Title
A numerical and observational investigation of short and long internal wave interactions

Author
Vanderhoff, Julie Crockett

Publication Date
2007

UNIVERSITY OF CALIFORNIA, SAN DIEGO

A numerical and observational investigation of short and long internal wave interactions

A thesis submitted in partial satisfaction of the
requirements for the degree Doctor of Philosophy
in
Engineering Sciences (Mechanical Engineering)

by

Julie Crockett Vanderhoff

Committee in charge:

Professor Keiko Nomura, Chair
Professor James Rottman, Co-chair
Professor Rob Pinkel
Professor Stefan Llewellyn Smith
Professor Kraig Winters

2007

The thesis of Julie Crockett Vanderhoff is approved, and it is acceptable in quality and form for publication on microfilm:

Co-chair

Chair

University of California, San Diego

2007

To Calvin,
for all your support,
and love.

Also to my family,
who have never doubted me.

TABLE OF CONTENTS

Signature Page . . . iii

Dedication . . . iv

Table of Contents . . . v

List of Figures . . . vii

Acknowledgements . . . xii

Vita . . . xiii

Abstract . . . xvi

I Introduction . . . 1
- A. Introduction . . . 1
- B. Literature Review . . . 4
  - 1. Wave-wave Interactions . . . 5
  - 2. Wave Interactions with Shears . . . 10
- C. Summary and Outstanding Issues . . . 19
- D. Research Objectives . . . 21
- E. Dissertation Outline . . . 22

II Dynamics of a Single Short - Long Wave Interaction . . . 25
- A. Idealized Problem Set-up . . . 25
  - 1. Initial conditions . . . 28
- B. Ray Theory . . . 29
  - 1. The ray equations . . . 29
  - 2. Caustics and Critical layers . . . 31
  - 3. Analytic ray solutions . . . 32
- C. Numerical ray solutions . . . 36
  - 1. Encounters of the first kind $c_{g0} \gg c$ . . . 36
  - 2. Encounters of the second kind $c_{g0} \approx c$ . . . 42
  - 3. Encounters of the third kind $c_{g0} \ll c$ . . . 42
- D. Numerical Simulations . . . 47
  - 1. Solving the Equations . . . 48
  - 2. Results . . . 49
- E. Discussion . . . 53

III Statistical Study of Wave-Wave Interactions 58
- A. Problem Parameters 58
- B. Ray and Adiabatic Invariance Theory 59
  - 1. Ray theory 59
  - 2. Adiabatic Invariance Theory 59
- C. Numerical ray solutions 62
  - 1. Wave sets 63
  - 2. Short wave horizontal wavenumber changes 76
  - 3. Propagation through many inertial waves 79
- D. Discussion 81

IV Observational Analysis 83
- A. Observational Setup 86
- B. Mathematics and Analysis 93
- C. Triple Product 101
  - 1. Triple Product in Numerical Simulations 103
  - 2. Triple Product in Ray Tracing 106
  - 3. Triple Product in Observations 109
- D. Wave Breaking 112
  - 1. Wave Breaking in Numerical Simulations 112
  - 2. Wave Breaking in Ray Tracing 117
  - 3. Wave Breaking in Observations 118
- E. Discussion 120

V Conclusions 122
- A. Summary 123
  - 1. Single Short and Long Wave Interaction 124
  - 2. Statistical Analysis 125
  - 3. Observational Analysis 127
- B. Future Work 128
  - 1. Three-dimensional Ray Tracing 129

Bibliography 131

LIST OF FIGURES

Figure II.1: Schematic of a short wave packet approaching an inertia-wave packet with basic parameters shown. 26

Figure II.2: Schematic of a short wave packet propagating through an inertia-wave packet. Dot-dashed line corresponds to the ray. Each short and long wave drawn is for a different snapshot in time. 35

Figure II.3: An encounter of the first kind: (a) the ray path, where the boundaries of the shaded, quasi-elliptical regions mark the locations where, at a given instant t, the strong-refraction condition $c_g = c$ can be satisfied (see text); (b) the wave-action density 37

Figure II.4: Comparison of the first-kind encounter (left column) with the approach to a critical layer (right column). The plots of $m^{-2}\partial m/\partial z$, m, $\hat{\omega}$, and A are for the first ray in the corresponding upper plot. For the first-kind encounter $m_{initial}/k = -3$. 41

Figure II.5: An encounter of the second kind. Plot details are as in Fig. II.3, but note the different scalings on the time axes, and that, despite appearances, the inertia wavenumber M and packet envelope scale L are the same; it is only the short-wave parameters . . . 43

Figure II.6: An encounter of the third kind. Plot details are as in Fig. II.3, but note the different scalings on the time axes, and that, despite appearances, the inertia wavenumber M and packet envelope scale L are the same; it is only the short-wave parameters 44

Figure II.7: A third-kind encounter followed by an upgraded first-kind encounter. All plots have the same horizontal axis, the time in inertial periods. Top: the ray path, which originates from $z = -4\lambda_i$ at $t = 0$, and the vertical profile of the inertial velocity u at $t = 0$. . 46

Figure II.8: An encounter of the first kind: (a) the perturbation density as a function of depth and time as computed by the spectral numerical method. Overlaid on the plot are ray paths computed as described in section II.B; (b) the time-averaged vertical 49

Figure II.9: Initial parameters as those in first-kind except with positive m_i and z_0. Plot details are as in Fig. II.8a. 51

Figure II.10: An encounter of the second kind. Plot details are as in Fig. II.8, but with straight line slope in (b) -1.7. 51

Figure II.11: An encounter of the third kind. Plot details are as in Fig. II.8, but with straight line slope in (b) -2.5. 52

Figure III.1: As in Figure 5 in Bruhwiler and Kaper [7]. Lines are from adiabatic invariance theory, and dots from the ray tracing. Scatter plots show the results of simulating 1000 test waves for $\mu_0 = 2.0$ and (a) $\epsilon = 0.2$, (b) $\epsilon = 0.1$, and (c) $\epsilon = 0.05$. 63

Figure III.2: Maximum (upper dashed line) and minimum (lower line) nondimensional vertical wavenumber values of the short wave for which strong refraction can occur at each μ_0 shown on the horizontal axis. Dot-dash line is located at the location $\mu_0 = 2$. 65
Figure III.3: Ray paths for 60 rays when (a) $\epsilon = 0.2$ and (b) $\epsilon = 0.05$. Boundaries of the shaded quasi-elliptical regions mark the locations where, at a given instant t, the strong-refraction condition $c_g = c$ can be satisfied (see text) 67
Figure III.4: Background velocity profiles for $\epsilon = 0.2$. Solid line is at $t/T_i = 3.75$, dashed line is at $t/T_i = 4$, and dotted line is at $t/T_i = 4.25$. Dot-dashed lines are minimum and maximum u_c values, 0.0049 and 0.0094 respectively. 69
Figure III.5: (a) A closer look of Fig. III.3a. (b) The corresponding background velocity values at $z = -97m$ (solid line) and $z = -86m$ (dashed line). The first two heavy dotted lines correspond to the first initial and final locations of strong refraction, the third is . . . 70
Figure III.6: Snapshot of background velocity U at different times throughout a short-long wave interaction. The vertical dot-dash lines outline the u_c values for which strong refraction will occur. For each snapshot we follow cartoon rays through their strong refractions . . 71
Figure III.7: Initial background velocity profiles (solid lines) for (a) $\epsilon = 0.2$ and (b) $\epsilon = 0.05$. Dot-dash line is envelope, dashed lines correspond to minimum and maximum u_c values for the range of initial rays used, and highlighted area is equal on both graphs. 73
Figure III.8: As in Fig. III.1. Scatter plots showing the results of simulating test waves for $\mu_0 = 2.0$ and (a) $\epsilon = 0.2$, (b) $\epsilon = 0.1$, and (c) $\epsilon = 0.05$, where an example set of waves is circled in each graph. . . 74
Figure III.9: As in Figure 8 in [7]. Frequency spectrum from a number of short waves, energy accounted for by number of waves in each frequency bin. $\epsilon = 0.1$, $\mu_0 = 2$, and $k = 2\pi/200$. Initial frequency spectrum (solid line), final spectrum calculated through 76
Figure III.10: Number of waves with initial (solid line) and final frequency spectrum calculated through ray tracing (dashed line), final frequency spectrum calculated through adiabatic invariance theory (dotted line), where $\epsilon = 0.1$, $\mu_0 = 0.3$, and $k = 2\pi/5000$. 77
Figure III.11: As in Fig. III.9 but for initial values of k having a -2 log slope, ranging from (a) $k = 2\pi/10000$ to $k = 2\pi/200$, and (b) $k = 2\pi/500$ to $2\pi/200$. $\epsilon = 0.1$, $u_0 = 4$cm/s, and $0.2 < \mu_0 < 2.0$. 30 bins are used to find the energy at each ω value. 78
Figure III.12: Initial and final short wave frequencies (values binned): (a) using adiabatic invariance theory, (b) using ray tracing. Note the difference in scales, as more waves were used in the theoretical case because of the fast calculation time. 80

Figure IV.1: Observational cruise paths from 2000 to 2002 along and around the Hawaiian Ridge. Figure provided by HOME researchers on chowder.ucsd.edu/home/index.html 84
Figure IV.2: Location of FLIP during August 2002 HOME Nearfield data collection. The blue circle represents the location of FLIP, the red circles are the locations of the moorings. The solid lines denote cross-ridge and along-ridge directions. 86
Figure IV.3: View of Kaena Ridge from the east looking west. 87
Figure IV.4: View of Kaena Ridge from east-south-east looking west-north-west. 88
Figure IV.5: View of Kaena Ridge from south-south-west looking north-north-east. 88
Figure IV.6: Average current over time. (a) Average zonal velocity (where positive is eastward) over depth for year days 258 to 291. (b) Average meridional velocity (where positive is northward) over depth for year days 258 to 291. (c) Average zonal velocity over depth . . . 90
Figure IV.7: Average buoyancy frequency over 32 days, fit with a cubic spline. 91
Figure IV.8: Observations from sonar data over Kaena Ridge for one week (year day 260 to year day 267) over all depths (100 meters to 800 meters). Inertial, diurnal, and semidiurnal frequencies are labelled. Line with slope of -2 superimposed on both the frequency 92
Figure IV.9: (a) Cross-ridge shear normalized by buoyancy frequency (dimensionless) calculated from the sonar data. (b) Strain rate squared [1/days^2] calculated from the sonar data. 96
Figure IV.10: Observations over Kaena Ridge. Line at location of near-inertial frequency of 0.9 cycles per day. Data over the one week of interest, year day 260 to 267, and the depths of interest, 425 to 475 meters. This is a 52 degree of freedom estimate. 98
Figure IV.11: (a) Cross-ridge shear normalized by buoyancy frequency calculated from the CTD profiles, filtered to only include low frequencies. (b) Strain rate squared calculated from the CTD profiles, smoothed with a 30 meter, 6 hour 99
Figure IV.12: Numerical simulation results. (a) The shear from the near-inertial wave, the colorbar units are [1/days]. (b) The squared strain rate of the short wave as defined in the text, colorbar units are [1/days^2], and include only high frequency waves. 99
Figure IV.13: Coherence and phases between the near-inertial cross-ridge shear and the high frequency squared strain rate in the area of modulation. This is a 52 degree of freedom estimate. (a) Coherence in observations, (where the squared strain rate is smoothed 100

Figure IV.14: Numerical simulations of a third-kind encounter, $m/k = -35$ initially. (a) Triple product averaged over time [m^2/day^3], $\overline{uwU_z}$. (b) Triple product [m^2/day^3]. (c) Background shear [1/day]. 103
Figure IV.15: Numerical simulations of a third-kind encounter. Average Reynolds stress (×10) [m^2/day^2], $\overline{uw}$, (blue), average triple product (×500)[m^2/day^3], $\overline{uwU_z}$, (green), and rms shear [1/day], $\sqrt{U_z^2}$, (red). 104
Figure IV.16: Numerical simulations of a third-kind encounter. Average positive shear over time and average negative shear over time (red positive, blue negative), average triple product at positive shear locations (light blue), average triple product at 105
Figure IV.17: Ray tracing calculations of a set of 1500 waves with different initial depths and frequencies ranging from $2f$ to $0.99N$. Average shear (×10^5) over time (red positive, blue negative), average triple product (×10^7) at positive shear locations 107
Figure IV.18: Observational analysis of flow over Kaena Ridge for two days over 200 meters. (a) Triple product averaged over time [m^2/day^2], $\overline{uwU_z}/N(z)$. (b) Triple product [m^2/day^2]. (c) Background shear [1/day]. 109
Figure IV.19: Observational analysis over Kaena Ridge, averaged from year day 262 to 264. Shear is divided by the buoyancy frequency as it is variable over the ocean depth. Average Reynolds stress, $\overline{uw}$, (blue), average triple product (×500) 110
Figure IV.20: Observational analysis over Kaena Ridge, averaged from year day 262 to 264. Shear is divided by the buoyancy frequency as it is variable over the ocean depth. Average shear (×10^5) over time (red positive, blue negative), average triple product 111
Figure IV.21: Numerical simulation of a third-kind encounter, where initially $m/k = -35$, and $\zeta_z = 0.1$. (a) Background shear [1/days]. (b) Possible breaking map for numerical simulation of a third kind encounter. The colorbar represents ζ_z 113
Figure IV.22: Numerical simulation of a first-kind encounter, where initially $m/k = -3$, and $\zeta_z = 0.6$. (a) Background shear [1/days]. (b) Possible breaking map for numerical simulation of a first-kind encounter. The colorbar represents ζ_z 114
Figure IV.23: Breaking map for numerical simulation of a third kind encounter with an initial wave steepness of $\zeta_z = 0.9$ and $m/k = -35$. The colorbar represents ζ_z 115
Figure IV.24: Breaking map for numerical simulation of a third kind encounter with an initial wave steepness of $\zeta_z = 1.5$ and $m/k = -35$. The colorbar represents ζ_z 115

Figure IV.25: Ray paths for different rays within the ray tracing simulation where the filled in ellipses are outlined by locations of strong refraction and corresponding ζ_z values along the ray. (a) First-kind encounter, $m/k = -3$. Notice the locations of positive and 116

Figure IV.26: Observational analysis over Kaena Ridge for two days over 200 meters depth. (a) Inertial shear divided by buoyancy frequency. (b) Wave breaking map calculated from CTD data. The colorbar represents ζ_z. 118

ACKNOWLEDGEMENTS

I am very grateful to my advisors, Professor James Rottman and Professor Keiko Nomura, who have provided me with academic and financial support while helping me pursue my research interests. I am also indebted to Professor Rob Pinkel for the opportunities he provided me to spend time in the field learning.

I am deeply grateful to the other members of my committee, Professor Stefan Llewellyn Smith and Professor Kraig Winters for their helpful comments and discussions.

I would like to further thank Professor Rob Pinkel's group for their support - Loyd Green, Mike Goldin, Jon Pompa, Tyler, Tony, Mi, and Oliver Sun. Also all those other researchers on the cruises.

Thank you to the department support staff for their administrative and technical support.

VITA

Ph.D., Engineering Science (Mechanical Engineering)
University of California, San Diego (2007)

M.S., Engineering Science (Mechanical Engineering)
University of California, San Diego (2004)

B.S., Mechanical Engineering
University of Denver (2002)

TEACHING EXPERIENCE

Teaching Assistant, University of California, San Diego
Dept of Mechanical and Aerospace Engineering (2004-present)

Served as T.A. for upper-division undergraduate courses: Thermodynamics (2 quarters), Fluid Mechanics, I (5 quarters), Fluid Mechanics, II (4 quarters) Received excellent student student evaluations each quarter. Improved student understanding of coursework by preparing and presenting discussion sections, holding office hours, answering emails and preparing and presenting review sessions. Served as head TA for 250 student class with 4 TA's and 5 graders, organizing TA and grader workload. Prepare homework solution sets.

Teaching Consultant: Individual Adjunct Professors
(see references, Dr. Rohr) (2005-present)

Review professor lectures for accurate content and appropriate length.
Create homework assignments and solutions.
Create quizzes, tests, and solutions testing students' knowledge over homework and lecture material.

TEACHING INTERESTS

Fluid Mechanics, Heat Transfer, Thermodynamics, Environmental Engineering, Numerical Methods, Computational Fluid Dynamics

RESEARCH EXPERIENCE

Graduate Research, Dept of Mechanical and Aerospace Engineering, UCSD (2002-present)
Advisor: Professor James W. Rottman.

Oceanic and atmospheric internal wave propagation through time independent and time dependent shears leading to changes in internal wave energy distribution and possible energy dissipation.

Accomplishments: In depth analysis of dynamics at location of wave interactions, including amplitude, frequency, and energy changes; statistical analysis of many realistic wave-wave interactions; three-dimensional ray tracing of wave-wave interactions

Selected computational skills: ray tracing using ray theory, computational fluid dynamics through numerical modeling with spectral and finite differencing codes.

Research Intern, SPAWAR (summer 2005 and 2006)
Principal Investigator: Dr. James Rohr.

Modeling and analysis of bioluminescent organisms flashing in pipe flow using Matlab.

Selected computational skills: microfluidics flow in a pipe.

Graduate Fieldwork, Scripps Institute of Oceanography (2002, 2006)
Advisor: Professor Rob Pinkel.

Two trips to Pacific Ocean (total of 7 weeks) to collect data on internal wave propagation. A part of the Hawaiian Ocean Mixing Experiment.

Selected technical skills: housing and deployment systems for current-temperature-density probes.

Undergraduate Research, University of Denver (2001-2002)
Advisor: Professor Corinne Lengsfeld.

Importance of electric potential gradient and charge density in droplet breakdown.

Selected technical skills: atomization spray techniques.

UNIVERSITY SERVICE AND OUTREACH

Present engineering projects to local middle and high schools, recently Gompers Middle School (a UCSD partnership charter school) Community Outreach Science Night (2007)

Graduate Student Panelist for prospective graduate students (2004)

Featured on UCSD Jacobs School of Engineering website discussing research to entice prospective graduate students (2002)

AWARDS AND FELLOWSHIPS

2006-2007 Outstanding Teaching Assistant, Dept of Mechanical and Aerospace Engineering, UCSD

2005, 2006 Travel Award, Dept of Mechanical and Aerospace Engineering, UCSD

2002-2003 Freshman Fellowship, Dept of Mechanical and Aerospace Engineering, UCSD

PUBLICATIONS, CONFERENCE AND SCHOLARLY PRESENTATIONS

Vanderhoff, J., Rottman, J., Nomura, K., and Macaskill, C. Doppler spreading of internal gravity waves by an inertia-wave packet. Accepted to Journal of Geophysical Research - Oceans, August, 2007.

Vanderhoff, J., Rottman, J., Nomura, K., and Broutman, D. Statistical analysis of short wave packets interacting with near inertial waves. To be submitted to Journal of Geophysical Research - Oceans, November, 2007.

Vanderhoff, J., Rottman, J., Nomura, K. Scattering of small-scale internal waves by near-inertial wavepackets in the ocean. American Physical Society Division of Fluid Dynamics Annual Meeting, November, 2006. Conference talk.

Vanderhoff, J., Rottman, J., Nomura, K. Evolution of a small-scale internal wave-packet through a time varying shear. UCSD Research Expo, February, 2006. Poster Session.

Vanderhoff, J., Rottman, J., Nomura, K. Doppler spreading of internal gravity waves in the ocean. American Physical Society Division of Fluid Dynamics Annual Meeting, November, 2005. Conference talk.

Vanderhoff, J., Rottman, J., Nomura, K. Doppler spreading of internal gravity waves by an inertia-wave packet. UCSD Research Expo, February, 2005. Poster Session.

ABSTRACT OF THE DISSERTATION

A numerical and observational investigation of short and long internal wave interactions

by

Julie Crockett Vanderhoff
Doctor of Philosophy in Engineering Sciences (Mechanical Engineering)
University of California, San Diego, 2007
Professor Keiko Nomura, Chair
Professor James Rottman, Co-chair

The breaking of oceanic internal waves is an essential part of the deep-ocean mixing processes that contribute to the general circulation of the ocean, the exchange of heat and gases with the atmosphere, the distribution of nutrients and the dispersal of pollutants. It is essential to improve our understanding of how these waves evolve toward dissipation. In this thesis ray theory, numerical simulations, and observations are used to examine the refraction of short internal-wave packets by time-dependent background shear profiles to test the validity and explore the limitations of currently used models of short internal waves propagating through steady shear in the deep ocean. Types of possible interactions due to initial short wave parameters are categorized. An analysis of observational ocean data supports the simulation results which show a change in the propagation of short internal waves and their properties when time-dependence in the background shear profile is taken into account. Through ray theory and simulations, a net exchange of energy to the background wave is found, which is consistent with ocean data. It is found through ray theory that the highest frequency short waves are the most likely to break, and these calculated locations are also consistent with ocean observations. The results of our simulations and analysis are enough to show that the ignored physical effect of the time-dependence in the long-wave shear can make a significant difference to short-wave behavior and should be taken into account in the models.

I

Introduction

I.A Introduction

In any stratified fluid medium, if there is a disturbance to the fluid and particles are displaced from their equilibrium, internal waves will result. For example in the ocean, internal waves may be created by wind forcing at the surface, by tidal flow over topography, or by small mixing processes. There are billions of internal waves present in both the ocean and atmosphere, which are both stably stratified. These internal waves in the ocean may have horizontal length scales on the order of kilometers, or centimeters, and vertical length scales equal to that of the ocean depth, or equal to that of a snail. Their frequencies range from as slow as 1 cycle per day to as fast as 100 cycles per day, corresponding to the range between the buoyancy and inertial frequency. Some of these internal waves are capable of carrying energy across oceans. Other internal waves may break and dissipate their energy within the ocean interior. Because of their ability to carry and dissipate energy, what happens to internal waves as they propagate through the ocean interior is very important. Waves may be affected by other internal waves, by themselves, by time-dependent shears in the ocean, or by time-independent shears in the ocean. The results of these interactions are exchanges of energy between different wavenumbers and frequencies, as well as wave breaking resulting in energy dissipation.

Some of the prevailing long waves in the ocean are downward propagating waves of inertial frequency created by wind blowing over the ocean surface. These waves are generally large-scale because of the scale of the energy input from the strong winds. Many other waves in the ocean will inevitably propagate through these large-scale inertial waves. Therefore a better understanding of what is occurring when internal waves created within the ocean interior interact with these inertial waves is necessary. Because of the long lengthscale of the inertial waves they can be thought of as a time-dependent shear profile. In the past many studies were done in which short waves interacted with time-independent shears, but observations have shown that the presence of steady shear is much less common than unsteady shear in the ocean. Thus there is an interest in short-wave interactions with unsteady shears.

First we need to understand the basic dynamics of an interaction between a small-scale, high-frequency wave and a large-scale, low-frequency wave. This interaction may be thought of as Doppler spreading of short waves by longer waves, where Doppler shifting is a shift in the short-wave frequency due to its refraction by the long wave. We are also interested in a statistical study of a number of these interactions occurring, as this is a more realistic setup with so many short waves propagating through the ocean. The more we understand the interactions occurring in the ocean, the closer we are to finding how and where energy is dissipating within the ocean.

Munk and Wunsch [40] used TOPEX/Poseidon (T/P) satellite altimeter data and tidal models to conclude that 2 terawatts (TW) of energy are necessary to maintain the large-scale thermohaline circulation of the ocean through deep ocean mixing. 1 TW of energy comes from the wind driving the surface of the ocean. Wunsch [67] found surface kinetic energy estimates that support this. It seems that the other half of the energy would be provided by the tides. Egbert and Ray [13] used T/P satellite altimeter data of tidal elevations in the sea surface to estimate that 1 TW of tidal energy is dissipated in the deep oceans. So the question is where the tides will be most effective at mixing the ocean.

Initially it was thought that the principal sink of barotropic tidal energy would be in the shallow seas because of the bottom friction there. But evidence of diapycnal mixing affecting the deep ocean suggests barotropic tidal dissipation due to flow over bottom topography may also be important. St.Laurent and Garrett [51] used internal wave theory of tidal flow over topography and concluded less than 30% of energy flux created is at smaller spatial scales and subject to local dissipation, providing irreversible transport of momentum across isopycnal surfaces. The larger scale waves propagate away from topography into the open ocean to interact with background ocean shears. This was also seen in an observational study over the Hawaiian Ridge where Rudnick et al. [48] directly measured turbulent energy dissipation rates with a collection of profiling and towed instruments. Diapycnal diffusivity was estimated from the dissipation. They found the isolated ridges were important sinks for surface-tide energy and were sites of elevated mixing. However, this local tidal conversion at ridges which is an important source of energy for mixing, could not account for the global eddy diffusivity of $10^{-4}\text{m}^2/\text{s}^{-1}$. Using five different sets of T/P data Egbert and Ray [13] found that dissipation is clearly enhanced over ridges and island chains oriented perpendicular to tidal flows, including the Hawaiian ridge. Recently a field study experiment in which I participated, the Hawaiian Ocean Mixing Experiment (HOME), tested this theory of strong mixing over the Hawaiian ridge. They found 15 gigawatts (GW) of tidal energy being dissipated there, which matches well with the data of Egbert and Ray [13] who calculated dissipation energies of about 20 GW. Llewellyn Smith and Young [35] used linear wave theory to find 90 GW of energy may be put into internal gravity waves purely by flow over weak topography throughout the world oceans.

If these internal gravity waves evolve to small enough scales they may break and cause mixing. The propagation and dissipation, mainly due to breaking, of internal waves is an integral part of momentum transfer and mixing in the oceans and atmosphere. Müller and Liu [39] tested, both theoretically and numerically in a two-dimensional finite-depth ocean, the scattering of tidal flow over topography and found different topographical shapes would matter, with the most jagged and convex portions of the topography being the most prone to scattering of internal waves in wavenumber space, generally to higher modenumbers. The turbulence produced by wave-breaking of small-scale, high modenumber waves may have a large effect on the diapycnal mixing in the oceans [53]. There are many wave-wave interactions which may be responsible for transferring energy of internal waves to to such small scales. These processes include, but are not limited to, steady shear interactions (critical layer), time-dependent shear interactions (caustic), self-acceleration, elastic scattering, and parametric subharmonic instability (PSI). Through some these mechanisms it is possible for waves to reach high enough frequencies and small enough scales to break and dissipate their energy. Which of these mechanisms are most dominant in the ocean is not yet fully understood though, and must be addressed. It is a question of high importance as global circulation models and coastal models are on the edge of resolving small enough scales to include near-inertial shear effects. Calculating more accurately the energy transfer between waves and mixing will improve models of the earth and atmosphere which will in return provide better estimates of climate.

I.B Literature Review

This section is a review of the main papers relating to the subject of internal wave interactions.

There is a question of dominance of mechanisms transferring energy to smaller scales in the ocean and atmosphere. This is important because once the waves reach these smaller scales they are able to break and dissipate, mixing the ocean interior and affecting organisms, pollutants, and the general global circulation of the wind and seas. These mechanisms include parametric subharmonic instability (PSI), induced diffusion (including both critical layers and refraction at caustics), and elastic scattering. Each of these mechanisms is argued to be the dominant mixing mechanism in the oceans and atmosphere, but each has strengths and weaknesses.

I.B.1 Wave-wave Interactions

The three basic mechanisms classified for the transfer of energy between internal waves are elastic scattering, parametric subharmonic instability (PSI), and induced diffusion. Elastic scattering is the vertical backscattering of a downward propagating, high-frequency wave by a low-frequency near-inertial wave. PSI is the breakdown of one wave into two waves of half the original frequency. For example an M_2 wave, created by the semidiurnal lunar internal tide (such that the resulting M_2 frequency is approximately 2 cycles/day), into two waves of 1 cycle/day, which can only occur when that frequency is less than the inertial frequency at the specific latitude. Induced diffusion efficiently transfers energy from high-frequency high-wavenumber waves to other higher frequency waves through interactions between short waves and steady or unsteady shear. In the past, studies of these types of interactions have been most successful in describing the high-frequency wave spectrum in the ocean.

Other mechanisms are also at work in the ocean, including self-acceleration, which is the advection of short waves by their self induced mean flow. Sutherland [57] found self-acceleration to be the dominant mechanism transferring energy to the shorter length scales during the initial evolution of non-hydrostatic (high-frequency) large amplitude internal waves. The simulations run by Sutherland [57] use a wide range of wave packet widths, shapes, and amplitudes. Self-acceleration has not been given much attention partially because it does not occur in laboratory experiments because the waves are confined laterally by the tank side-walls so a mean horizontal flow cannot develop. It is also not a dominant factor in plane waves because the wave-induced mean flow is vertically uniform. But, through self-acceleration, wave packets with sufficiently large amplitude, and thus a large self-induced mean flow acceleration, can evolve to become convectively unstable, as Grimshaw [24], Dunkerton [11], Fritts [15], and Sutherland [56] found.

Elastic Scattering

During elastic scattering the energy of the high frequency short waves involved is mainly being transferred back and forth, acting to keep the high frequency vertical wavenumber spectrum in the ocean in equilibrium, but not acting as a mechanism actually taking energy from the lower frequency waves. This mechanism therefore generally does not lead to short-wave breaking.

Parametric Subharmonic Instability

PSI can only occur when $M_2/2$ is greater than the inertial frequency, or Equatorward of 28.9°. There has been a revival in the study of PSI as an effective transfer mechanism since observations by Polzin, Toole, Ledwell, and Schmitt [46] have shown energy at the $M_2/2$ frequency. Then numerical simulations were done by Hibiya, Nagasawa, and Niwa [30] as well as MacKinnon and Winters [36] where M_2 waves with coherent phases resulted in energy transfer time scales of days, which would result in dissipation of the short-waves in deep water. But Olbers and Pomphrey [43] found that when these waves have random phases the result is energy transfer time scales of hundreds of days. This is possibly because the theoretical calculations of Olbers and Pomphrey [43] were based on an assumption that the waves in question are in a statistical steady state with randomly distributed phase and direction, which may not be appropriate near internal-tide generation sites.

MacKinnon and Winters [38] did simulations of M_2 waves propagating poleward, equatorward, and at the critical latitude. The simulations assume a 'hyper-difusivity', which cuts off any wave with a vertical wavelength smaller than 150 meters, as it is assumed such a wave will break and dissipate. Those waves which are not cut off are absorbed at the 'thermocline' (top layer of the simulation, sponge layer). The simulations poleward of the critical latitude resulted in all the energy being absorbed at the top layer: there was no energy dissipation throughout the simulation. This is an idealized situation, as there must be other mechanisms working in the ocean because there is dissipation in the oceans poleward of the critical latitude. MacKinnon and Winters mention these are the waves which propagate further into the ocean and dissipate elsewhere. They find at the critical latitude, after the simulation has reached a steady state, it shows energy dissipating in the first 1 km as the waves propagate upwards. Then there is a linear decrease up to about 3 km. This simulation displays the energy dissipating on a time scale of 2 days. This coincides with the time scale of energy dissipation calculated using the formula given by Staquet and Sommeria [53], L/U, where L is the vertical wavelength and U is the rms horizontal velocity of the waves. If the time scale put forth by Olbers and Pomphrey [43] were used, the waves would travel out of the simulation domain before transferring energy to the small scales. The idealized simulation, with no shear and no smaller scale waves, shows 80% of the energy input being dissipated in the location of the critical latitude. Equatorward of the critical latitude MacKinnon and Winters still find energy dissipation due to PSI, but less than at the critical latitude. Here PSI transfers 40% of the initial wave's energy to dissipation.

The latitude dependence of dissipation found from PSI follows the same ideas as those found in Gregg, Sanford, and Winkel [22]: the mixing decreases with decreasing latitude. They find when the same energy is input in the small-scale internal waves at all latitudes, the lower latitudes result in less dissipation. This may have to do with weaker background shears at lower latitudes. Results of MacKinnon and Winters [36] imply an order-one dependence on latitude for the percentage of generated energy lost in producing local mixing hotspots near tidal conversion sites (St. Laurent and Nash [52] suggest on average 30% lost near hotspots). So PSI dissipation rates range from 0% to 80% over a latitude range up to 28.9°.

In the ocean, Nagasawa et al. [42] tested their earlier numerical experiments, which showed that the energy cascade across the internal wave spectrum down to small dissipation scales was under strong control by PSI. They used 106 expendable current profilers in the North Pacific, including near the Aleutian Ridge (53° N, 165° W), the Hawaiian Ridge (22.8° N, 167.6° W), and the Izu-Ogasawara Ridge (30° N, 144° E). The main conclusion was that at mid-latitudes (Equatorward of the critical latitude 28.9°) there is significant enhancement of the 25 m vertical shear over known locations of generation of semidiurnal internal tides, such as the ridges above. At high latitudes this enhancement was not found. They found high vertical wave number, near-inertial shear, as created by PSI, plays a key role in controlling turbulent mixing processes.

A comparison is then made by Nagasawa et al. [42] between the internal wave power spectrum measured and that of Garrett and Munk [19]. It is found that at the lower latitudes (and lower depths) there is an increase in the ratio of Froude numbers where $Fr^2_{measured}/Fr^2_{GM}$ is $4-6$, whereas at the higher latitudes it is $1-3$. Even at the Izu-Ogasawara Ridge (30° N) it was seen that north of the location of the ridge there was no significant increase in the above mentioned ratio, yet south of the ridge there was. This relationship is consistent with PSI, which cannot occur Poleward of 28.9°.

Gregg [21] gave an empirical formula for the turbulent dissipation rate, which Nagasawa et al. [42] used, but for a vertical shear with a vertical scale of 25 m vertical shear (instead of 10 m). This dissipation rate is then used to estimate the diapycnal diffusivity following Osborn [44]. Over the ridges below the critical latitude of PSI the inferred diapycnal diffusivity reaches $2 \times 10^{-4}\mathrm{m}^2/\mathrm{s}$. This is the order of magnitude required to satisfy the large-scale advective-diffusive balance of the meridional overturning circulation. It is better than previous microstructure measurements carried out in the ocean interior where the diapycnal diffusivity was estimated to be $10^{-5}\mathrm{m}^2/\mathrm{s}$.

Hibiya, Nagasawa, and Niwa [30] used vertically two-dimensional numerical simulations to test how energy supplied by M_2 internal tides cascades through the local internal wave spectrum down to dissipative scales. They looked specifically the Aleutian Ridge (at 49° N) and the Hawaiian Ridge (at 28° N) because both generate large-amplitude M_2 internal tides. Two-dimensional Navier-Stokes equations under the Boussinesq approximation were integrated with a finite-difference scheme by applying centered differences and a leapfrog scheme. They input an instantaneous perturbation in the form of an energy spike at the lowest vertical wave number and the M_2 tidal frequency. They find that for the Hawaiian Ridge, because the high vertical wave number, near-inertial current shear is intensified, high horizontal wave number internal waves are efficiently Doppler shifted so that the vertical wave number rapidly increases and enhanced turbulent dissipation takes place. The elevated spectral density in the high vertical wave number, near-inertial frequency band, which plays the key role in cascading energy to dissipation scales, is thought to be caused by parametric subharmonic instability, PSI. In the Aleutian Ridge set up this is not seen, as the M_2 tidal frequency is 1.2 times the inertial frequency and therefore free from PSI.

Luc Rainville [47] found observations of energy fluxes from FLIP indicate a PSI-like mechanism occurring, but with a much shorter interaction timescale than was originally thought possible for PSI. In both the near field and far field, the energy flux in the diurnal band varies according to the presence or absence of strong semidiurnal internal tides, and exhibits a more complex vertical structure (higher modes) than the semidiurnal internal wave field. Because of the slow propagation speed of the high modes and the synchronism mentioned, he interprets most of the signal of the diurnal band to be at frequency $M_2/2$, and a product of nonlinear interactions of the M_2 internal tide. This process might be PSI. Yet the short time scale in the near field points towards a local and probably non-resonant mechanism. The energy transfrerred to a new frequency propagates away from the interaction region and is not available to transfer back to the original waves.

Furuichi, Hibiya, and Niwa [17] calculate bispectra in numerical simulations of tidal energy transfer to show another type of triad interaction existing between the lowest vertical wavenumber M_2 internal tide and two nearly identical internal waves with horizontal wavelengths of $0.5 - 20$ km and periods less than four hours. Because the frequency and wavenumber of the M_2 internal tide are both lowest among the triad members it suggests this resonant interaction is induced diffusion. But the amount of energy drained this way is an order of magnitude lower than by

PSI.

MacKinnon and Winters [37] did an idealized numerical study of northward propagating M_2 waves which showed a dramatic loss of energy to small-scale subharmonic instabilities near 28.9°. After spinup, PSI acts as an effective filter of northward tidal energy flux. Between 27.5° and 29.5° the steady-state northward tidal energy flux drops from 1.6kW/m to 0.6kW/m. The instability growth is limited at other latitudes in two main ways. First, the vertical group velocity of small-scale subharmonic motions increases with distance Equatorward of the critical latitude (as the subharmonic is increasingly super-inertial) leading to energy traveling hundreds of meters vertically on a ten-day time scale. Energy flux divergences drain subharmonic energy as it is generated, preventing the exponential buildup possible at the critical latitude. Second, at lower latitudes there are additional terms in the energy equation stemming from vertical velocity, displacements, and buoyancy anomalies of the subharmonic waves which act to reduce the overall growth of the subharmonic. Watanabe and Hibiya [62] also found that PSI increases energy at the near-inertial frequency, which results in an increase in diapycnal diffusivity, but only between 25° and 30°. Thus within this latitude band PSI may enhance the occurrence of interactions of short waves with unsteady shear.

I.B.2 Wave Interactions with Shears

Short waves interacting with shear profiles can also contribute to short-wave breaking and the dissipation of energy in the ocean and atmosphere. The interaction between steady shear and unsteady shear is dynamically different, and will be covered in more detail later.

Steady Shear

One of the most widely studied mechanisms for the transfer of internal wave energy to breaking scales is the critical layer. Critical layers are of interest because of the array of situations they present, the interaction of shear and buoyancy forces, fluid instability and stratified turbulence. Internal waves approach critical levels as they propagate through larger-scale currents in the ocean and winds in the atmosphere. A critical layer interaction occurs when internal waves encounter a background shear and reach a state where the shifted frequency of the short wave vanishes, generally resulting in absorption of the short wave into the mean flow at the critical level. Depending on its initial amplitude, the short wave as it approaches a critical layer may be almost completely absorbed by the mean flow, as the linear theory of Booker and Bretherton [2] found for small amplitude waves, may be partially reflected, as Winters and D'Asaro [65] found in numerical simulations, or may break if it initially has sufficiently large amplitude.

Using theory and some supplemental experiments, Hazel [26] included the effects of viscosity and heat conduction on a critical layer interaction. Hazel started with the basic two-dimensional, steady, linear, Boussinesq equations of motion, and then includes the viscosity and the coefficient of head conductivity. Viscosity and heat conduction are more important than non-linear effects, and including them results in a sixth order differential equation for the problem, which is not singular at the critical level, but has non-negligible viscous solutions near the critical level. The problem was solved assuming not only an input wave, but also a reflected and transmitted wave, as well as two more viscous solutions both above and below the critical layer, found using asymptotic analysis. Then the amplitudes were found using the matching solution and its first five derivatives.

Hazel's results agree with Booker and Bretherton [2]: the amplitude of the wave transmitted through the critical level is severely attenuated, and when rescaled to fit Hazel's problem the same attenuating factor was found. The reflected wave is non-existent when the most realistic initial conditions are used. The Reynolds stress decreases approximately linearly through a region just below the critical level (when the wave is traveling upward), until it has the constant small value it had above the level. This decrease in stress below the critical level shows that the momentum transfer to the mean flow takes place in this region. In short, Hazel finds the same factor of amplitude attenuation when accounting for viscosity and heat conduction as has been previously found for inviscid, adiabatic critical layer interactions.

Thorpe [60] found viscosity plays an important role, though, when short wave amplitudes are large enough to expect breaking. He studied critical layers in an accelerating shear flow field using experiments and numerical solutions of a model describing the weakly nonlinear development of the short waves. In the experiments the floor has a sinusoidal corrugation, as opposed to the earlier triangular obstacles used, and the internal waves that develop have a well defined wavelength and are more amenable to theoretical description. The shear flow was created by sharply tilting the tube through a small angle. Thickening dye lines show where the slope was greatest. These strong slopes correspond to surfaces which are inclined at increasingly shallower angles to the horizontal and are the most likely sites of gravitational overturn. Overturning occurred almost immediately above the troughs of the corrugated floor, while the opposite occurred above the crests, resulting in a Kelvin-Helmholtz looking profile. Yet there was no breaking, which Thorpe concluded was because of the viscous damping, since in the corresponding numerical simulations, where the effects of viscosity and diffusion were neglected, instabilities at the critical level were seen.

The refraction of short internal waves by longer inertial scale waves is also the main process modelled by Henyey and Pomphrey [27], Flatté, Henyey, and Wright [14], and Henyey, Wright, and Flatté [28] (hereafter HP, FHW, and HWF respectively),and Sun and Kunze [54, 55] in the ocean and in the atmosphere (Hines [32]). The refraction models of HP, HWF and FHW assumed critical layer interactions occur. Some major assumptions have been made in these models. The first is that ray theory is applicable, or in other words the background waves or shear have longer length and time scales than the shorter waves, and the background is not affected by the short waves. This is not a bad assumption considering the large difference in scales in the ocean between short waves and long near-inertial shears. But time-dependence of the background wave was never introduced, the background was always a steady shear, which is not characteristic of the unsteady shears found throughout the ocean interior. So the assumption that these time-dependent shears may be modelled as steady shears is in question. Another drawback was that the dissipation was calculated assuming the short waves broke when they reached a certain vertical wavelength, 5 meters. This may be a good assumption if the interaction is definitely with a critical level, but if the waves are in an unsteady shear they may refract to small wavelengths but stay intact. Finally, Henyey and Pomphrey did not take into account the amplitudes of the short waves, which may not lead to a correct estimate of wave-breaking. Fritts [15] found that if the amplitude of the short waves approaching a critical layer were small enough, no instability would occur at all. Henyey and Pomphrey have also been able to match recent observations of the latitude dependence of mixing in the ocean by Gregg, Sanford, and Winkel [22] and Garrett [18]. But this may be purely because the dissipation model of Henyey and Pomphrey depends on the energy in the Garrett-Munk spectrum, which decreases at the lower latitudes, as does dissipation.

Gregg, Sanford, and Winkel [22] compared ocean data with the theory of HWF [28] and found that the calculated dissipation rate very closely matches the ocean field data. Although time-dependence of the background shear and amplitude are not included in these calculations, it seems the model works well. The latitude dependence of the model arises because the rate at which the evolving waves are Doppler shifted depends on the ratio between their vertical and horizontal length scales, which depends on their dominant frequency, which is slightly greater than the Coriolis frequency, f and thus varies with latitude.

Winters and D'Asaro [64] performed high-resolution, two-dimensional numerical simulations of an internal wave packet approaching a critical level. They were able to compute accurately and carefully diagnose the internal wave propagation and breakdown processes. They found that shear instabilities, and not convective overturning, were the primary mechanism for breakdown, although the density field contained statically unstable regions for several buoyancy periods prior to breakdown.

Later, Winters and Riley [66] found that the instability mechanism is fundamentally three-dimensional in nature and exhibits both shear and convective dynamics. They solved the ray equations using a Runge-Kutta scheme. Then they also solve the sixth-order stability equation. The setup has strong shear regions coincide with stable stratification while weak shear regions coincide with unstable stratification.

The strong shear inhibits any streamwise convective instabilities, but spanwise convective instabilities exist when three dimensions are considered. These can grow and it is concluded that instability behavior is expected to be fundamentally three-dimensional when both shear and convective effects are important. The two-dimensional shear-driven instability studied by Winters and D'Asaro [64] occurred suddenly after many buoyancy periods during which unstable stratification existed. During this time the wave continued to shrink in scale and intensify its shear. The vertical scale at which instability did occur may have been smaller than if the wave were modelled in three dimensions. Thus it is possible that the energy partition and mixing efficiency of wave-breaking events will be biased by the two-dimensionality constraint.

Winters and D'Asaro [65] extended the three-dimensional work by studying the prediction of linear stability theory (that instability should develop through convective rolls oriented spanwise to the ambient shear) and quantifying the distribution of energy between various components of the flow field (incident and reflected waves, mean flow, mixing, and dissipation). It is known that the vertical wavenumber of the test wave increases dramatically through interaction with the ambient shear, and Winters and D'Asaro also expected that wave instability will produce turbulent flow at even smaller scales.

The critical layer is studied through a numerical simulation of an initial value problem using both large and small amplitude wave packets. Winters and D'Asaro used large-eddy simulations with damping. The early propagation, critical layer interaction, and subsequent trapping of wave energy near the critical level is two-dimensional. But three-dimensionality develops by transverse convective instability of the two-dimensional wave. The initially two-dimensional flow eventually collapses into quasi-horizontal vertical structures. It is found that one third of the initial energy reflects, the same amount joins the mean flow acceleration, and the last third cascades to small scales and is dissipated. Although this specific budget depends on the wave amplitude, it is clear that when both convection and shear are important three-dimensional dynamics may be important.

Unsteady Shear

Realistic environments have more complicated effects, such as time-dependent and three-dimensional shear. When the background shear is time-dependent, instead of short waves being absorbed, reflected, or breaking at a critical layer, the short waves are strongly refracted to different vertical wavenumbers, thus changing their group and phase speeds. Strong refraction occurs when the group speed of an internal wave is equal to the phase speed of the longer inertial wave. These locations of strong refraction are called caustics and the interaction may be represented by short waves propagating through longer waves in the ocean. Time-dependence of the background flow is important because it removes the constraint that the absolute frequency must be constant along the ray. In a steady horizontal shear flow this constraint forces the frequency to return to the same value whenever the background horizontal velocity is zero, preventing permanent changes which can occur when the background shear is time dependent. The time-dependence also eliminates the occurrence of critical layers, which would otherwise be important for short-wave dynamics.

Broutman [3] was motivated to study interactions of short waves with time-dependent shears by a collection of observations and calculations including: observations by Pinkel 1983 and comments from T. B. Sanford indicating the presence of many groups of downward-propagating inertial waves in the upper ocean; and understanding how critical layers are modified when the background flow is time varying. Hence Broutman [3] used ray tracing theory to investigate the interaction between a single short wave packet and an inertial wave, making many of the same assumptions as Henyey and Pomphrey, except using a time dependent inertia wave with arbitrary amplitude. Broutman found that when a more realistic background wave velocity (ocean values are of the order 20 m/s) is used, short waves that initially satisfy the condition of strong refraction, $c = c_g$, are trapped in low-shear regions and have little to no change in final wavenumber. If the short wave initially has $c_g \ll c$ then he saw a decrease in final wavenumber, on average. It makes sense that those waves that will make it out of the background wave will be those with low wavenumber and large group velocity because they will have the speed to escape the background near-inertial packet. Broutman discovered the strongest focusing of the short waves occurred near locations of strong refraction by unsteady shear, not critical layers. Thus strong interactions with a time-dependent background transport wave properties to lower wavenumbers. This is opposite to weak-interaction theory, which predicts transport to high wavenumbers. It also seems that there is more energy in the test wave after its interaction with the inertial wave, resulting in a damping of the downward-propagating group of inertial waves. Broutman [3] found although there is a large net increase in the energy density of the wave, there is a net decrease in both energy and the wave action because the group of test waves has a larger volume after its interaction with the near-inertial wave packet. Broutman, Macaskill, McIntyre, and Rottman [5] found that through refraction the short waves may exit the time-dependent shear group with a full spectrum of vertical wavenumbers. Observations of overturning near Point Argüello, California lead Alford and Pinkel [1] to believe overturning, as characterized by a jump in strain rate followed by a return to normal values, may result when small-scale internal waves propagating through a slowy varying background flow become unstable.

Bruhwiler and Kaper [7] used ray tracing to better understand the evolution of a distribution of short waves interacting with a single long wave. They defined a frequency spectrum using the number of waves at each frequency. Each of the short waves has the same amplitude, so more waves are necessary for short-wave frequencies which contain more energy. Starting with a realistic short-wave frequency spectrum they found that after a single interaction with a long wave the short waves generally refracted to a higher frequency. This corresponds to a decrease in vertical wavenumber, leading to a decrease in probability of the short-wave breaking after the encounter. Also, through their theory and simulations they expect a flat slope for the short wave frequency energy spectrum, which was initiated with a -2 slope on a log plot, if waves are sent through an inertial wave. But all their tests are linear, the test wave amplitude and horizontal wavenumber are kept constant, and they only test the interaction of upward propagating test waves with a single inertial wave, so the resulting flat energy spectrum may not be representative of realistic conditions in the oceans and atmosphere.

In the atmosphere, Eckermann [12] focused on the omission of the propagation of the other waves in the spectrum when determining the Doppler spreading by a given gravity wave. This approximation has been shown to be invalid as waves are refracted to shorter scales. So ray theory is used to study short-wave refraction within propagating long-wave fields. They find that although turning levels are common, critical levels do not occur if there is no mean wind shear and the waves propagate upwards. Thus the sharp increase in probability of wave breaking beyond the previously decided cutoff vertical wavenumber no longer occurs.

Hertzog, Souprayen, and Hauchecorne [29] use ray paths and an experiment to test the vertical evolution of the vertical wavenumber spectrum in the atmosphere. They start with a background flow produced by both long waves and balanced motion (baroclinic eddies) and launch rays at a constant altitude but with differing vertical wavenumbers and frequencies. The interaction captured by the ray techniques produces an efficient net spectral transfer of wave energy and is almost entirely responsible for the formation of the observed spectra.

Sun and Kunze [54, 55] included vertical divergence of the background and found that it sped up the refraction of the short waves toward small dissipating scales and hence increased the predicted dissipation rate of the HWF model to a value closer to reality.

Sartelet [49, 50] investigated the interaction between single short waves and a single long wave using ray-tracing and two-dimensional numerical simulations in the atmosphere. She compared interactions between short and long waves travelling in the same direction, resulting in critical layer interactions, and in opposite directions, resulting in caustic interactions, to short waves interacting with a steady background shear, resulting in a steady critical layer interaction. Using these comparisons she addressed reflection and transmission of the short waves, the effect changes in the long wave phase speed and amplitude, and the vertical wavenumber cutoff for short wave breaking and resluting dissipation.

Her results for a short wave propagating in a steady shear show that as the frequency of the short wave increases the more likely the short wave is to be totally or partly reflected because of Doppler shifting. When the background is a long wave though, the transmission and reflection of the short wave depend on the direction of the phase speed of the long wave. If the long wave phase speed is in the same direction as the short wave group speed the transmission and reflection are smaller, but if the phase and group speeds are in opposite directions the transmission and reflection are larger. When the phase speed of the long wave is decreased the interaction between the short and long wave is weaker. It is not completely clear whether this is because of the increase in the vertical wavenumber of the long wave, or because of the resulting decrease in amplitude of the long wave in order to keep the minimum background Richardon number constant. These are interesting statistical results of short and long wave interactions, and they raise questions about what is happening during locations of strong refraction in short-long wave interactions that causes these differing results.

Sartelet [49, 50] calculated wave breaking due to refraction of the short waves by either a steady shear or internal waves of realistic scales through a mixed shear and convective adjustment scheme, in which breaking is modeled via both convective and Kelvin-Helmholtz instabilities. She compared the wavenumber cutoff of the short waves (the wavenumber at which the short wave would break) in each case and found when the background flow is time independent (steady shear) there is a sharp transition, at a particular calculated vertical wavenumber, when short waves break and are dissipated. In the cases with a time-dependent background there is no distinct vertical wavenumber of the short waves at which breaking is certain, but her results show breaking is most probable at locations of strong refraction (caustics or critical layers depending on the directional relationship between the long and short wave). She estimates that wave-breaking during interactions when the background is time dependent will occur much less often than when the background is time independent. So using the assumption of steady-shear in the atmosphere may lead to an overestimate of dissipation. This extends to the ocean in that the time-dependence of background shear is a significant factor in the wave-breaking leading to mixing in the ocean.

I.C Summary and Outstanding Issues

We see that to keep the balance of the general circulation in the ocean there is approximately 2 TW of energy dissipation necessary in the deep ocean. The generation and breaking of internal waves over topography may be an important part of this. It has been shown internal wave energy is enhanced over topography, some of which contributes to immediate mixing, and some which propagates away to contribute to mixing elsewhere. It is not yet understood exactly how this mixing is occurring. Of the types of wave-wave interactions, PSI and induced diffusion are the most capable of transferring energy between waves of different frequecies. Although PSI seems to occur in laboratory and numerical simulations, the strength of the mechanism depends on the coherence of the initial wave train. There is not strong observational support of PSI and it can only occur equatorward of 29° latitude.

Also, once these waves have broken down into two waves of half the frequency, they may or may not be down to breaking scales. These waves may still need to interact with other background phenomenon to reach breaking scales and dissipate their energy.

Historically, induced diffusion has been the most successful mechanism in describing the high-frequency wave spectra in the ocean and the spatial dependence of dissipation. The process of internal waves propagating to waves of short enough scales where breaking may occur is a type of this mechanism, but is not yet fully understood. Henyey and Pomphrey made some assumptions about the dissipation of short internal waves as they reached smaller scales which are still being used in some models today. But these dissipation estimates do not take into account the time-dependence of the shear in the ocean and assume a cutoff for wave-breaking based on time independent background shears in the ocean.

Field data have shown that time-dependent shear profiles are more likely to be occurring in the ocean than time-independent shears. Inertial waves created by strong winds at the surface of the ocean propagate downward through the ocean, providing a time-dependent shear for the broad spectrum of wavenumbers present in the upper-ocean to propagate through. Thus it is important to study the effect of time-dependent shear on internal waves, in addition to steady shear, and understand their similarities and differences in the dynamics of the interaction if we are to understand why these past models have worked. It is also important to follow the short waves past the previous assumed cutoff vertical wavenumber for breaking, because when the background flow is time dependent the short waves do not necessarily continue to get smaller and smaller once they reach a certain vertical wavenumber. The short waves may interact with the background wave again, as it is changing in time, and refract to a longer wave, which will not break.

This study will focus on those short waves which may be reaching small breaking scales, since assumptions of steady shear in the ocean may not be accurate. Therefore in this thesis the main mechanism explored to transfer short waves to smaller scales is specifically at induced diffusion, including refraction by steady and unsteady shear. The most basic level, studying the dynamics of individual wave-wave interactions utilizing both numerical and observational techniques, will be covered first. This may give insights into why the more complicated models work so well, and how they might be improved in the future. The background shear will be time-dependent in order to to model a more realistic ocean, which has strong near-inertial shears. Then a statistical analysis of a number of waves propagating through a number of inertial waves is carried out, as this is more realistic than the previous work which has covered only a set of short waves propagating through a single inertial wave, with a single realization. Then observational data is analyzed in an attempt to understand the mechanisms which may be affecting the flow in a particular area of the ocean. Then the signature of this mechanism will be compared to ocean data to see if short-waves propagating through near-inertial shear may be occurring.

I.D Research Objectives

The general objective of this work is to increase the understanding of high frequency, short-scale wave interactions with shears in the ocean. This work will broaden the scope of previous work through analysis of theory, simulations, and comparisons to and analysis of observational data. The main goals of this work are outlined below:

- Achieve a better understanding of a single short wave propagating through a time-dependent shear (in the form of an inertial wave), including how the short waves propagate, what happens when they strongly refract, and where they may reach small enough scales to break and dissipate.

  Investigate, in depth, the changes in short waves as they are refracted strongly by a longer wave. Study changes to the short wave parameters at the location of strong refraction, and compare these dynamics to those of an interaction with a steady shear background. Test validity of ray tracing resluts through fully nonlinear numerical simulations.

- Understand how a distribution of short waves will interact with more complicated time-dependent shear, whether the general trend will be toward breaking.

  Perform a statistical study using two-dimensional ray tracing and adiabatic invariance theory to calculate different spectra of short waves propagating through a number of inertial waves. Test a distribution of short waves propagating through a distribution of inertial waves, as of course many waves are present in the ocean, with energy in the spectrum accounted for by the number of waves (each with the same amplitude).

- Relate numerical simulations to observations, creating a map of the possible ocean profile if the main occurence were short waves interacting with inertial waves.

  Compare data collected over Kaena Ridge, Hawaii, supplied by Professor Rob Pinkel, to the ray tracing and numerical simulations of both the single packet interactions and the statistical study. Relate numerical simulations to collected observational parameters to find footprint of these short-long wave interactions occuring in the ocean

I.E Dissertation Outline

The technical content of this dissertation is arranged into six further chapters:

- Chapter 2 presents a description of the dynamics of a single small-scale wave interacting with a time-dependent background shear in the form of a background long-wave of inertial frequency.

  The basic problem is introduced and parameters are defined. The mathematical formulation for the ray theory and fully nonlinear numerical simulations are included, specifically the governing equations and solution method are discussed. We then solve the equations for a single interaction between a short and long wave. We carry many important parameters through the analysis, including the amplitude of the short wave as it propagates and the changes in the short-wave vertical wavenumber. These parameters are compared to results of an interaction of a short wave with a steady background shear. The differences are clear and show that time-dependence in the background shear can make a significant difference to short-wave behavior. The results lead to an understanding of the necessity of including background time-dependence in future modeling efforts.

- Chapter 3 presents a statistical study of sets of short waves propagating through sets of inertial waves.

  The problem formulation is much like that in the previous chapter, but many simulations are run in order to find a statistical analysis of what a number of waves will do when being refracted by a time-dependent background. In the ray tracing simulations we include thousands of rays propagating through a number of inertial waves to understand the results of having a broad range of internal waves present. These waves are then distributed in frequency space as they may be in the ocean and the results are compared to those of a random set of initial waves. Adiabatic invariance theory is also used to compute the same statistics. The results compare well and we conclude there are significant changes to the short-wave frequency spectrum after the short waves a single or multiple times with the inertial wave packet.

- Chapter 4 presents an analysis of observational data and compares the results to the numerical studies presented in the previous chapters.

  First there is an overview of the data collection process and location of the observations necessary to put the results into the correct context.

  A detailed mathematical description of the data analysis (coherence, phase, etc.) is presented. Then the results of these analysis are discussed. Then we compare these results to those of the fully nonlinear numerical simulations and ray tracing. We find some parameters coincide and believe we are seeing strong interactions between short waves and inertial waves. There are also some results which lead us to the conclusion that these are not the only interactions occurring at this location, as we would expect.

The wave-breaking criteria is also outlined and we create a wave-breaking map for short waves propagating through inertial waves. This is a signature of what one may see in the ocean if the proposed short-long wave interactions are occurring. If such relationships are not strong, it is possible this mechanism of leading waves to breaking is not dominant in that particular location.

- Chapter 5 concludes the dissertation with a summary of significant findings of this investigation. Through the simulations and observational analysis we have found considerable evidence that interactions of short internal gravity waves with time-dependent shears are vastly different from interactions of these waves with time-independent shear. These differences lead to different probable locations of wave breaking of the short waves, and in some instances breaking will not occur where it was previously thought to if a steady shear was present. These new locations calculated for wave breaking of short waves, as well as calculations of short wave activity, coincide well with breaking locations and short wave activity calculated for data from observations.

  Suggestions for further work are also discussed.

II

Dynamics of a Single Short - Long Wave Interaction

We compare the results of ray tracing to numerical simulations. We also discuss the differences between the dynamics of an interaction between a short wave and a steady background shear, and the interaction of a short wave with an unsteady background shear (long inertial wave).

After the basic setup of the problem is described, the governing equations for ray theory are shown, and the equations necessary to solve the fully non-linear problem are also described. Then the results are presented for both the ray tracing and numerical simulations. There are three general outcomes for different short wave packets propagating through a longer wave packet. These are called first, second, and third kind encounters. The dynamics of each will be described in more detail throughout the chapter.

II.A Idealized Problem Set-up

In the numerical simulations and ray tracing we consider the situation in which a single packet of short waves approaches a single packet of inertia waves either from above or below. Fig. II.1 depicts the initial wave situation with the

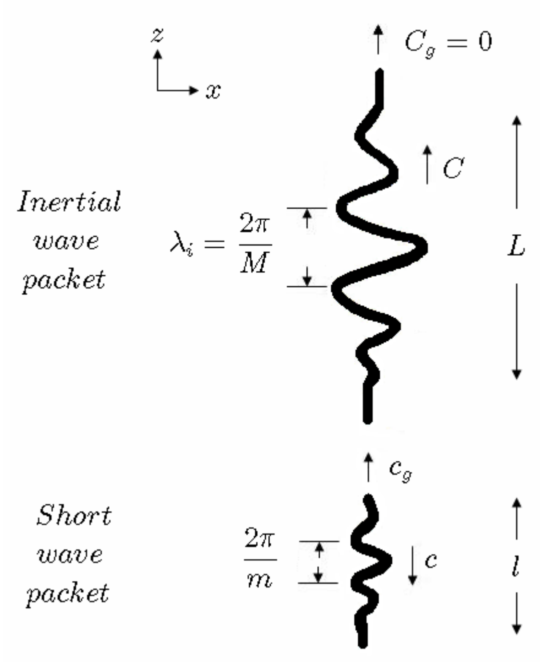

Figure II.1: Schematic of a short wave packet approaching an inertia-wave packet with basic parameters shown.

short wave below the inertia wave in this case. The coordinate system is (x, y, z) with z positive upwards.

The waves of the inertia-wave packet have wavenumber $\mathbf{K} = (0, 0, M)$, where $M = 2\pi/\lambda_i$ and λ_i is the vertical wavelength of the inertial wave. The frequency of the background is defined as the Coriolis or inertial frequency, f, thus the name inertia-wave. The Coriolis frequency is defined by the rotation of the earth, which is approximately 1 cycle/day, but decreases as you travel from the equator poleward. We will assume it is constant. We also define an inertial period as $T_i = 2\pi/f$. The velocity field of the inertia-wave is a purely horizontal, time-dependent current $\mathbf{u} = (u, v, 0)$ extending infinitely far in the horizontal, but confined in the vertical by a Gaussian envelope:

$$u + iv = u_0 \, e^{-z^2/L^2} e^{i(Mz - ft)} \tag{II.1}$$

where L, the envelope size, and u_0, the maximum horizontal velocity of the background, are constants, real and complex respectively.

The short waves can be defined by their vertical displacement field:

$$\zeta(x,z,t) = \mathrm{Re}\left\{\zeta_0\, e^{-(z-z_0)^2/\ell^2} e^{i(kx+ly+mz-\hat{\omega}t)}\right\} \tag{II.2}$$

where ℓ, the short wave envelope size, and z_0, the initial vertical position of the short wave, are real constants and ζ_0 is a complex constant. The vertical displacement of the short waves can also be written $\zeta = \zeta_0 \exp(i\theta)\exp -(z-z_0)^2/\ell^2$, from which the wavenumber and wave frequency are given by $\mathbf{k} = \nabla\theta$ and $\omega = -\theta_t$, respectively, and where $\omega = \hat{\omega} + ku$.

The wave-energy density E is related to ζ_0 by

$$E = \frac{1}{2}\rho_0\zeta_0^2 N^2\left[1 + \left(\frac{fm}{Nk}\right)^2\right] \tag{II.3}$$

where ρ_0 is the mean density of the fluid. The wave-action density $A = E/\hat{\omega}$.

The short waves have wavenumber $\mathbf{k} = (k, l, m)$, with k constant, and intrinsic frequency $\hat{\omega}$, which is the Doppler-shifted frequency, which are related through the dispersion relation

$$\hat{\omega}^2 = (N^2k^2 + N^2l^2 + f^2m^2)/(k^2 + l^2 + m^2) \tag{II.4}$$

which simplifies to

$$\hat{\omega}^2 \approx \frac{N^2k^2}{m^2} \tag{II.5}$$

when $f^2 \ll \hat{\omega}^2 \ll N^2$ and $l = 0$. We take k and $\hat{\omega}$ to be positive, and allow m to have either sign. N is the Brunt-Väisälä buoyancy frequency, related to the natural frequency of a particle if it were displaced from its equilibrium position within a stably stratified fluid. It is a measure of the strength of stratification of the fluid, the larger N is the stronger the stratification. Where N^2 is defined as

$$N^2 = -\frac{g}{\rho_0}\frac{d\rho}{dz} \tag{II.6}$$

and g is the acceleration of gravity and ρ_0 is the mean density of the fluid.

Other important parameters of the problem which are necessary to define in order to understand the following equations include the group and phase speed of the short wave packets. The group velocity, c_g, is defined as the velocity at which the short wave packet travels. The energy travels at the group velocity.

$$c_g = \frac{\partial \hat{\omega}}{\partial \mathbf{k}} \ . \tag{II.7}$$

The phase speed, c, is the speed at which the phases of the short wave travel through the group. For internal gravity waves the phases travel perpendicular to the direction in which the group velocity travels.

$$c = \frac{\hat{\omega}}{\mathbf{k}} \ . \tag{II.8}$$

II.A.1 Initial conditions

For the fully nonlinear numerical simulations the computational domain contains one horizontal wavelength of the short waves in the horizontal direction and one vertical wavelength of the inertia waves in the vertical direction. There are 512 grid points in the vertical direction, but only 8 grid points in the horizontal direction. The low horizontal resolution suffices for this problem – as has been verified by tests at higher resolution – because the short waves, though strongly refracted, are not strongly amplified, and remain well below breaking threshold. Periodic boundary conditions are imposed in both the x- and z-directions. The maximum wave-steepness $\partial\zeta/\partial z$ of the short waves over the duration of the simulation is only about twice its maximum value at the initial time, chosen to be 0.1. No viscosity or filtering was necessary to stabilize the calculation. (An initial steepness of 0.2, however, leads to computational instability at this resolution if no filtering is employed.)

For the numerical results shown, we use the following parameter values, which are characteristic of internal waves in the deep ocean at mid-latitudes: $M/k = 2$, $N/(Mu_0) = 2.4$, and $N/f = 75$. In the ray-tracing integrations to catagorize the types of interactions possible we use $ML = 2\pi$. For the numerical simulations, the initial steepness $|\zeta_z| = |m\zeta_0| = 0.1$, where subscript z represents the partial derivative with respect to z, $ML = \pi/5$ (this value will be used in the ray tracing as well to compare to numerical simulations), and $\ell/L = 0.75$. We will use the typical value $M = 2\pi/(100\,\mathrm{m})$ in the deep ocean and $f = 10^{-4}\,\mathrm{s}^{-1}$, which with the above parameters yields $u_0 = 0.05\ \mathrm{m\,s}^{-1}$.

II.B Ray Theory

Using ray theory we can calculate approximately the behavior of the short wave encounter with the inertial wave group. To do this we assume that the inertial wave is both unaffected by the short wave interaction and has a much larger length scale than that of the short wave. Also we assume the short wave is determined by the linear dispersion relation. Then an evolution equation in characteristic form can be found for $\mathbf{k}$.

II.B.1 The ray equations

The ray tracing equations are a set of equations that define the path on which a short wave packet will travel. Therefore the group speed of the short wave packet, c_g, is defined as the change in spatial location over time:

$$\frac{d\mathbf{x}}{dt} = c_g \ . \tag{II.9}$$

The equations for wavenumber and wave frequency mentioned earlier, $\mathbf{k} = \nabla\theta$ and $\omega = -\theta_t$, respectively, where $\omega = \hat{\omega} + ku$, will help define the second main ray equation. If we switch to the inertial-wave reference frame, which is important for the Doppler shifting, the short wave frequency becomes

$$\Omega = \hat{\omega} + ku - Cm \tag{II.10}$$

where $C = f/M$ is the phase speed of the inertial wave.

We then relate these equations for wavenumber and wave frequency by taking the time derivative of $\mathbf{k}$ and setting it equal to the spatial derivative of Ω. Then

$$(\nabla\theta)_t = \mathbf{k_t} \tag{II.11}$$

$$\nabla\theta_t = \nabla\Omega \ . \tag{II.12}$$

Then:

$$\mathbf{k_t} = \nabla\boldsymbol{\Omega} \ . \tag{II.13}$$

We are mainly interested in the changes in the vertical, as the background long wave which is purely horizontal will only effect the vertical wavenumber of the short wave. For the vertical position of the ray path and the vertical wavenumber respectively:

$$\frac{dz}{dt} = c_g, \qquad \frac{dm}{dt} = -k\frac{\partial u}{\partial z} \ . \tag{II.14}$$

Here $d/dt = \partial/\partial t + c_g\partial/\partial z$. Because the expression (II.1) has no dependence on x, the horizontal components $(k, 0)$ of the wavenumber of the short waves are conserved along the ray. Thus k is constant. To predict wave steepness a set of additional equations based on wave-action conservation is integrated. These equations, which are described by Broutman [3] and here below, make consistent allowances for structure near caustics in view of its likely importance for wave-breaking thresholds.

The following three equations furnish the ray amplitude:

$$\frac{dV}{dt} = VG_{mm}\frac{\partial m}{\partial z} \ , \tag{II.15}$$

$$\frac{d}{dt}\frac{\partial z}{\partial z_0} = G_{mm}\frac{\partial m}{\partial z_0} \ , \tag{II.16}$$

$$\frac{d}{dt}\frac{\partial m}{\partial z_0} = -G_{zz}\frac{\partial z}{\partial z_0} \ , \tag{II.17}$$

where $\omega(z,t) = G(m,z,t)$. We use G and denote partial derivatives by subscripts when m is to considered with z and t as an independent variable. Since there are frequent caustics, the ray equations are expressed in terms of V, which measures the volume of a ray tube and hence vanishes at the caustic. The quantity V is essentially the inverse of the wave-action density, the only difference being that V

changes sign each time the ray intersects the caustic. In (II.16)-(II.17) we treat m and z as functions of their initial position z_0. The solutions of (II.16)-(II.17) combine to give

$$\frac{\partial m}{\partial z} = \frac{\partial m/\partial z_0}{\partial z/\partial z_0} \tag{II.18}$$

which is required to integrate (II.15). The full expressions for (II.15)-(II.17) include terms proportional to G_{mz}, which is zero under present assumptions (as of course is G_x). More information on the amplitude integration was accomplished by Broutman [3], whose implementation is based on the theory of Hayes [25].

II.B.2 Caustics and Critical layers

We now turn to the problem of computing short-wave amplitudes at ray singularities known as caustics, which occur in this problem near depths where $c_g = c$. Caustics occur where the slowly-varying assumption on which ray-tracing is based, breaks down, producing infinite amplitudes that do not occur in the full linear problem. We consider two measures of the short-wave amplitude: the wave-steepness, defined as ζ_z, where ζ is the vertical displacement of the short waves; and a component of the wave-induced shear u'_z, where u' is the x-component of the particle velocity of the short waves.

In the ray approximation, the wave-steepness ζ_z has a magnitude $|m\zeta_0|$ that reaches unity when the short waves are about to overturn. For $\hat{\omega} \ll N$, the wave steepness is related to the wave-action density A by

$$|\zeta_z| = k\ (2/\rho_0)^{1/2}\ A^{1/2}\ \hat{\omega}^{-1/2}\ . \tag{II.19}$$

This is derived from the dispersion relation and (II.3). The wave-induced shear u'_z is related to the wave-action density in the ray approximation by

$$|u'{}_z| = Nk(2/\rho_0)^{1/2}\hat{\omega}^{-1/2}(1 - f^2/\hat{\omega}^2)^{-1/2}A^{1/2} \tag{II.20}$$

when $\hat{\omega} \ll N$. The values of $|\zeta_z|$ and $|u'_z|$ are in fact computed in our ray integrations from the more general formulae in which the low frequency approximation $\hat{\omega} \ll N$

is not made. It suffices to plot only $|u_z'|$, since when normalized by their initial values the above solutions for $|u_z'|$ and $|\zeta_z|$ differ only by the multiplicative factor $N(1 - f^2/\hat{\omega}^2)^{-1/2}$, which is a function of z.

The short-wave amplitude near a caustic can be estimated by applying standard Airy-function techniques to the case of a purely sinusoidal inertial wave in which the frequency Ω defined in (II.10) and the wave-action flux B defined in (II.24) are constants. Let the ray solution be given in the form

$$a = a_0(z,t)e^{i\theta} \tag{II.21}$$

where $\mathbf{k} = \nabla\theta$ and $|a_0^2| = A$ is the wave-action density. Let the amplitude near the caustic be of the form $A_0 Ai(\rho)$, where Ai is the Airy function and ρ is a nondimensional distance from the caustic. Then as Broutman [3] showed,

$$A_0 = |\pi B|^{1/2}\left(\frac{32}{\Omega_{mm}^2\Omega_z}\right)^{1/6} \tag{II.22}$$

where Ω_{mm} and Ω_z are evaluated at the caustic. Making use of (II.5) reduces (II.22) to

$$A_0 = \left|\frac{2\pi B}{kN}\right|^{1/2} Ri_c^{1/12}|m_c| \tag{II.23}$$

where we define $Ri_c = N^2/u_z c^2$ to be the Richardson number, a nondimensional parameter relating the potential to kinetic energy, at the caustic.

II.B.3 Analytic ray solutions

An analytic ray solution describing short-wave refraction by inertia waves appears in Broutman and Young [6] and is obtained by letting L approach infinity in (II.1). The inertia-wave velocity $\mathbf{u}$ is then purely sinusoidal. In a reference frame moving at the inertial-wave phase speed c, the inertial current appears steady. Solutions then exist for which the short-wave frequency in the inertial-wave reference frame, Ω, and the vertical flux of wave-action in the inertial-wave reference frame

$$B = (c_g - c)A \tag{II.24}$$

are constants.

For our idealized model, caustics occur when

$$c_g = c \; . \tag{II.25}$$

Though derived for the case of infinite L in (II.1), (II.22) and (II.23) probably give reasonable approximations when the inertia waves are localized by an envelope, provided that B and Ω vary slowly, on the envelope scale L. Both B and Ω are easily computed during the ray integration, so this slowly varying assumption can be checked, and if satisfied (II.22) can be used to estimate the maximum amplitude near the caustic from the numerical ray solutions.

A simplification of (II.23) is appropriate when the refraction is strong enough to make $|m| \gg |m_c|$ on one side of the caustic. Then $c_g \ll c$ and the conservation of wave-action flux (II.24) forces A to be approximately constant. Let that value be A_*. Substituting $B \approx cA_*$ in (II.23) and using

$$m_c \approx -\left(\frac{MkN}{f}\right)^{1/2} = -\left(\frac{kN}{c}\right)^{1/2} \; . \tag{II.26}$$

gives a relationship between A_* and the caustic amplitude A_0

$$A_0 = (2\pi)^{1/2} Ri_c^{1/12} (A_*)^{1/2} \; . \tag{II.27}$$

The Airy function attains the maximum value of approximately 0.54 near the caustic. Thus a caustic-correction formula relating the maximum wave-action density $A_{\max}$ near the caustic to the ray prediction A_* is

$$A_{\max} \approx 1.8 Ri_c^{1/6} A_* \; . \tag{II.28}$$

To determine the corrected value for $|u_z'|$ near the caustic, we start with the caustic correction for the wave-action density A in (II.24). The subscript max denotes the maximum corrected value near the caustic, making the appropriate Airy correction and taking into account the fact that the Airy function reaches its peak on the illuminated side of the caustic. The subscript c denotes the value right at the caustic, and $Ri = N^2/{u_z}^2$. A_* is the value of A away from the caustic in the direction along the short-wave ray of decreasing vertical group speed c_g. We shall see in the next section that the wave-action density quickly approaches the value of A_* where $c_g \ll c$.

Next we assume that near the caustic, $|u'_z|$ is related to A by the same ray formula (II.20) that relates $|u'_z|$ and A away from the caustic. The justification behind this assumption is that the Airy function correction valid near caustics associated with $c_g = c$ describes the envelope of the short waves, and within this envelope the short waves are sufficiently slowly varying that the ray-theory relationship between A and $|u'_z|$ still holds to a first approximation. Using (II.24) to evaluate (II.20) near the caustic gives

$$\begin{aligned} &|u'_z|_{\max} \sim Nk(2/\rho_0)^{1/2}\times \\ &1.8^{1/2} Ri_c^{1/12} {A_*}^{1/2} {\hat{\omega_c}}^{-1/2} (1 - f^2/{\hat{\omega_c}}^2)^{-1/2} \ . \end{aligned} \tag{II.29}$$

Introducing the subscript zero to denote an initial value, we then obtain

$$\begin{aligned} &\frac{|u'_z|_{\max}}{|u'_z|_0} = \\ &1.8^{1/2} Ri_c^{1/12} \left(\frac{A_*}{A_0}\right)^{1/2} \frac{{\hat{\omega_0}}^{1/2}(1 - f^2/{\hat{\omega_0}}^2)^{1/2}}{{\hat{\omega_c}}^{1/2}(1 - f^2/{\hat{\omega_c}}^2)^{1/2}} \ . \end{aligned} \tag{II.30}$$

All quantities in (II.30) are easily determined in the numerical ray integrations. We do not actually match the ray solutions to the Airy function. Instead we simply show plots in which the solution for $|u'_z|$ near the caustic is clipped to the maximum value as calculated from (II.30).

After a strong refraction at the caustic, the properties of the short wave change. The vertical wavenumber increases (decreases) and the frequency decreases (increases), resulting in a decrease (increase) in vertical group speed of the short wave packet. A cartoon of this idea is shown in Fig. II.2. Each drawn short-long wave set is a different snapshot in time and shows how after a strong refraction the previous explained changes occur to the short wave packet.

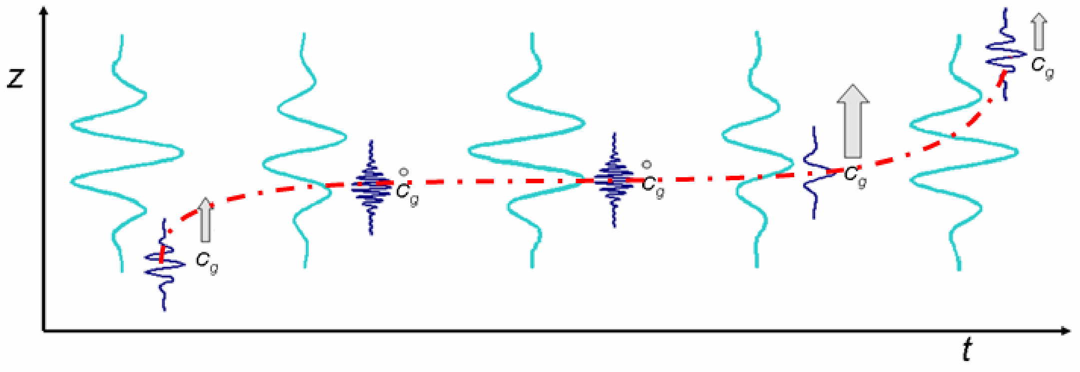

Figure II.2: Schematic of a short wave packet propagating through an inertia-wave packet. Dot-dashed line corresponds to the ray. Each short and long wave drawn is for a different snapshot in time.

The vertical wavenumber m_c of the short waves at the caustic is defined by equation (II.26), which is derived using $c_g \approx kN/m^2$, which follows from (II.5). In this approximation Broutman and Young [6] find from (II.10) that the value of u at the caustic is

$$u_c \approx \frac{\Omega}{k} - 2\left(\frac{Nc}{k}\right)^{1/2} . \tag{II.31}$$

Although substantial refraction occurs in many cases for both the free and trapped solutions, the strongest *focusing*, where a defined ray tube shrinks in diameter, of the short-wave rays occurs at the caustics, where the ray tube will vanish, and these are found only in the trapped solutions. Therefore the trapped solutions are of special interest and are singled out for additional discussion in the next subsection.

A useful result for inertia wave packets of finite length can be obtained by noting that typically in our calculations Ω takes approximately the same value before and after the encounter. This implies that large permanent changes in the vertical wavenumber of the short waves can result from the encounter, as we now show. Let the subscript i denote an initial value, before the encounter, and the subscript f denote a final value, after the encounter. Then since u_i and u_f are zero, outside the envelope of the inertia wave $\Omega_i = \Omega_f$ implies from (II.10) that

$$\left(\frac{kN}{m_f m_i} + c\right)(m_f - m_i) = 0 , \tag{II.32}$$

where again we have used the approximation (II.5). Thus $m_f = m_i$ is one possible outcome of the encounter. Alternatively the first factor in (II.32), using (II.26) gives

$$\frac{m_f}{m_c} = \frac{m_c}{m_i} \; . \tag{II.33}$$

II.C Numerical ray solutions

We have calculated numerical solutions of the ray equations for a wide variety of short-wave and background inertia wave groups. For a slowly varying packet of inertial waves, these numerical ray integrations indicate that the analytical solutions for the special case of an inertia-wave train provide useful approximations. Caustics coincide approximately with $c_g = c$; and the frequency Ω varies slowly along the ray – more slowly than variations in m or $\hat{\omega}$ (see Figs. 5 and 6 of Broutman [3]).

Encounters between short waves and inertia waves, in which $c_g = c$ is satisfied at some stage during the encounter, can be divided into three classes depending on the value of c and on the initial value of c_g, say $c_g = c_{g0}$ at $t = 0$. Sample ray calculations for these three classes, which we will refer to as encounters of the first, second and third kinds, are described in the next three subsections.

II.C.1 Encounters of the first kind $c_{g0} \gg c$

In the first-kind encounter the short-wave group approaches the inertial-wave packet with small vertical wavenumber and large vertical group velocity. The initial wavenumber in this example is $m = -3k$, giving the initial values $\hat{\omega} \approx 24f$ and $c_g \approx 17c$. The results of the ray integration are plotted in Fig. II.3. In each case the time, in inertial periods, is given on the horizontal axis. The depth of the ray path (upper left) is measured in wavelengths of the inertial wave ($\lambda_i = 2\pi/M$) relative to the center of the inertial-wave packet at $z = 0$. The wave-action density A and short-wave shear $|u'_z|$ are normalized by their initial values.

The shaded, quasi-elliptical regions in Fig. II.3a show the phase propagation of the inertia waves: more precisely, the long axis of each shaded region marks the

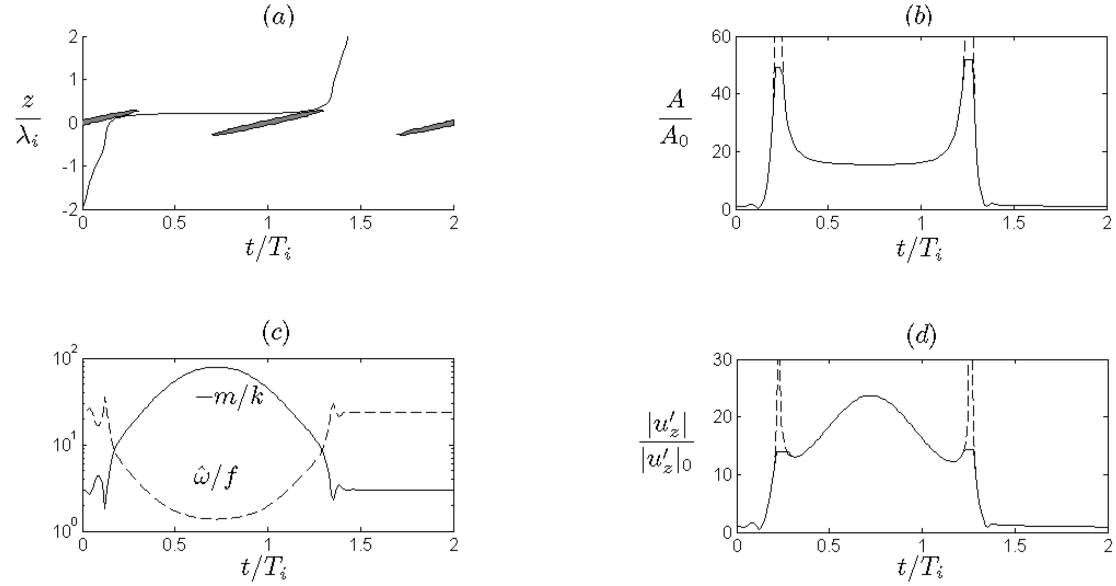

Figure II.3: An encounter of the first kind: (a) the ray path, where the boundaries of the shaded, quasi-elliptical regions mark the locations where, at a given instant t, the strong-refraction condition $c_g = c$ can be satisfied (see text); (b) the wave-action density of the short waves, normalized by its initial value, with the dotted line indicating the singular ray solution, and the solid line clipped to indicate the maximum value, $A_{\max}$, near the caustic, where $A_* = 15.5$; (c) the vertical wavenumber (solid line) and intrinsic frequency (dashed line); (d) the short-wave shear $|u'_z|$ normalized by its initial value, with the dotted line indicating the singular ray solution and the solid line clipped to indicate the maximum amplitude near the caustic. All plots have the same horizontal axis, the time in inertial periods.

spacetime locus of a crest or maximum in the u field of the inertia wave. Each quasi-ellipse, i.e., the boundary of each shaded region, marks the approximate depths and times (to leading order in the slow-modulation approximations for the wave packets) at which $c_g = c$ can be satisfied for the given wave parameters.

Since the initial vertical wavenumber of the short-wave group in this example is $m_i \approx m_c/4$, we expect from (II.33) that some short-wave groups entering into the inertial-wave packet at a different phase of the inertial wave will emerge from the encounter with their wavenumber increased by a net factor of about 16. Only in a small number of cases, however, does the final wavenumber actually increase in magnitude to the larger value whose possibility is predicted by (II.33). The reason why high-wavenumber outcomes are uncommon is that at high wavenumber the short-wave group propagates very slowly and is therefore unlikely to escape from the inertial-wave packet before the next crest of the inertial wave catches up with the short-wave group and refracts the short-wave group to low wavenumber and fast group velocity [6], [7]. In most cases, therefore, first-kind encounters conclude with $m_i \approx m_f$. For this example, the final value of the vertical wavenumber is $m_f = -3.01k = 1.003m_i$. Permanent changes are more likely in third-kind encounters.

Fig. II.3 illustrates one of the most important points about the refraction of short internal waves by an inertia wave: the refraction is strongest where $c_g \approx c$, and not (necessarily) where the inertial shear is strongest or where the short-wave wavenumber is largest. A second important point, to be addressed further in the next section, is that between the caustics in Fig. II.3, the wave-action density levels off to an approximately constant value, A_*. This is predicted from (II.24), which indicates that a constant wave-action flux B implies an approximately constant wave-action density A when $c_g \ll c$.

We apply the caustic correction formula (II.28), using $A_* \approx 15$ and Ri_c approximately 27 and 35 at the first and second caustics respectively. The corrected value of A near the caustic is then approximately 50. The maximum value for $|u'_z|$ near the caustic, corrected for the ray singularity using (II.29), is indicated on the plot for $|u'_z|$. The solid line is clipped at this maximum value, while dotted lines represent the singular ray solution.

As regards its relevance to short-wave dissipation, therefore, this first strong refraction resembles the refraction toward a critical level in steady shear *except* that the steepness is amplified by a finite factor only, reducing though not eliminating the likelihood of wave breaking. Fig. II.4 contrasts the focusing of rays in a first-kind encounter (left column) with the focusing of rays in a non-rotating critical layer situation of the classic Booker and Bretherton type (right column). The left column has $m/k = -3$ initially and is the same case as shown in Fig. II.3; the classic critical-layer case, the right column of Fig. II.4, has $m/k = -5$ initially and $f = 0$ throughout, i.e., $f = 0$ both in (II.1) and also in the short-wave dynamics. For the first-kind encounter, five rays are shown, each originally separated in time by a sixtieth of an inertia period. After the short-wave rays glance the $c_g = c$ quasi-ellipse, they propagate into a region of stronger shear while refracting to still higher vertical wavenumber. However, the short-wave focusing weakens as the inertia-wave shear strengthens. This is clear from the plot: the rays become parallel.

As explained by Broutman, Macaskill, McIntyre, and Rottman [5], the wave-action density A becomes approximately constant as the rays become parallel. This can be anticipated theoretically using arguments similar to those of Broutman and Young [6]: in the reference frame moving vertically at the phase speed of the inertia waves the vertical flux of wave-action density, $(c_g - c)A$, is approximately constant, and therefore

$$c_g A \simeq \text{constant} \qquad \text{whenever} \qquad c_g \gg c \tag{II.34}$$

$$A \simeq \text{constant} \qquad \text{whenever} \qquad c_g \ll c\ . \tag{II.35}$$

The limit of constant $c_g A$ is relevant to many steady-shear refraction and critical-layer models, and it is this limit that Hines [31] assumes from the very start of his analysis. But at high vertical wavenumbers for which $c_g \ll c$, it is the wave-action density A, not the wave-action flux that becomes constant. This is similar to the steady-shear refraction model proposed by Phillips [45] (included in the first edition only) and related to the original sheared-disturbance theory of Thomson [59], in which the short-wave rays do not converge but instead remain parallel during the refraction.

In a model such as ours, a quantity that measures the degree of ray focusing is $m^{-2}\partial m/\partial z$. This is the fractional change in the vertical wavenumber over a vertical distance of m^{-1}. Its value can be computed in a ray calculation, and in fact $\partial m/\partial z$ is required anyway to calculate the wave-action density from (II.15). When neighboring rays cross at a caustic $m^{-2}\partial m/\partial z$ diverges. When neighboring rays are parallel $m^{-2}\partial m/\partial z$ vanishes. Fig. II.4 includes a plot of $m^{-2}\partial m/\partial z$, computed numerically for the first ray to reach the caustic in the upper left plot of Fig. II.4.

Consider again the simple ray model (subsection II.B.3) for the case of an inertia wave that is infinite in extent, i.e. with no Gaussian envelope. In the reference frame moving vertically at the phase speed of the inertia wave we find a steady ray solution for $m^{-2}\partial m/\partial z$. In the limit $\hat{\omega}^2 \ll N^2$ we have from (6), $(c_g - c)\partial m/\partial z = -ku_z$, so that

$$\frac{1}{m^2}\frac{\partial m}{\partial z} = -\frac{u_z}{N}\left[\frac{1}{(1-f^2/\hat{\omega}^2)^{1/2} - m^2/m_c^2}\right] \tag{II.36}$$

where we have used $c = c_g(z_c) \approx kN/{m_c}^2$ to obtain the above expression.

If we first consider a steady shear by letting $c \to 0$ and consequently $m_c \to \infty$, we find that $m^{-2}\partial m/\partial z$ is proportional to the local shear u_z. Thus, if rotation is ignored the rays will approach a critical layer sharply focused if the shear is strong. An example of focused rays approaching a critical layer (without rotation) is shown in the right column of Fig. II.4. If rotation is included, ray theory itself breaks down in the approach to a critical layer, as $\hat{\omega} \to f$, and ray theory's slowly varying approximation is violated. But for time-dependent inertial shear, i.e. nonzero c and finite m_c, the combined limit of large vertical wavenumber m and $\hat{\omega} \to f$ becomes one of vanishing $m^{-2}\partial m/\partial z$.

The Phillips limit illustrates that strong refraction is not the same as strong focusing. In the Phillips limit (II.35), unlike limit (II.34), the wave-energy density

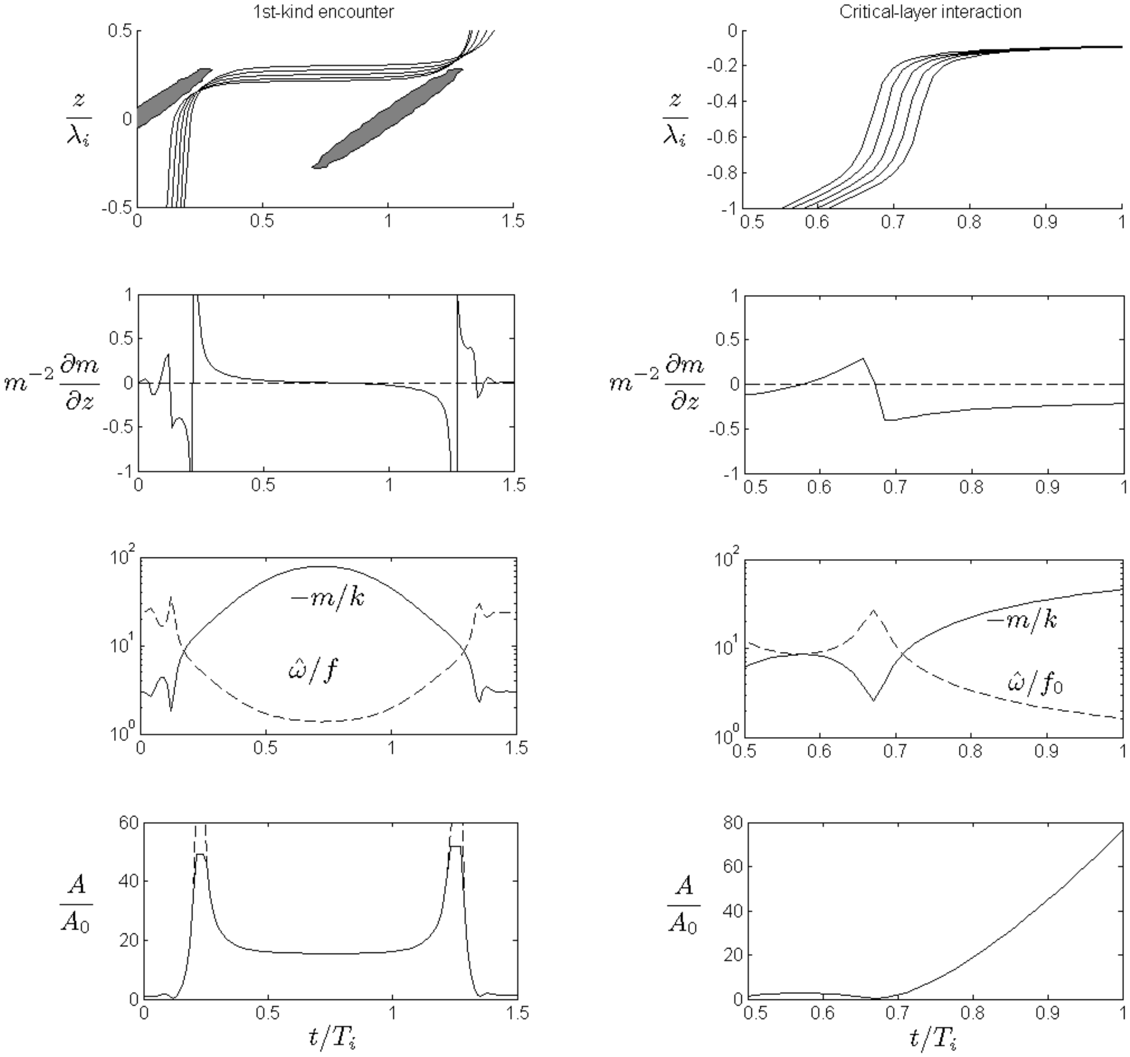

Figure II.4: Comparison of the first-kind encounter (left column) with the approach to a critical layer (right column). The plots of $m^{-2}\partial m/\partial z$, m, $\hat{\omega}$, and A are for the first ray in the corresponding upper plot. For the first-kind encounter $m_{initial}/k = -3$. The rays originate from $z = -2\lambda_i$ every $1/60^{th}$ of an inertial period starting from $t = 0$. The wavenumber and wave-action density plots are identical to Fig. II.3 (redrawn for convenience). For the critical-layer calculation $m_{initial}/k = -5$. Since $f = 0$ in the critical-layer calculation, the time axis and intrinsic frequency $\hat{\omega}$ are scaled by $2\pi/f_0$ and f_0 respectively, where $f_0 = N/75$. The rays originate from $z = -4\lambda_i$ at intervals of $1/60^{th}$ of $2\pi/f_0$.

(II.3) decreases as the vertical wavenumber m increases, as seen in Fig. II.4. Wave-induced shear and wave steepness increase as m increases, but at a slower rate than they would if the wave-action flux, rather than the wave-action density, were constant. An internal wavefield which obeys the Phillips limit rather than limit (II.34) may be able to sustain larger amplitudes at lower wavenumber without saturation at high wavenumber.

II.C.2 Encounters of the second kind $c_{g0} \approx c$

These short waves, with $m/k = -12.25$ initially, satisfy $c_g = c$ immediately upon entering the inertia-wave packet. But, despite this, refraction is weaker than in the first-kind encounter, because the short-wave group becomes trapped around the low-shear trough of the inertia wave midway between two shaded regions. We refer to this case as an *encounter of the second kind*.

The initial condition for the second kind encounter in Fig. II.5 is $m = m_c \approx -12.25k$, or $\hat{\omega} \approx 6.2f$. These short waves find caustics immediately upon entering the outer fringes of the inertial-wave packet. Nine caustics occur during the encounter. Toward the center of the inertial-wave packet the quasi-ellipses expand in size, as the caustics migrate toward the nearest trough of the inertial waves. Hence the short waves are trapped by refraction in a region of low inertial shear and experience smaller variations in vertical wavenumber than those experienced in first-kind and third-kind encounters. The equation (II.33) suggests that the final wavenumber should be close to the initial one, as both roots of that equation predict $m_f = m_i$. The ray integration gives $m_f = -9.8k$, the discrepancy being attributed to a net change in Ω.

II.C.3 Encounters of the third kind $c_{g0} \ll c$

In third-kind encounters, the short waves approach the inertial-wave packet very slowly. The ray integration in Fig. II.6 is initialized with $m/k = -30$ or

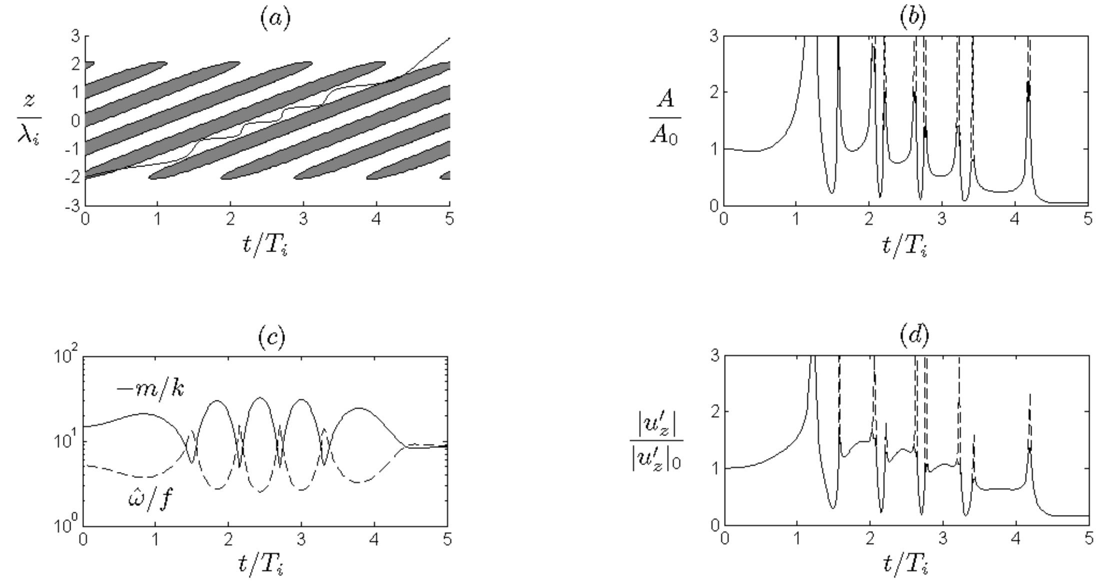

Figure II.5: An encounter of the second kind. Plot details are as in Fig. II.3, but note the different scalings on the time axes, and that, despite appearances, the inertia wavenumber M and packet envelope scale L are the same; it is only the short-wave parameters and the location of the condition $c_g = c$ that vary. The values for A_* in (b) in order of occurrence are: 0.96, 0.75, 0.51, and 0.23.

$\hat{\omega} = 2.7f$, implying $c_g \approx 0.17c$ The first 6 inertial periods are omitted from the plots.

Despite their slow propagation, the short waves never find critical layers, as they would in a steady current of similar strength. (The horizontal phase speed of the short waves is less than $0.2u_0$ before the encounter.) Nor is there much amplification near the caustics, relative to the initial amplitude, when correction is made to the singular ray solution.

The post-encounter wavenumber is $m/k \approx -3.6$. Equation (II.33) predicts $m_f/k \approx -4.3$, but was derived assuming that the initial and final values of Ω are the same, whereas in this example they are different by about a factor of 1.2. This large permanent decrease in the vertical wavenumber is a common outcome of third-kind encounters, as illustrated in Figs. 7 and 9 of Broutman and Young [6], and in many examples provided by Bruhwiler and Kaper [7]. We call this effect the *wavenumber downshift*. If this were a steady depth-dependent current, instead of

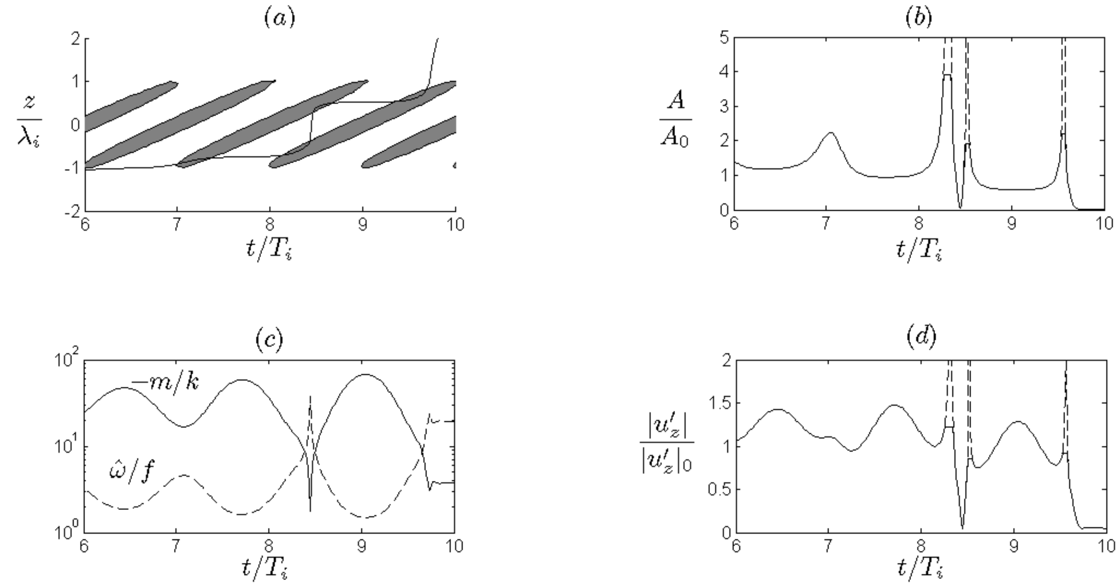

Figure II.6: An encounter of the third kind. Plot details are as in Fig. II.3, but note the different scalings on the time axes, and that, despite appearances, the inertia wavenumber M and packet envelope scale L are the same; it is only the short-wave parameters and the location of the condition $c_g = c$ that vary. The values for A_* in (b) in order of occurrence are: 0.95, 0.6, and 0.2.

a time-dependent one, the wavenumber downshift would be impossible as it would violate the conservation of the frequency $\hat{\omega} + ku$ along the ray. The conservation of Ω leads instead to a quadratic formula for m, permitting different initial and final wavenumbers.

As a result of the wavenumber downshift, the short-wave group expands in size as it leaves the inertial-wave packet. This is because during the downshift the leading edge of the short-wave group momentarily climbs upward at a faster speed than the trailing edge. Since the integral of the wave-action density over the volume of the short-wave group is constant, the wave-action density itself must decrease, as indicated in the bottom panel of Fig. II.6. Changes to the inertial waves as the result of this encounter are discussed by Broutman and Grimshaw [4].

Now recall that short waves entering into the first-kind encounter face intense focusing and amplification near their initial caustic. If the short waves are to propagate past the caustic without breaking, and hence persist into the Phillips high-wavenumber regime, the short waves must initially have very small amplitude with very low frequency. Here is a scenario for how this might happen in the ocean.

Suppose small-amplitude short wave groups are generated at low frequency (where the sources of oceanic internal waves – at least large-scale internal waves – are most energetic), and then interact with large-scale internal waves. They initially enter into third-kind encounters, but thereafter are more likely to participate in first-kind encounters because of the wavenumber downshift – the net decrease in vertical wavenumber. Thus third-kind encounters may evolve into first-kind encounters. As illustrated in Fig. II.6 of the present paper, and by Broutman and Young [6], such third-kind encounters culminate with short waves of greatly reduced wave-action density and wave-induced shear. Hence the amplification in the subsequent first-kind encounter would only restore the short waves to their original but small amplitude.

We will refer to those first-kind encounters that evolve from third-kind encounters as *upgraded* first-kind encounters, or simply upgraded encounters. An ex-

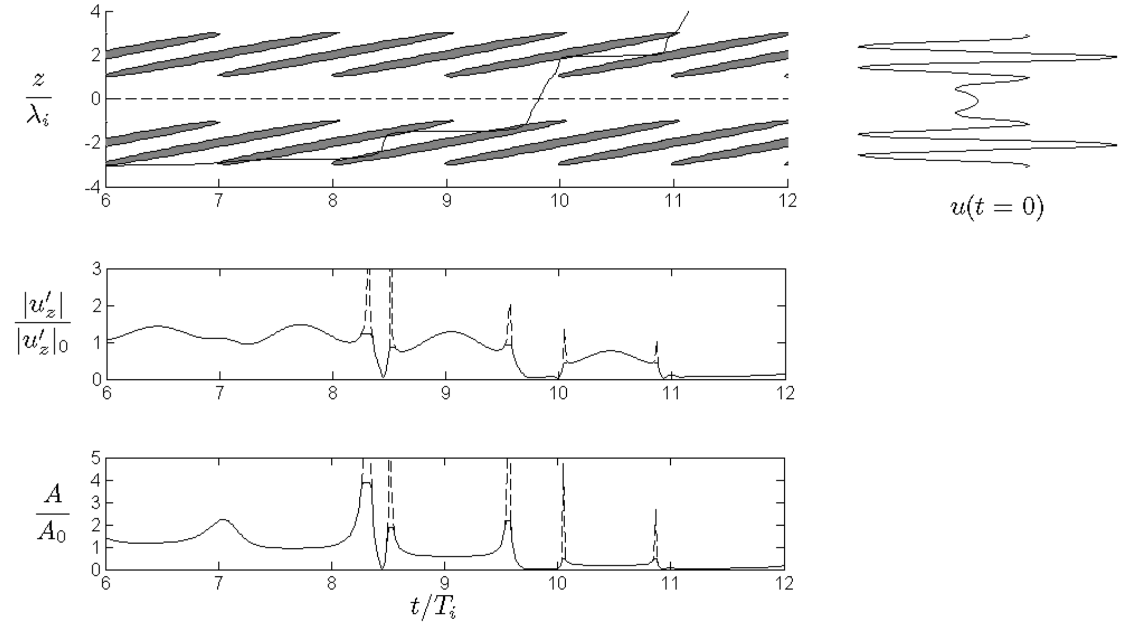

Figure II.7: A third-kind encounter followed by an upgraded first-kind encounter. All plots have the same horizontal axis, the time in inertial periods. Top: the ray path, which originates from $z = -4\lambda_i$ at $t = 0$, and the vertical profile of the inertial velocity u at $t = 0$. The lower inertial-wave packet is centerd at $z = -2\lambda_i$, and the upper one is centerd at $z = 2\lambda_i$. The two inertia waves are the same as shown in Fig. II.3 The initial wavenumber of the short waves is $m/k = -30$. Middle: the short-wave shear $|u'_z|$, with the dotted line to indicate the singular ray solution and solid line to indicate the maximum value near the caustic. Bottom: the wave-action density, with the dotted line indicating the singular ray solution and the solid line indicating the maximum value near the caustic.

ample is shown in Fig. II.7. Here the short waves propagate through two vertically separated inertial-wave packets. The lower one, below the horizontal dashed line on the plot of the ray path, is a third-kind encounter; the upper one, above the dashed line, is an upgraded encounter.

II.D Numerical Simulations

For comparison with ray theory, which is linear and which assumes, formally, a slowly varying background and slowly modulated wave packets, we now present numerical results obtained by integrating the fully nonlinear inviscid, Boussinesq equations of motion described earlier.

The full Navier-Stokes equations, defined as:

continuity

$$\frac{\partial \rho}{\partial t} + \nabla \cdot (\rho \mathbf{v}) = 0 \ , \tag{II.37}$$

and momentum

$$\rho \left(\frac{\partial \mathbf{v}}{\partial t} + \mathbf{v} \cdot \nabla \mathbf{v} \right) = -\nabla p + \rho \mathbf{g} + \mu \nabla^2 \mathbf{v} \ . \tag{II.38}$$

are changed to fit this problem. The inviscid assumption results in a loss of the shear force terms which are multiplied by ν which goes to zero. Under the Boussinesq approximation, since the deviation of the fluid density from the reference level ρ_0 is small, ρ_0 is only retained in the inertial terms on the left side of momentum equation. On the right side, however, even a small deviation in fluid density from the reference level can produce significant buoyancy effects that cannot be neglected, thus the entire density term must be retained. In their vorticity-streamfunction form, the equations are:

$$\frac{\partial^2\psi}{\partial x^2} + \frac{\partial^2\psi}{\partial z^2} = q \tag{II.39}$$

$$\frac{\partial q}{\partial t} - J(\psi, q) - \frac{\partial \sigma}{\partial x} - f\frac{\partial v}{\partial z} = 0 \tag{II.40}$$

$$\frac{\partial v}{\partial t} - J(\psi, v) + fu = 0 \tag{II.41}$$

$$\frac{\partial \sigma}{\partial t} - J(\psi, \sigma) - N^2 w = 0, \tag{II.42}$$

where q is the y-component of vorticity and $J(\psi, q)$ the Jacobian with respect to (x, z). Here the fluid velocity $\mathbf{u} = (u, v, w)$, and the stream function ψ is defined such that $u = \partial\psi/\partial z$, $w = -\partial\psi/\partial x$, and $q = \partial u/\partial z - \partial w/\partial x$. The scaled density perturbation due to the presence of internal wave motions is $\sigma = g\rho'/\rho_0$ where g is the acceleration due to gravity; the density $\rho = \rho' + \rho_0$, with $\rho_0(z)$ the mean density profile. Because of rotation, there is a nonzero v field, but all variables are assumed to be independent of y.

II.D.1 Solving the Equations

The equations are solved using a Fourier spectral collocation technique with third order, low-storage, Runge-Kutta time stepping, first introduced by Williamson [63] and further discussed by Canuto, Hussaini, Quarteroni, Zang [9]. The nth-order explicit Runge-Kutta scheme to advance a set of differential equations

$$\dot{x} = f(x) \tag{II.43}$$

over a step h is

$$x(h) = x(0) + \sum_{j=1}^{n} w_j k_j \ , \tag{II.44}$$

$$k_j = hf\left(x(0) + \sum_{i=1}^{j-1} \beta_{ji} k_i\right) \ , \tag{II.45}$$

$$\alpha_j = \sum_{i=1}^{j-1} \beta_{ij} \ , \tag{II.46}$$

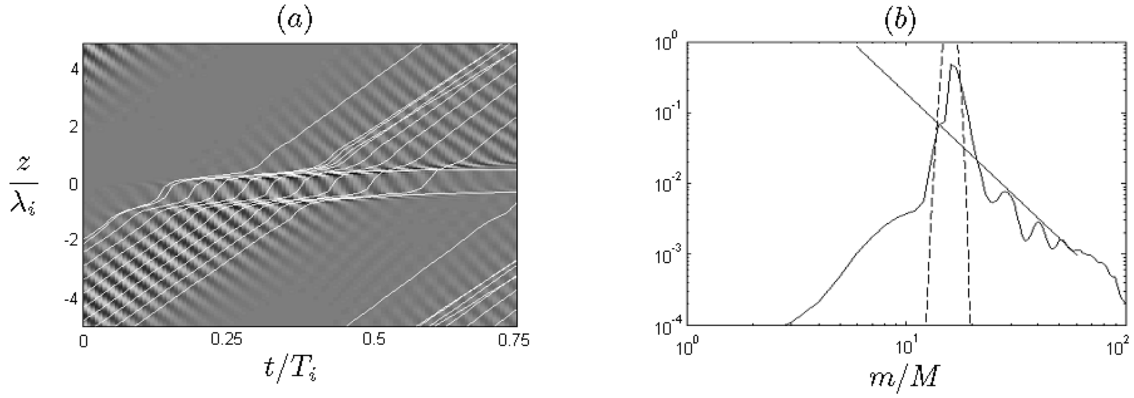

Figure II.8: An encounter of the first kind: (a) the perturbation density as a function of depth and time as computed by the spectral numerical method. Overlaid on the plot are ray paths computed as described in section II.B; (b) the time-averaged vertical wavenumber vertical displacement spectrum (solid line). The dashed line is the initial spectrum and the straight line has slope -2.9.

$$\sum_{j=1}^{n} w_j = 1 \ . \tag{II.47}$$

Where the vector x represents the N variables, which include the independent variable if f depends explicitly on it. We have chosen the following values for the coefficients: $\alpha_2 = 1/3$, $\alpha_3 = 3/4$, $\beta_{32} = 15/16$, $w_1 = 1/6$, $w_2 = 3/10$, and $w_3 = 8/15$, which correspond to Williamson [63] case 7.

II.D.2 Results

Fig. II.8a shows the perturbation density field computed from the numerical model as a function of depth and time at a fixed horizontal location. It is an example of a first kind encounter where $m/k = -3$ initially. Ray paths in the $t - z$ domain were computed for this example and are superimposed on the figure for comparison. The inertia-wave packet does not show up directly in the figure, as there is no corresponding density perturbation. These figures look much like those by Sartelet [49], Figures 1-3, where she addressed each of the three encounters in the atmosphere to test for wave-breaking. Looking closely we can see the rays do not match all that well in some of those figures. This may be attributed to the single vertical wavelength seen in each short wave envelope. Because the vertical envelope size for each of the short waves is very small, as can be seen in the work of Sartelet [50] Figure 3, the initial spectrum of the short wave is broader than the spectra presented here, so the rays calculated at a single vertical wavenumber are not a true representation of the numerical simulations, which have too small of envelopes. We are careful to have envelopes large enough to include at least four full vertical wavelengths to ensure our ray tracing calculations are as close as possible to the spectrum of short waves input into the numerical simulation. Then the previously shown calculations of wave action, shear, and vertical wavenumber along a ray would match the numerical simulations seen in Fig. II.8 and the following like figures for each encounter. Then general conclusions may be made about short-long wave interactions which include information taken from both simulations and ray theory.

After the short wave is refracted some of the rays follow the same behavior as seen in Fig. II.3, and others propagate upward. This is a result of the position of the ray and thus where and when it reaches the inertia-wave packet. The first ray which is refracted horizontally has been strongly refracted by the upper bound of the first caustic location, the last ray of the set which is refracted horizontally has been strongly refracted by the second caustic location but near the lower bound. Because of the packeting of the short wave there is a spread of initial wavenumbers of the short wave in the numerical simulation, as can be seen in Fig. II.8b. In order to see the wave propagation occurring just above the inertial wave we include a ray with slightly smaller initial vertical wavenumber, but which is still within the spectra shown, which propagates in this location. It is the second ray down and has initial wavenumber $0.94m_i$. It is important to include in this case because the locations of strong refraction here are very small, so even a small change in wavenumber will make a difference in whether or not the short wave will refract strongly.

Fig. II.8b shows the vertical-wavenumber spectrum of the vertical displacement ζ, obtained by averaging spectra over the last half of the simulation. Starting

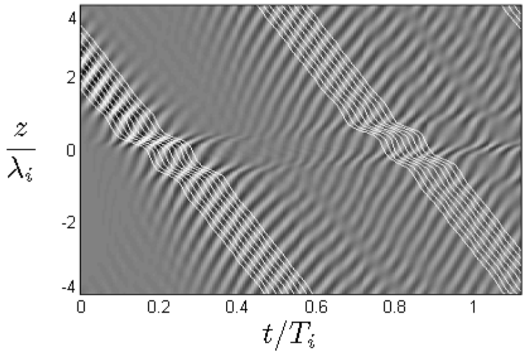

Figure II.9: Initial parameters as those in first-kind except with positive m_i and z_0. Plot details are as in Fig. II.8a.

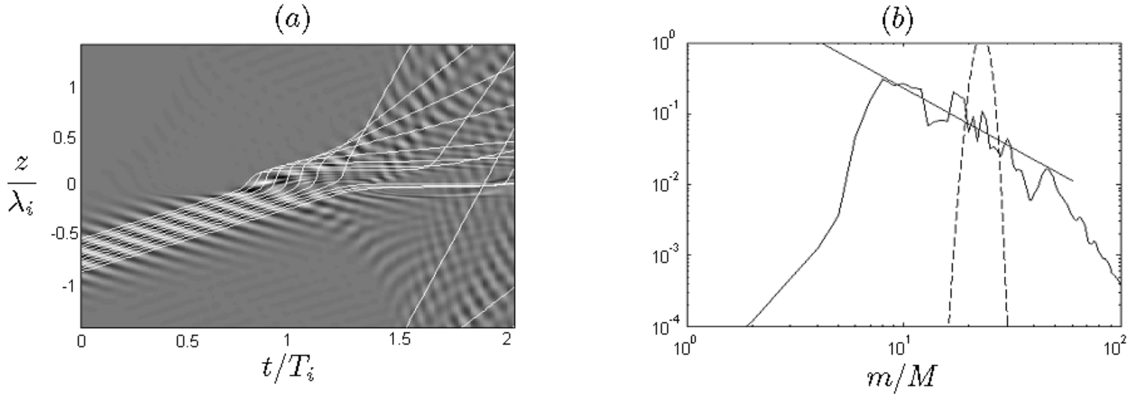

Figure II.10: An encounter of the second kind. Plot details are as in Fig. II.8, but with straight line slope in (b) -1.7.

from a single short-wave packet, which is refracted by a single inertia-wave packet, the spectrum develops a region with slope of about -2.9 within one inertia period which is in the range of the -2 to -3 high-wavenumber slopes typically measured in the ocean. But there is still a strong peak at the initial vertical wavenumber, showing that in this case many waves exit the interaction with $m_f = m_i$. This is one of the features of the first-kind encounter.

Fig. II.9 shows the perturbation density field for the same initial parameters as the first-kind encounter except with m_i positive and z_0 above the inertial wave. The short waves are being refracted in the form of non-resonant interactions. Strong refraction will not occur because $c_g = c$ will never be satisfied as these two parameters are opposite sign.

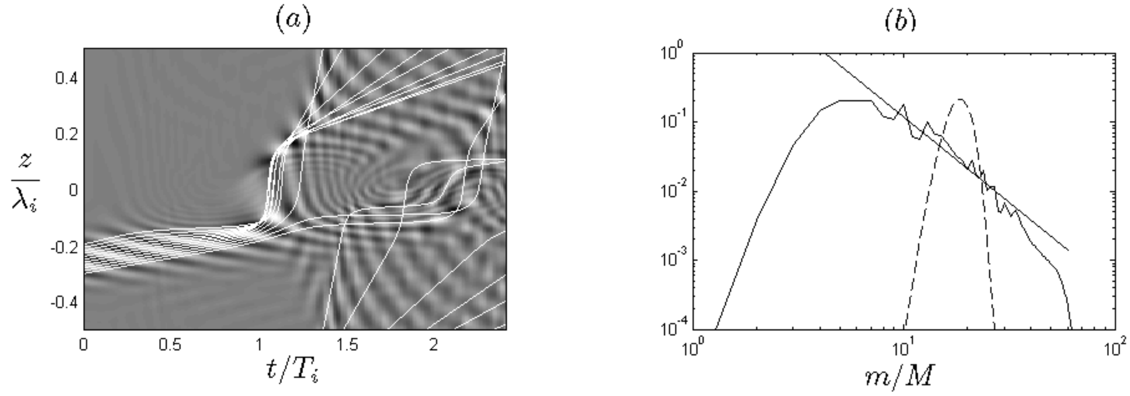

Figure II.11: An encounter of the third kind. Plot details are as in Fig. II.8, but with straight line slope in (b) -2.5.

Fig. II.10a is the perturbation density field for a second-kind encounter where for the short wave packet $m/k = -14.7$ initially. The dimensionless inertia-wave packet scale $ML = \pi/5$, or 1/10 of one inertial wavelength, is a smaller value than that used for the ray integrations of the previous section.

Once again the short-wave packet is almost immediately refracted with rays propagating both horizontally and vertically. As the rays come back into the computational domain they are refracted again, and we see many rays concentrated in the center of the domain. Multiple refractions occur in the second half of the domain, displaying the trapping of the inertial waves that occurs in second-kind encounters.

The graph of the wave energy spectrum, Fig. II.10b, shows a region with a slope of about -1.7 in the second half of the time domain. This is just below the range of typical high-wavenumber slopes within the ocean.

The perturbation density plot of Fig. II.11a is, in most of its essentials, an example of a third-kind encounter. Initially, $m/k = -35$. Once again the inertial wave has the same characteristics as described above for the second-kind encounter perturbation density plot.

The short-wave packet can be seen propagating upwards and then refracting strongly after about one inertia period, in much the same way as in the first strong refraction event seen in Fig. II.6, i.e., illustrating a $c_g = c$ interaction. Just afterward, some short-wave energy escapes rapidly from the inertia-wave packet, illustrating the permanent decrease in vertical wavenumber m that is the most striking feature of a third-kind encounter. However, because of the fanning out of the rays above the inertia-wave packet, more of a spread of m values is produced, in this case, than in the case shown in Fig. II.6. Refraction and the vertically periodic boundary conditions soon spread the short-wave energy throughout the computational domain.

It is interesting that when starting from a single short-wave packet, which is refracted repeatedly by a single inertia-wave packet, the spectrum in Fig. II.11b develops a broad region with slope of about -2.5 within two inertia periods, – in the range of the -2 to -3 high-wavenumber slopes typically measured in the ocean. For a computational domain of 100m depth, the region of -2.5 slope extends from a scale of about 12 m to about 3 m. This was also seen in work done by Broutman, Macaskill, McIntyre, and Rottman [5] and is similar to what Winters and D'Asaro [64] found in their critical layer case.

II.E Discussion

The ray and numerical simulations summarized here show that short-wave focusing is sharply concentrated around those (time-evolving) depths where $c_g = c$, and that short-wave focusing is relatively weak everywhere else. The calculations have also reminded us that, in order to understand and adequately model the role of Doppler spreading in realistic oceanic and atmospheric spectra, the usual assumptions about critical levels in steady shear need to be treated with caution since they may fail, sometimes drastically, in time-dependent shear. Similar caveats have been put forward by Eckermann [12].

What are the consequences of our conclusions for the interpretation of Henyey's ray simulations? Upgraded encounters may be useful in interpreting the results of Henyey and Pomphrey [27], who ray-trace short-wave groups through a background composed of internal waves of many frequencies and wavenumbers, combined with the amplitudes prescribed by the Garrett-Munk internal-wave model (see the work of Munk [41]). They initialize each short-wave group with high intrinsic frequency and low vertical wavenumber and terminate the ray integrations if the short-wave group refracts to 5-meter wavelength, supposing critical-layer dissipation in such cases.

It seems likely that the rapid increases in wavenumber pictured in Henyey and Pomphrey's Figure 6 are associated with the temporary satisfaction of $c_g = c$, involving the short-wave group and some near-inertial component of the background wavefield. If so we would classify them as first-kind encounters. Alternatively, the same results might represent upgraded first-kind encounters. The amplification in a first-kind encounter is strong, upgraded or not, but the likelihood of achieving instability and wave breaking is much less if the encounter is an upgraded one: the short-wave group enters into the upgraded encounter having inherited a very small amplitude from the preceding third-kind encounter. Flatté, Henyey, and Wright [14], [28] extend the Monte-Carlo ray simulations of Henyey and Pomphrey [27], but they make a key change: the initial horizontal wavelength of the short waves is lengthened to 1000m, up from 200m in Henyey and Pomphrey. It is then found, in contrast to Henyey and Pomphrey, that changes in the horizontal wavenumber of the refracting short waves become as important as changes in the vertical wavenumber in affecting the spectral transport of wave-action.

In our encounters, increasing the horizontal wavelength of the short waves while keeping the strength of the inertial shear fixed weakens the short-wave refraction in the same way as decreasing the inertial shear while keeping the horizontal wavelength of the short waves fixed, as is seen in the work of Broutman [6], Section 2. Either way, the refracting short waves experience smaller variations in vertical wavenumber. In the limit of increasing horizontal wavelength, first-kind and third-kind encounters gradually disappear, leaving only second-kind encounters which themselves become progressively weaker. In this limit, only short waves with $m \approx m_c$ before the encounter will ever satisfy $c_g = c$ during the encounter. Thus the relative importance of horizontal wavenumber variations in the studies of Flatté, Henyey, and Wright [14], [28] may be related to the relative unimportance of the $c_g = c$ condition. As the short waves in the simulations of Flatté et al. and Henyey et al. refract to shorter horizontal wavelength, we would expect $c_g = c$ to be more readily satisfied and consequently the refractive changes in vertical wavenumber to dominate the refractive changes in horizontal wavenumber. In this regard, we note that it is only after the short waves refract to the shorter horizontal wavelength of approximately $100 - 300$ m that Henyey et al. find significant refraction to short vertical wavelength, which they associate with dissipation.

A comparison of the encounters with oceanic measurements is suggested by the magnitude of m_c, the vertical wavenumber at $c_g = c$, which by (II.26) is approximately $(kMN/f)^{1/2}$. Suppose we take $N/f = 50$, and use $2\pi/100m$ for both the vertical wavenumber of the inertial wave M and the horizontal wavenumber of the short waves k. These values give (ignoring the sign) $m_c \approx 2\pi/14m$. In estimating m_c, a good indication of N and M is often obtainable from vertical profiles of density and horizontal velocity respectively, but an appropriate value to use here for k is more difficult to assess. However there is only a square root dependence on k, and there are lower and upper bounds for k beyond which the short waves propagate either too quickly or too slowly to satisfy $c_g = c$. If we take as a crude lower bound $k \geq N/u_0$ (closer to a condition for critical layers), where u_0 is the maximum speed of the inertial current, then

$$m_c \geq M\left(\frac{N}{f}\right)^{1/2}\left(\frac{N}{bu_0}\right)^{1/2} . \tag{II.48}$$

Choosing $N/f = 50$ and the minimum Richardson number $(N/Mu_0)^2$ to be $O(1)$, we find that m_c is about seven times the vertical wavenumber of the background inertial wavefield.

By these estimates m_c falls in the range of wavenumbers at which a rolloff in the slope of temperature spectra has often been observed in the ocean, [23]. Eq. (II.48) indicates that m_c increases with decreasing latitude and is only weakly dependent upon the total energy level of the internal wavefield, if that total energy is proportional to u_0^2. Both these characteristics are generally consistent with the measurements of Gregg, Winkel, and Sanford [23].

The steepening slope may thus be related to the importance of parallel-ray refraction at high vertical wavenumber. In this "Phillips limit", (II.35) constrains the wave-action density A to be approximately constant. An increase in m, or equivalently a decrease in $\hat{\omega}$ then causes a reduction in the wave-energy density $E = \hat{\omega} A$ of the refracting short waves. The lost wave-energy goes into a mean flow, which takes the form of forced and trailing inertia waves, [4]. Temperature spectra might steepen slightly more than velocity spectra because the short-wave generated inertial waves have no vertical displacement.

What are the consequences of our conclusions for Hines' theory for the high-wavenumber shape of internal-wave spectra? The context here is the upper atmosphere, where unlike the ocean, the short waves and the long waves are believed to propagate energy predominantly upwards. Hines models upward propagating internal waves only; hence $c_g = c$ interactions do not occur in his model. In such cases, our computations, and those of Eckermann [12] and Sartelet [49, 50], suggest that a steady-shear assumption is likely to lead to an overestimate, perhaps significant, of the strength of the refraction and of the rates of dissipation.

A statistical study done by Bruhwiler and Kaper [7] addresses the question of the high-wavenumber shape of internal-wave spectra as well. Using ray theory they let a set of short waves with a realistic frequency spectrum propagate through a single inertial wave. The spectrum is accounted for by the number of waves, where each wave has the same initial amplitude. They find a general trend of short waves propagating to higher frequencies, and therefore smaller vertical wavenumbers. It is interesting though that they find a flattened short wave frequency spectrum when the initial spectrum had a slope of -2. There is much more statistical work to be done, such as including changes in short wave horizontal wavenumbers and propagation through more than one inertial wave.

What are the consequences of our conclusions for the interpretation of ocean finestructure measurements? Firstly, the absence of high-wavenumber focusing may allow the short waves to refract to very large vertical wavenumber and near-inertial frequency before, or without, becoming unstable, providing a source for the near-inertial finestructure observed in the deep ocean by, for instance, Kunze, Williams, and Briscoe [34]. Their observational work shows evidence that the finest-scale near-inertial waves in the main thermocline of the deep ocean have upward-directed group velocities. Since the strongest refraction occurs for those short waves that satisfy $c_g = c$, there should be a predominance of finestructure with energy propagating in the opposite direction to that of the larger-scale near-inertial waves, which are created at the surface of the ocean by strong winds and then propagate downward into the ocean. This would typically mean that the fine-scale near-inertial waves propagate energy upwards. This is what Kunze, Williams, and Briscoe [34] have found in their data.

Secondly, we mention the observed rolloff in temperature and velocity vertical-wavenumber spectra measured in the ocean. The rolloff begins at a vertical scale of 10 m. Is this scale related to the effects of time-dependent shear? For example, do short waves of c_g less than c of the dominant background waves begin to dominate the spectrum at these scales? There is some evidence from the calculations of Henyey et al. (1986) that this is the case. If so, and if the short-wave focusing is weak at these scales, then the generation of slowly varying mean flows by the short waves becomes important, and may result in steeper spectral slopes. The mean flow takes the form of forced and trailing inertia waves [4].

III

Statistical Study of Wave-Wave Interactions

In this chapter we show and discuss the results of having a number of short waves propagating through a number of inertial waves. This will give us a statistical understanding of short wave propagation in areas where many short waves are present, which is a realistic assumption.

III.A Problem Parameters

For the statistical study, there are two main nondimensional parameters which define the problem, ϵ and μ.

$$\epsilon = \frac{1}{2ML} \tag{III.1}$$

defines the relative envelope size of the long wave: the smaller ϵ is, the closer the long wave is to an infinite wave train, and therefore solutions should be closer to adiabatic invariance theory.

The second parameter,

$$\mu_0 = u_0(k/Nc)^{1/2} \tag{III.2}$$

is a measure of the size of the short wave with respect to the long wave. This parameter defines the range of possible initial m values the short wave can have to be strongly refracted. As μ_0 increases the range of short waves which may be refracted by the inertial wave increases. μ_0 can also be thought of as a measure of the size of the contours of constant Ω in phase space. As μ_0 increases so does the size of the closed contour. But μ_0 can decrease so much that the closed contour is only a line, and the final vertical wavenumber of the short wave must be equal to the initial because no strong refraction will occur.

We do not look at some of the usual nondimensional parameters, such as the Richardson number because it is only a measure of the background shears and does not include the horizontal wavenuber of the short waves, which is important in the equation $\Omega = \hat{\omega} + uk - cm = \text{constant}$. In the cases shown throughout this chapter the nondimensional vertical wavenumber $m^* = m(c/Nk)^{1/2}$ values range from 0.2 to 2.9, and the nondimensional frequency is defined as $\omega^* = \omega(M/Nkf)^{1/2}$.

III.B Ray and Adiabatic Invariance Theory

III.B.1 Ray theory

As explained in the previous chapter, we can use ray theory to calculate approximately the behavior of short wave encounters with the inertial wave groups. To do this we assume that the inertial wave is both unaffected by the short wave interaction and has a much larger length scale than that of the short wave. Also we assume the short wave is determined by the linear dispersion relation. Then an evolution equation in characteristic form can be found for $\mathbf{k}$.

III.B.2 Adiabatic Invariance Theory

Through adiabatic invariance theory we can average the solution of ray theory over many phases, thus assuming the long-wave is an infinite wave train, and calculate two possible final short-wave vertical wavenumbers, one of which is the initial vertical wavenumber, and the other which can be found using the theory.

The ray equations are a form of the classical Hamiltonian equations. It has been shown by Cary, Escande, and Tennyson [10], and Kruskal [33] that a slowly varying Hamiltonian with one degree of freedom has an adiabatic invariant. In the context of a short wave propagating through a long wave this means the long wave must be slowly varying and have a purely horizontal velocity, which are both satisfied in this problem. The adiabatic invariant is conserved to all orders of the slowness parameter, ϵ, except when orbits in phase space cross a separatrix, which coincides with a caustic. The lowest-order adiabatic invariant is the action, which is the area enclosed by a contour of constant energy and can be calculated by integrating the canonical momentum around a phase-space trajectory. The value of the adiabatic invariant is discontinuous across the separatrix because it is defined by a different integral above, on, and below the separatrix (in phase space). The action on the separatrix is defined by taking the limit of the action as the contours of the frequency in phase space approach the limit, $\Omega \rightarrow \mu(\lambda)+2$. We are then left with the following values of action near and on the separatrix [7]:

$$\begin{aligned} Y_{a,b}(\lambda) &= \pm 2\pi(1+\mu/2) \\ &+ 4(\mu/2)^{1/2} + (1+\mu/2)\tan^{-1}[(\mu/2)^{1/2}] \ , \end{aligned} \tag{III.3}$$

$$Y_c(\lambda) = Y_a(\lambda) + Y_b(\lambda) \ , \tag{III.4}$$

where the subscripts on Y are used to indicate the relevant region of phase space. λ is the average vertical position of the test wave within the envelope of the background wave, $\lambda = Mz$. The λ-dependence in the equations arises through $\mu(\lambda)$. Location a is above the separatrix in phase space and corresponds to $\Omega > \mu + 2$ and $|m^*| < 1$, leading to the short-wave group speed being greater than the phase speed of the background wave. Location b is below the separatrix in phase space and corresponds to $\Omega < \mu + 2$ and $|m^*| > 1$, leading to the short-wave group speed being less than the phase speed of the background wave. Location c is on the separatrix, where the group speed of the short wave is equal to the phase speed of the long wave.

At the separatrix crossing the local background wavepacket amplitude is $\mu_x \equiv \mu(\lambda_x)$, and is defined implicitly by the relation:

$$-\frac{2\pi}{|m_i^*|} = -2\pi(1 + \mu_x/2) \pm \frac{1}{2} Y_c(\lambda_x) \ , \tag{III.5}$$

where the $+$ corresponds to $|m_i^*| > 1$ and the $-$ corresponds to $|m_i^*| < 1$. If the short wave escapes in a different region than it began in, then the final value of the vertical wavenumber can be calculated by relating the initial action to the final action, $Y_a - Y_b$ or vice-versa. This is the action far from the inertia-wave packet before and after the interaction. At these locations we can calculate the action in the limit of vanishing shear amplitude. Letting $\mu(\lambda) \to 0$ we find

$$Y_a = \frac{2\pi}{|m^*|} \ , \tag{III.6}$$

and

$$Y_b = -\frac{2\pi}{|m^*|} \ . \tag{III.7}$$

Then if the short wave begins below (above) the separatrix and exits above (below) the final short wave vertical wavenumber can be found using

$$1/|m_i^*| + 1/|m_f^*| = 2 + \mu_x \ . \tag{III.8}$$

Cary, Escande, and Tennyson [10] have shown that for general planar adiabatic Hamiltonian systems, given an ensemble of trapped trajectories with the same action and uniformly distributed in phase, the probability of the short wave escaping above the separatrix is $R_a \equiv Y_a'(\lambda_x)/Y_c'(\lambda_x)$, and the probability of the short wave escaping below the separatrix is $R_b \equiv Y_b'(\lambda_x)/Y_c'(\lambda_x)$, where the prime here denotes differentiation with respect to λ. In terms of already calculated parameters these probabilities are:

$$R_a(\lambda) = \frac{(\pi/2)(\mu/2)^{1/2}\tan^{-1}[(\mu/2)^{1/2}]}{21 + (\mu/2)^{1/2}\tan^{-1}[(\mu/2)^{1/2}]} \ , \tag{III.9}$$

and

$$R_b(\lambda) = 1 - R_a(\lambda) \ . \tag{III.10}$$

The wavenumber limits beyond which these wave-wave interactions cannot occur can be calculated by equating the initial adiabatic invariant far from the wave packet with the separatrix action associated with the maximum wavepacket amplitude, μ_0. Doing this both above and below the separatrix yields:

$$|M_{a,b}|^{-1} = (1 + \mu_0/2) \pm \frac{1}{4\pi} Y_c(\lambda_0) \ . \tag{III.11}$$

The importance of this parameter is that test waves with an initial vertical wavenumber $|m_i^*| > |M_b|$ or $|m_i^*| < |M_a|$ will not interact resonantly with the background wave, because their phase-space trajectories will never cross the separatrix, so $c_g = c$ will never occur.

III.C Numerical ray solutions

We have produced numerical solutions of the ray equations for a wide variety of short-wave and background inertia wave groups. For a slowly varying packet of inertial waves, these numerical ray integrations indicate that the analytical solutions for the special case of an inertia-wave train provide useful approximations. Caustics coincide approximately with $c_g = c$; and the frequency Ω varies slowly along the ray – more slowly than variations in m or $\hat{\omega}$ (see Figs. 5 and 6 of Broutman [3]).

Encounters between short waves and inertia waves, in which $c_g = c$ is satisfied at some stage during the encounter, can occur more frequently as μ_0 increases. Initially we look at these ideal interactions, where strong refraction is possible. There are some interesting phenomenon seen in the plots of Bruhwiler and Kaper [7] which we first explain.

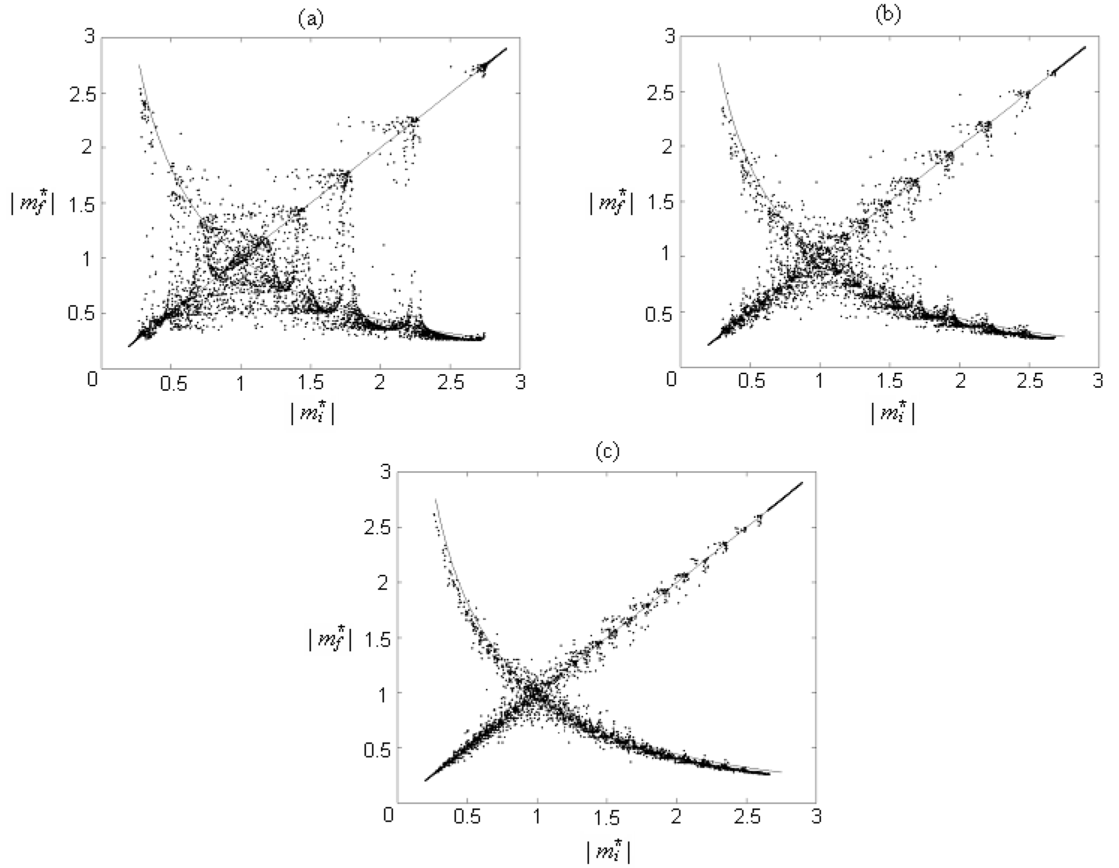

Figure III.1: As in Figure 5 in Bruhwiler and Kaper [7]. Lines are from adiabatic invariance theory, and dots from the ray tracing. Scatter plots show the results of simulating 1000 test waves for $\mu_0 = 2.0$ and (a) $\epsilon = 0.2$, (b) $\epsilon = 0.1$, and (c) $\epsilon = 0.05$.

III.C.1 Wave sets

For the initial statistical analysis, 1500 waves were traced using ray theory through an inertial wave, which resulted in Figure 5 by Bruhwiler and Kaper [7] which is analogous to Fig. III.1. The nondimensional vertical wavenumber m^* values range linearly from 0.2 to 2.9. The horizontal wavenumber is constant at $k = 2\pi/200$ and the frequency is defined by the dispersion relations. The dots represent actual short waves ray traced through an inertial wave. They are scattered around the theoretical lines created by adiabatic invariance theory. As the length of the inertial wave envelope increases, ϵ decreases and there is less variability in the results of the ray tracing. In Fig. III.1c, where $\epsilon = 0.05$ the ray tracing results lie almost exactly along the theoretical lines. Values of $\epsilon = 0.08$ are generally seen in the ocean [7].

There is a theoretical line at $m_f = m_i$ which corresponds to short waves which may not be interacting with the long wave, or fast travelling waves corresponding to first kind encounters which exit the inertial wave interaction with approximately the same final small vertical wavenumber as initial. The points created by ray tracing are scattered around this theoretical line. There are fewer dots in ther upper portion of the final vertical wavenumber domain, $m_f^* > 1$, because as we have already discovered the general trend is for short waves to propagate to lower vertical wavenumbers which correspond to a higher group speed.

The second theoretical line is curved, and makes the structure of the two lines look somewhat like a wing. This line represents short waves which interact with the inertial wave and exit the interaction with a new wavenumber. We can see that for $m_i^* < 1$ this results in an increase in short wave vertical wavenumber. We have seen this isn't very common, so again the scarce number of dots scattered about this portion of the line makes sense. The nondimensional parameter μ_0 will also affect this theoretical line. As μ_0 decreases the range of short waves which can be strongly refracted also decreases, as will be shown shortly. This results in the second theoretical line being shortened because as fewer waves are able to refract, fewer are then able to exit the interaction with a different wavenumber than they entered with.

It is of interest to note that in these plots with nondimensional vertical wavenumber as the parameter, those locations where $m^* < 1$ correspond to first kind encounters and those with values of $m^* > 1$ are third kind encounters. This can be seen by using the mid-frequency approximation where $\omega = Nk/m$, so $c_g = Nk/m^2$. Manipulating the equation for the nondimensional vertical wavenumber we have $m^* = (C^{1/2})/(c_g^{1/2})$. This relates the phase speed of the inertial wave to the group speed of the short wave. When $C \ll c_g$ then $m^* < 1$ and it is a first kind encounter.

Fig. III.2 shows the change in maximum and minimum bounds on m^* for

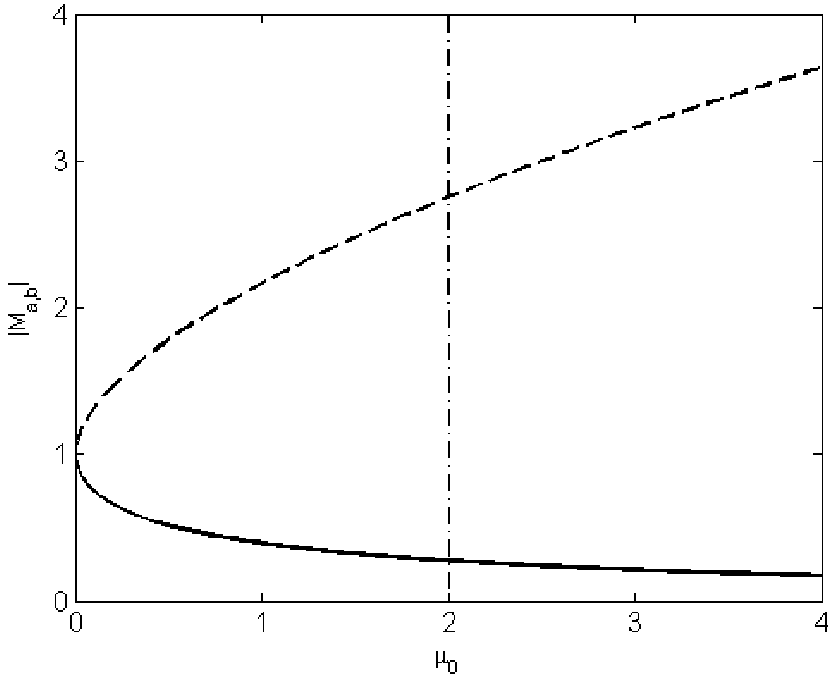

Figure III.2: Maximum (upper dashed line) and minimum (lower line) nondimensional vertical wavenumber values of the short wave for which strong refraction can occur at each μ_0 shown on the horizontal axis. Dot-dash line is located at the location $\mu_0 = 2$.

a range of μ_0 values, within which the short wave may refract strongly and exit the inertial wave with a different final vertical wavenumber. The values plotted are calculated using Eq.III.11, where M_a is the minimum possible nondimensional vertical wavenumber of the short wave which will be strongly refracted. M_b is the maximum. Therefore the larger the space between the two lines the greater the chance of a change of final vertical wavenumber as defined by adiabatic invariance theory. We can see the difference between the maximum and minimum cutoff vertical wavenumbers for the short wave decrease as μ_0 decreases. This results in a decrease in separation between minimum and maximum short wave frequencies as well. Another result of decreasing μ_0 is that the wings on Fig. III.1 will decrease until at $\mu_0 = 0$ we are left with a single line of slope 1. The smaller μ_0 becomes the smaller the range of affected short waves becomes.

Each plot in Fig. III.1 has areas with sets of values with about the same final value along the line $m_f = m_i$, and then empty spaces between the these sets where all the final values are along the theoretical line where $m_f = m_i$. We want to understand why the wave sets and other higher order phenomenon within the wave sets that can be seen in Fig. III.1 exist.

The breakdown along the curves of wave sets occurs because of the time-dependence of the background long wave. As the phases of the background wave pass through the envelope domain so do locations of strong refraction. As the short waves reach their location of strong refraction, $c_g = c$, they are caught up in that particular phase of the background. Often a few different short waves (different m values) will become trapped during a single phase because the rays are at about the same z location and have approximately the same initial m value and thus approximately the same corresponding u_c value of the background necessary for strong refraction as well. This can be seen in Fig. III.3, where 60 rays from $m_i^* = 1.6$ to 2 are equally spaced and allowed to propagate through a background wave with (a) $\epsilon = 0.2$ and (b) $\epsilon = 0.05$. Sets of rays are caught between locations of strong refraction. Each individual set of rays is made up of all the rays which were picked up

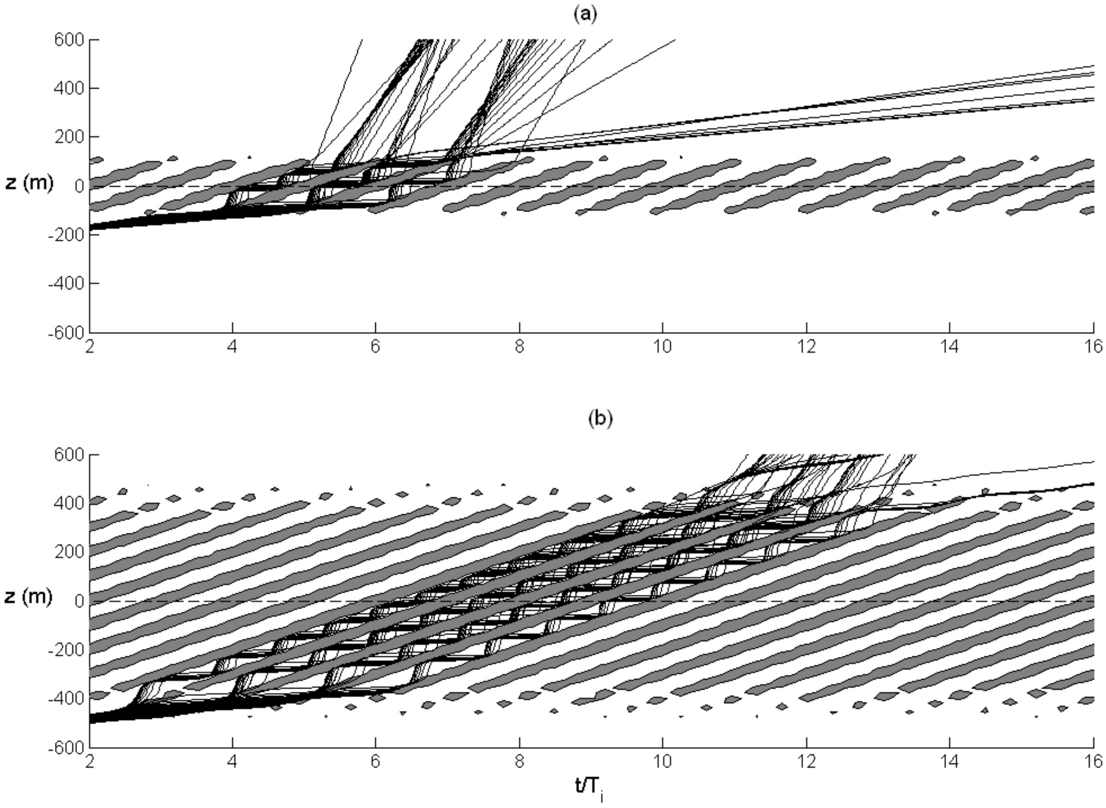

Figure III.3: Ray paths for 60 rays when (a) $\epsilon = 0.2$ and (b) $\epsilon = 0.05$. Boundaries of the shaded quasi-elliptical regions mark the locations where, at a given instant t, the strong-refraction condition $c_g = c$ can be satisfied (see text) by the same phase of the background wave. Different locations of strong refraction are present for different rays because of differing initial m values or z locations, but the locations are generally close if the initial m values are close and the rays are started about the same distance from the background. Thus sometimes a few rays will be refracted by the same passing phase of the background, and sometimes since they have not reached their point of strong refraction yet they do not get caught up in the background until a later phase comes through. Therefore we get a number of rays caught in the background as sets.

As the sets of rays exit the background phase they are more likely to exit with a lower m value because it corresponds to a higher c_g which means it can escape from the background. This can also be seen in Fig. III.3, where most of the exiting rays have an increased slope, which means $m_f < m_i$ and c_g has increased. The final refraction occuring may be slightly weaker because of the envelope and thus we get a small spread of final m values around the theoretical line. This is possible no matter what the final refraction, as we can see variability in the theoretical line where $m_f = m_i$ as well. The first few rays in the set of many rays with comparable m_i values which enter a background phase together refract the most times and exit with $m_f < m_i$, and c_g increased. The last few rays enter so late they may refract only a few times (depending on the envelope size) and exit with $m_f = m_i$. Therefore as m^* increases above 1 we have the sets seen in Fig. III.1 consisting of first an area where most of the rays end with $m_f < m_i$ (the first many rays caught in a phase of the background) then a few rays around the line $m_f = m_i$ (the last few rays caught in the phase). This process repeats itself as m_i increases and rays are caught in later phases.

For further understanding, Fig. III.4 shows background velocity profiles for three different times. The vertical dot-dash lines outline possible values of u_c necessary for strong refraction. There is a small spread of values because there is a small spread of initial m values for the short waves. At $t/T_i = 3.75$ the rays that have reached a height of about $-120m$ and have the minimum $u_c = 0.0049$ value neces-

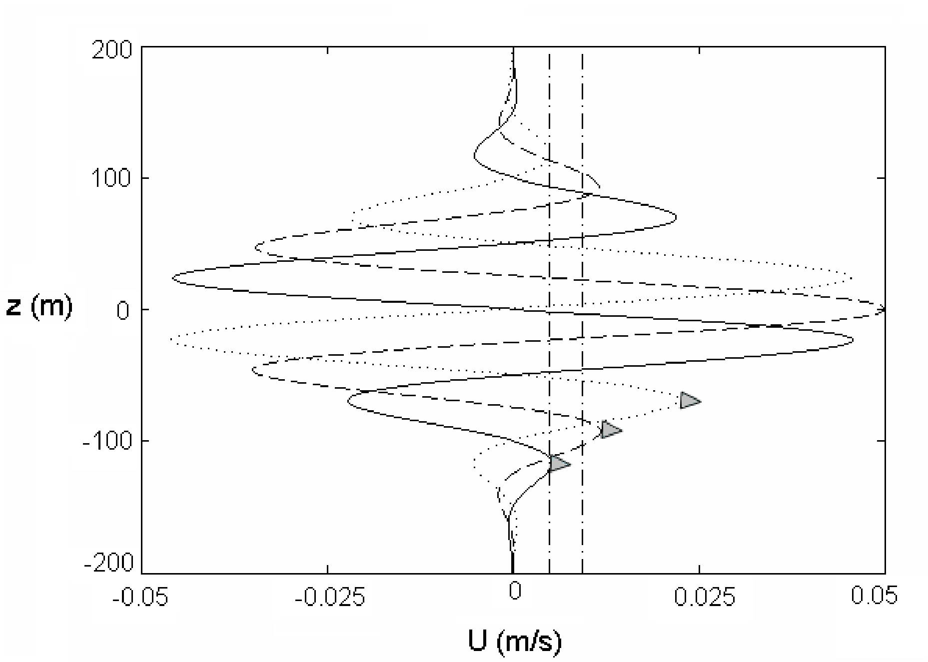

Figure III.4: Background velocity profiles for $\epsilon = 0.2$. Solid line is at $t/T_i = 3.75$, dashed line is at $t/T_i = 4$, and dotted line is at $t/T_i = 4.25$. Dot-dashed lines are minimum and maximum u_c values, 0.0049 and 0.0094 respectively. Triangles represent a single phase.

sary for strong refraction will refract. Later, at $t/T_i = 4$, rays that have propagated just further will be refracted by the dashed line phase. This will be a set of waves since a set of rays have reached this location. At $t/T_i = 4.25$ we see rays must have reached $z = -100m$ to make it into the phase we have been following (marked by a triangle at the tip of the phase). Since most will not have made it that far, they continue to propagate until the next phase comes through to pick them up.

Another way to visualize this phenomenon is shown in Fig. III.5. Here we have zoomed in on the first few strong refraction locations for the rays shown in Fig. III.3. Also shown is the value of the background wave over time for the locations $z = -97m$ (solid line) and $z = -86m$ (dashed line). The first rays reaching the background wave are those with smaller m values, because their vertical group speed is greater. The corresponding u_c values necessary for strong refraction are also smaller than those for larger m. So the first rays which reach about $z = -97m$ are being refracted, as shown by the rays which curve upward within the first two

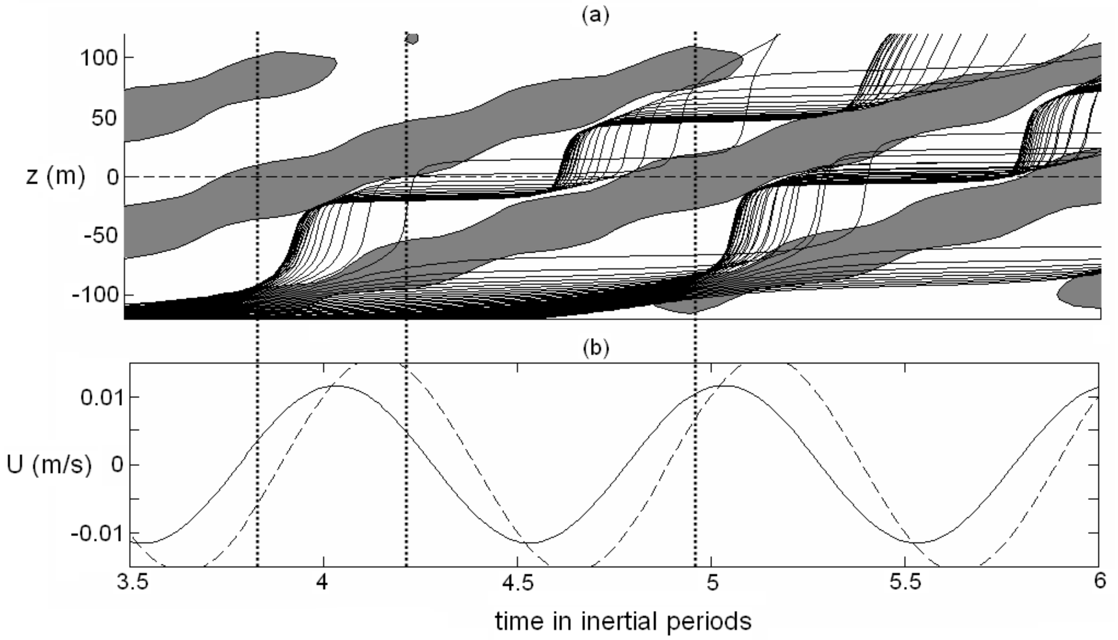

Figure III.5: (a) A closer look of Fig. III.3a. (b) The corresponding background velocity values at $z = -97m$ (solid line) and $z = -86m$ (dashed line). The first two heavy dotted lines correspond to the first initial and final locations of strong refraction, the third is the next location of strong refraction.

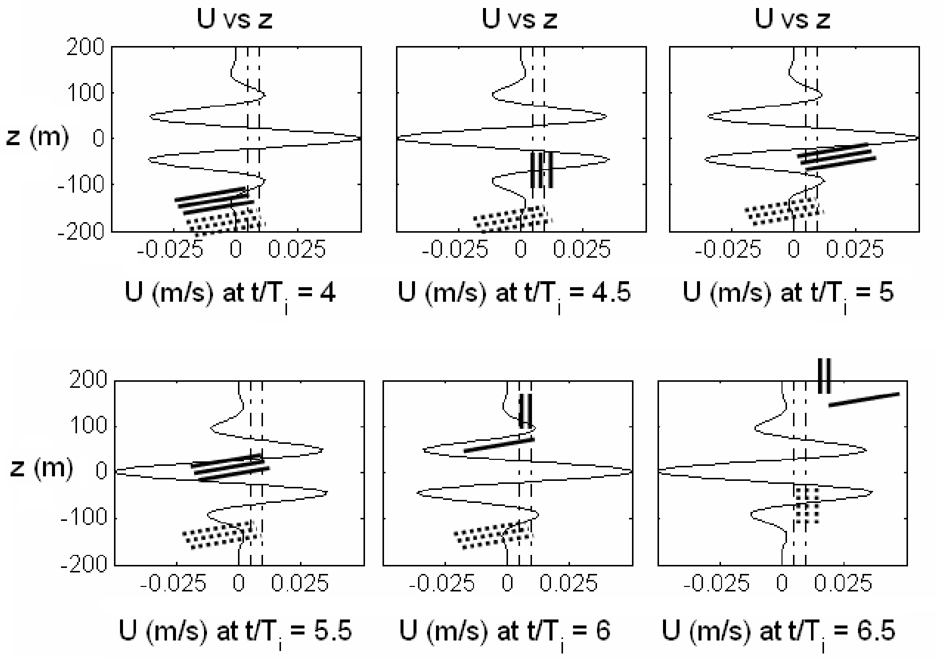

Figure III.6: Snapshot of background velocity U at different times throughout a short-long wave interaction. The vertical dot-dash lines outline the u_c values for which strong refraction will occur. For each snapshot we follow cartoon rays, depicted as solid and dotted lines, propagating upward through the long wave. The solid lines correspond to the first rays which are strongly refracted and the dotted lines correspond to the next set of rays which are strongly refracted.

heavy dotted lines, which outline the location of strong refraction. The slower short waves, with larger m, get to $z = -97m$ too late and are not refracted yet by the long background wave. Instead they continue to propagate to about $z = -86m$ where the new background U value is plotted as a dashed line. The heavy dotted line corresponds to the first location of refraction for these short waves.

The cartoon shown in Fig. III.6 depicts an idea of what is going on as sets of rays are strongly refracted by the background wave. The background wave velocity is shown by the solid sine wave with an envelope, and the vertical dot-dash lines outline possible values of u_c necessary for strong refraction. Again there is a small spread of values because there is a small spread of initial m values for the short waves. The solid lines depict the first few rays, which will be refracted first, and the heavy dotted lines represent the second set of rays, which are not strongly refracted until a later phase of the background wave. Notice these rays all have a shallow propagation angle, corresponding to a slow initial vertical group speed of the short wave, so $c_g < c$ in this example. We see the first set of rays reaches a location of strong refraction within the background wave almost immediately, and is strongly refracted, resulting in an increase in group speed and a slope in $z-t$ space which is almost vertical (shown as vertical in the cartoon for easy viewing) at the next time snapshot. We see the rays with slower group speed (not obvious in the cartoon slope of the rays, but they are lower in z so they must have been going more slowly) have not yet reached a point of strong refraction and are passed over by this first phase, so they continue to propagate slowly throughout most of these time snapshots. In the next time snapshot, $t/T_i = 5$, the rays are all slowly propagating and have not yet reached another location of strong refraction, or rather such a location has not yet reached them, as $c_g < c$. Finally, at $t/T_i = 5.5$, two of the rays from the first set have reached another location of strong refraction and in the next plot they have become vertical and it is obvious they will be escaping the background wave as there are no other possible locations of strong refraction. These represent the majority of the rays in the set, which exit the long wave with an increase in vertical group speed and a decrease in m, $m_f < m_i$. The single ray of the set which was left behind will also exit the background wave without another refraction, but just barely. This wave represents the few rays in the set which may exit the long wave with approximately the same vertical group speed as it began with, $m_f = m_i$. At $t/T_i = 6$ the other set of short waves has finally reached a point of strong refraction and these waves begin their trip through the background wave as the others are exiting.

Once we understand why these wave sets occur then we ask why the number of wave sets increase and the spacing between them decrease as ϵ decreases (getting closer to theory). As the long wave approaches an infinite wave train a couple things are happening. First there are fewer rays being caught up with each background

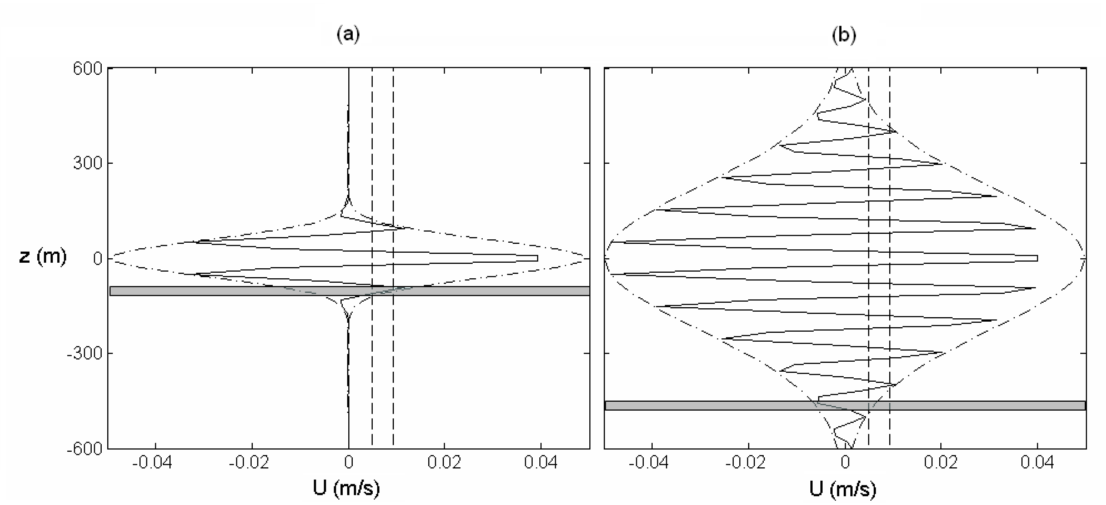

Figure III.7: Initial background velocity profiles (solid lines) for (a) $\epsilon = 0.2$ and (b) $\epsilon = 0.05$. Dot-dash line is envelope, dashed lines correspond to minimum and maximum u_c values for the range of initial rays used, and highlighted area is equal on both graphs.

phase, and therefore fewer rays in each phase set, but more sets of rays being caught in other phases. This can be seen in the Fig. III.3, where the upper plot is representative of a background wave with $M = 2\pi/100$ and $\epsilon = 0.2$ and the lower plot has $\epsilon = 0.05$ (closer to infinite wave train). Both plots have 60 rays equally spaced in m, but Fig. III.3a has less rays being trapped in each phase. Fig. III.7 shows the corresponding initial background velocity and envelope for the cases. From the rectangular highlighted boxes superimposed on the figure, which are both the same size and begin at the first location of possible strong refraction when taking the envelope into account, we can see that a larger range of possible U values is available when the envelope is smaller ($\epsilon = 0.2$). This is because when the envelope size is increased the angle of the envelope as it opens and closes decreases (is much more shallow). With the smaller envelope, as soon as it opens there is a wide range of u values available for the background wave to take on, and many rays are strongly refracted. So in the same amount of z space the shorter envelope has more possible u_c values for strong refraction. Thus in the figures we see more rays being caught in each phase of the background when it has a smaller envelope.

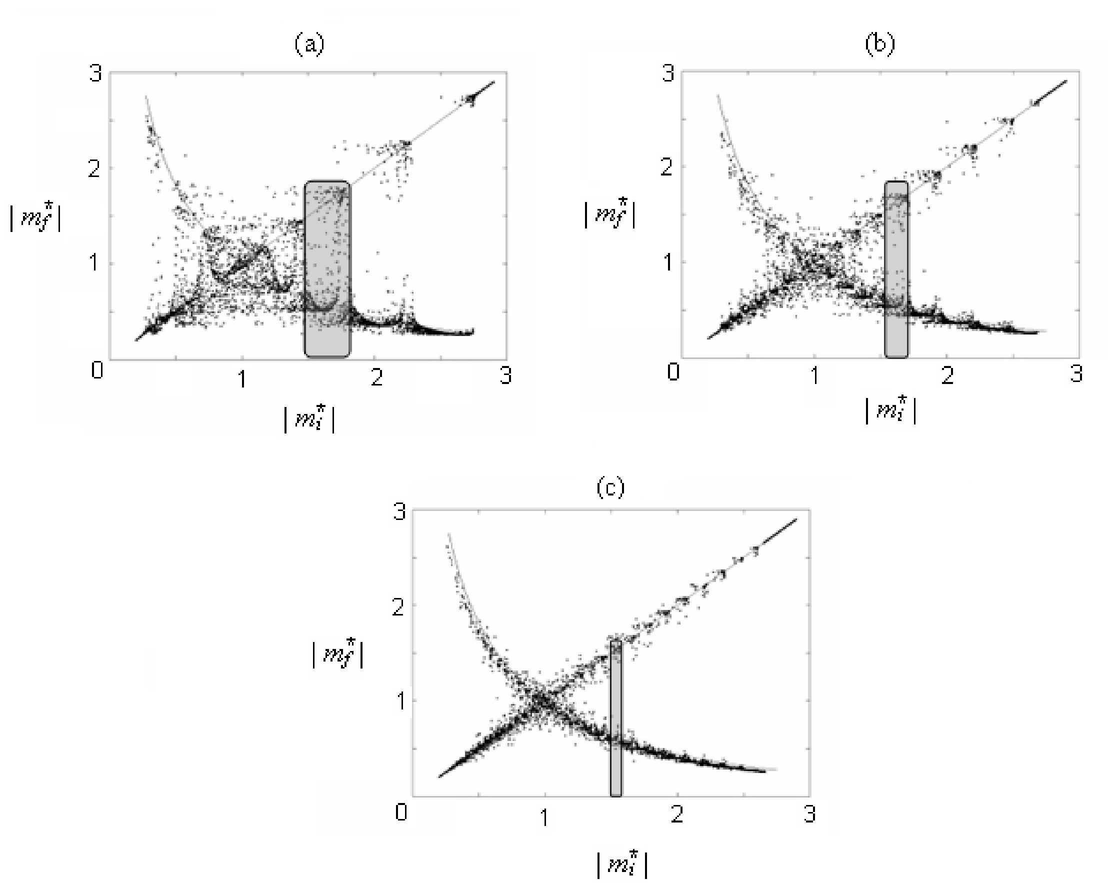

Figure III.8: As in Fig. III.1. Scatter plots showing the results of simulating test waves for $\mu_0 = 2.0$ and (a) $\epsilon = 0.2$, (b) $\epsilon = 0.1$, and (c) $\epsilon = 0.05$, where an example set of waves is circled in each graph.

As the length of the envelope increases the rays being refracted are more confined, just the few which have reached this small region of u_c values necessary to strongly refract will be caught in the particular phase of the background wave. Thus we see smaller sets of waves which are closer in m-space when the background wave has a larger envelope size (decrease in ϵ).

There is a strong relationship between the space between sets and the value of ϵ. If we are to call the size of a set the distance from the beginning of the set on the m_f theory line and ending on the $m_f = m_i$ line, as is shown in Fig. III.8, we can see as ϵ decreases so does the set size. It seems to be a linear relationship. If we account for the terms of most importance - or to first order - as mentioned before the slope of the opening envelope matters. Calculating $d(envelope)/dz$ we find it is proportional to $1/L$ for a given $z = XL$ value, where XL is the distance from the center of the envelope. As the slope of the inertial wave envelope increases, the size of the sets increases since more waves' u_c value is attained more quickly. Another important factor we have not yet discussed is the vertical wavelength of the inertial wave. As the vertical wavelength increases we have a longer period of time when the inertial wave satisfies u_c for the short waves (it is not rushing to start another wavelength if there are merely say 2 in the packet instead of 10). Since λ_Z, the vertical wavelength of the inertial wave, is proportional to $1/M$, as $1/M$ increases, so do the set sizes. We can also think of this in terms of the phase speed, f/M. If it is increased, even if the envelope has a very shallow slope, more u_c values can be attained in a shorter amount of time while the short waves are all near the same z location since the waves move quickly through it. So we conclude: set size $\propto 1/L * 1/M \propto \epsilon$. ϵ values ranging from 0.025 to 0.3 were tested and it was found that the average set size $= 2\epsilon$.

In the ray tracing plots we can see that the farther the rays propagate the more spread they become because of their different c_g values. The waves with greater m_i values have slower group speeds and therefore encounter the background wave at a later time. The slower the wave-group, the shallower the slope and the longer the short wave lingers near the same z location as the phase of the background passes through, so more rays can get caught in a single phase so the set (set at $m_f > m_i$ and set at $m_f = m_i$) is larger.

There is less variability in the wave sets themselves as ϵ decreases. This is because as the long wave becomes closer to an infinite wave-train it gets closer to the theoretical line. With many refractions occurring we are getting closer to an infinite wave-train. Also, as the waves exit there again will be less variability (as there was when the waves entered the background envelope).

It is interesting to note that even if we are to initialize the short waves at random depths, the results are the same as we have seen here, with wave sets

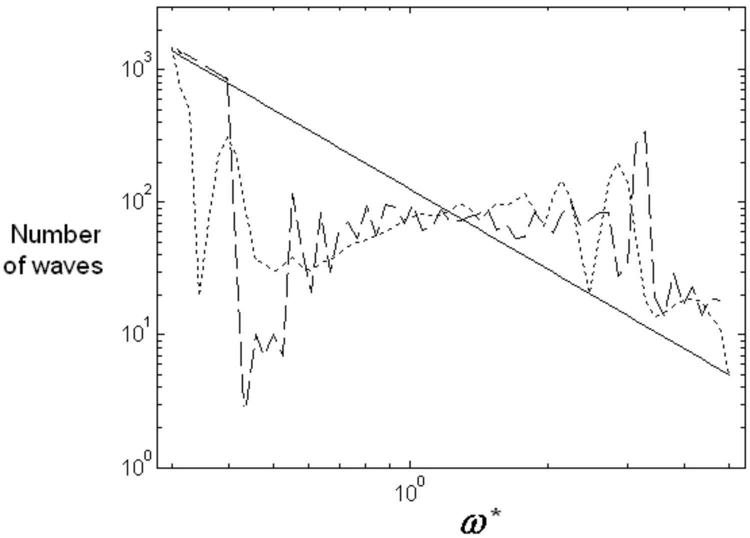

Figure III.9: As in Figure 8 in [7]. Frequency spectrum from a number of short waves, energy accounted for by number of waves in each frequency bin. $\epsilon = 0.1$, $\mu_0 = 2$, and $k = 2\pi/200$. Initial frequency spectrum (solid line), final spectrum calculated through ray tracing (dashed line), final spectrum calculated through adiabatic invariance theory (dotted line).

occurring along the theoretical lines. Because the relationship between the slope of the advancing ray and the slope of the region of strong refraction is the same, the short waves will still have a preferred final vertical wavenumber. Thus we see the wave set phenomenon.

III.C.2 Short wave horizontal wavenumber changes

We have reproduced Figure 8 from the work of Bruhwiler and Kaper [7], and it is shown in Fig. III.9, which is the short wave frequency spectrum after a set of short waves has propagated through a single inertial wave where the initial short wave vertical wavenumber is $k = 2\pi/200$, $\epsilon = 0.1$ and $\mu_0 = 2$. Here the energy is accounted for by the number of rays in the simulation: each short wave has the same amount of energy initially, so more waves at a particular frequency results in more energy at that frequency. In Fig. III.9 we see a frequency spectrum with an initial slope of -2 has a final slope of approximately 0 after the short waves interact with a single inertial wave. We note the ray tracing and adiabatic invariance theory results

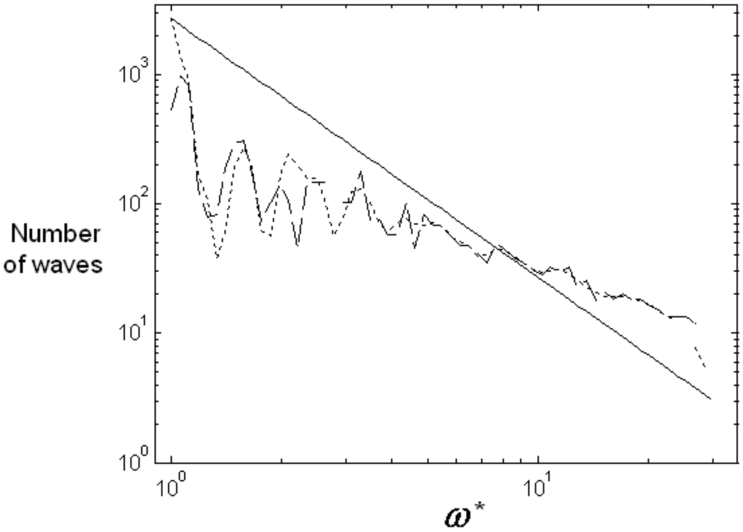

Figure III.10: Number of waves with initial (solid line) and final frequency spectrum calculated through ray tracing (dashed line), final frequency spectrum calculated through adiabatic invariance theory (dotted line), where $\epsilon = 0.1$, $\mu_0 = 0.3$, and $k = 2\pi/5000$.

match quite well. This result shows a general trend of short waves propagating to higher frequencies (shorter vertical wavenumber), as was seen in the third-kind encounter.

Extending these results to include other horizontal wavenumbers results in a decrease in the range of initial vertical wavenumbers in order to keep the short wave frequency between the inertial frequency and the buoyancy frequency while still keeping the short wave vertical wavelength smaller than that of the inertial wave. Results like those in Fig. III.9 but for $k = 2\pi/5000$ and $\mu_0 = 0.3$ are shown in Fig. III.10. As k decreases, so does μ_0, and a decrease in μ_0 results in a decrease in effective strong refraction because fewer waves can be refracted as was seen in Fig. III.2. We can see the decrease in the vertical wavenumber extent of the flattened area, which corresponds to a group of waves with are refracting to different final vertical wavenumbers, due to the decreased value of μ_0. But we can use a larger value for u_0, up to about 30cm/s as that is about the greatest velocity of inertial waves observed, to counter-act the decrease in k and keep $\mu_0 = u_0(k/Nc)^{1/2}$ realistic

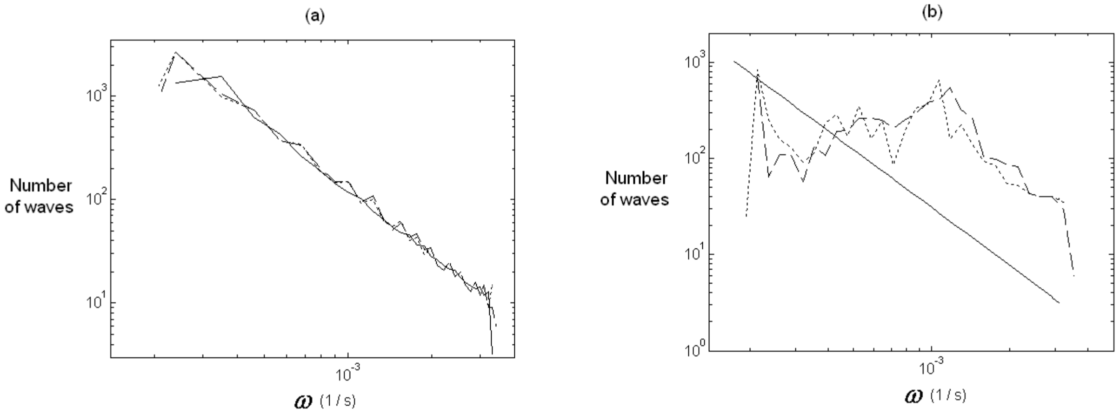

Figure III.11: As in Fig. III.9 but for initial values of k having a -2 log slope, ranging from (a) $k = 2\pi/10000$ to $k = 2\pi/200$, and (b) $k = 2\pi/500$ to $2\pi/200$. $\epsilon = 0.1$, $u_0 = 4$cm/s, and $0.2 < \mu_0 < 2.0$. 30 bins are used to find the energy at each ω value. Solid line is initial spectrum, dashed line is final spectrum calculated from ray theory, dotted line is final spectrum calculated from adiabatic invariance theory.

($\mu_0 > 1$). Since the same range of ω values for Fig. III.10 were used in Fig. III.9 but k is larger, the result is a decrease in overall m values, in this case $m^* < 0.75$. With this k decrease we see that only a few short waves are affected by the long wave, resulting in new vertical wavenumber values, highlighting the importance of the short-long wave relationship in strong refraction occurrences.

To extend the calculations we include a -2 slope for both the frequency and horizontal wavenumber of the short wave and let them vary from $k = 2\pi/10000$ to $k = 2\pi/200$ and $\omega = 2f$ to $\omega = N/2$. The results are shown in Fig. III.11a. For these figures $\epsilon = 0.1$, $u_0 = 4$cm/s, and $0.2 < \mu_0 < 2.0$. Fig. III.11 shows the strong relationship between the initial and final ω values. Because of the -2 slope imposed on the horizontal wavenumber spectrum there are a large number of waves with values of k too small to allow for strong refraction by the long wave. These waves dominate the final results so the short wave frequency spectra does not significantly change throughout the interaction. In decreasing the value of k, and therefore accounting for longer horizontal wavelengths of the short waves, we introduce a spectrum of waves that does not change much after propagating through an inertial wave. We also introduce short-wave vertical wavenumbers smaller than that of the inertial-wave, resulting in short waves that are not small scale. If we then also choose to decrease the vertical wavenumber of the long wave, we decrease μ_0 even more and are left with a final spectrum almost exactly equal to the initial.

Fig. III.11b, has a smaller range of short-wave horizontal wavenumbers than Fig. III.11a in order to have more short waves within the region of strong refraction, yet still have the -2 slope in the k parameter. The horizontal wavenumber range is $k = 2\pi/500$ to $2\pi/200$, with $\epsilon = 0.1$, and $\mu_0 = 2$. We use both ray tracing and adiabatic invariance theory to calculate the short wave frequency spectrum, and the two methods match quite well. These plots also agree with the general theory of Bruhwiler and Kaper [7] in that the frequency spectrum is flattened. But the range of horizontal wavenumber values for the short wave is very narrow.

Hence there are a limited number of k values available to use and still stay within the bounds of a realistic and small short wave vertical wavelength. The assumptions to watch because they are affected by changing k include keeping $\mu_0 > 1$ and having the short wave be a smaller spatial scale than the long wave. When k is altered it is important to make sure the short-waves are still small scale. As k decreases, m also decreases if ω is constant (the bounds of ω are approximatly constant to satisfy the mid-frequency approximation), so at $k = 2M\omega/N$, then $m = 2M$, and if k gets any smaller the vertical spatial scale separation will not be enough to call the short waves small scale. Although decreasing M will increase the possible spread of k values to keep $m > 2M$ (assuming this will keep the waves spatially separated), it will even further constrict the range of m values subject to strong refraction by decreasing μ_0 more.

III.C.3 Propagation through many inertial waves

Another step from what Bruhwiler and Kaper have done is to test what happens when a set of short waves propagates through a set of inertial waves. Using adiabatic invariance theory as Bruhwiler and Kaper [7] do, we calculate a set of m_f, and ω_f values after starting with the same set as in Fig. III.9. Then this final

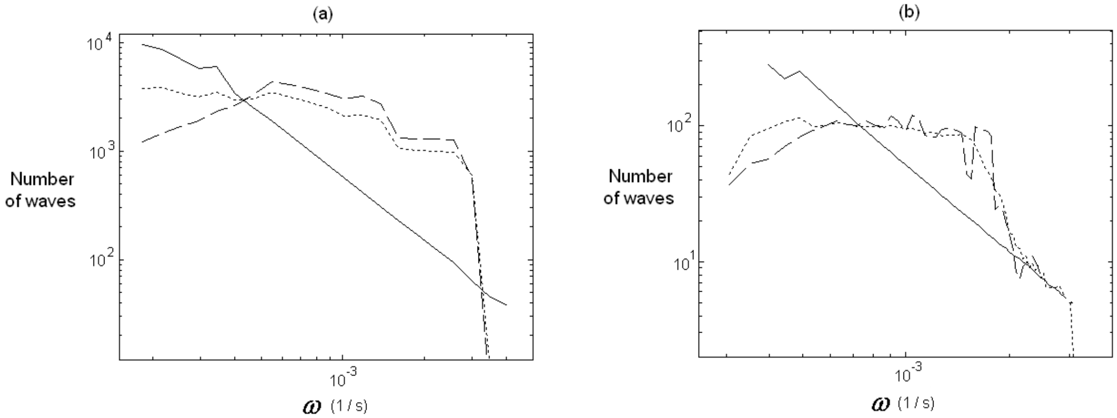

Figure III.12: Initial and final short wave frequencies (values binned): (a) using adiabatic invariance theory, (b) using ray tracing. Note the difference in scales, as more waves were used in the theoretical case because of the fast calculation time. The solid line shows the initial frequencies, $k = 2\pi/500$ to $k = 2\pi/200$, the dashed line is after first long wave interaction, and the dotted line represents the final frequencies after the short wave has propagated through eight inertial waves.

set of rays become the initial set of rays and their propagation through the inertial wave is calculated again for these new values. Fig. III.12a shows what the final spectrum will look like after the first interaction (dashed line), and then after eight interactions (dotted line) when using adiabatic invariance theory. We can see the spectrum seems to flatten out more after many interactions with the inertial wave. The spectrum actually fluctuates back and forth between a flat spectrum and a spectrum with a slightly negative slope, yet after many interactions the spectrum is almost totally flat.

The resulting frequency spectra, after a set of short waves propagates through eight identical inertial waves in ray tracing, yeild the same type of results as adiabatic invariance theory does. Fig. III.12b shows that when using ray tracing, after more interactions with the inertial wave, the variability around the horizontal line (a perfectly flat spectrum) decreases, and the spectrum of all the rays is eventually horizontal.

The consequences of such results is that the general trend is for low frequency waves to propagate to higher frequencies. This is consistent with the previous results of Bruhwiler and Kaper [7] and Vanderhoff, Nomura, Rottman, and Macaskill [61] showing the idea of propagation of short waves to smaller vertical wavenumbers. Although this final spectrum is not necessarily more likely to break, since for that we would want short waves at larger vertical wavenumbers which would result in smaller vertical wavelengths leading to breaking, there is a possibility of breaking within the short-long wave interaction, specifically at the caustics. If the waves do not break, though, we would expect this flat frequency spectrum to emerge when a broad ensemble of short waves with a -2 slope (close to ocean values) propagates through inertial waves. Since this does not seem to be the result in the ocean, as the -2 slope seems to be constant throughout the ocean, other interactions or three-dimensional effects are probably present. One such mechanism occurring which is not calculated here is short wave breaking, which may be occuring within this region of strong refraction.

III.D Discussion

The statistical results of this chapter show that if a set of short waves with realistic ocean frequency spectra propagate upward through a downward propagating inertial wave, the resulting frequency spectrum is no longer that of a realistic ocean. The frequency spectrum is instead almost horizontal. There is a question of what type of spectrum can be input to have the output resemble that of the ocean, and if that input spectrum can also resemble the observed ocean spectrum. The general trend of short-waves of low frequencies propagating to higher frequencies corresponds to short waves exiting with smaller vertical wavenumbers. These results match previous numerical and ray tracing studies. What is not taken into account in these statistics is the decrease in amplitude of these waves. In this study we simply count the number of rays at each frequency, but do not take into account their energy, which is also important. The work here has been purely two-dimensional and the -2 slope in the vertical wavenumber has not been accounted for either.

Because a horizontal frequency spectrum is not seen in the ocean, something must be occurring to keep the short waves from attaining this flattened spectrum. It is possible that the short waves are not interacting with the inertial wave and therefore there would be no change in the frequency spectrum. However, the next chapter will show the relationship between inertial waves and short wave activity suggests there is definitely some sort of interaction between the two. Another conclusion may be that some of those short waves which can interact are breaking and dissipating their energy, and others which are interacting are transferring their energy down to those scales which had originally broken. This idea will be discussed further in the next chapter when breaking locations are calculated.

IV

Observational Analysis

This chapter will cover the observational setup, location, instruments used to collect data, and an analysis of that data. Then I will compare the results of the observations to results from both numerical simulations and ray tracing simulations. I will make conclusions about possible mechanisms affecting the flow at these locations within the ocean, and what signature may be seen in the ocean which can be a clue to the observer that strong refraction in the form studied here is occurring within the ocean and atmosphere.

The data being analyzed here was collected as a part of the Hawaiian Ocean-Mixing Experiment, HOME. The purpose of HOME was to test the theory that mixing does not occur uniformly over the entire ocean, which has been supported by recent measurements which show an increase in mixing over topography [46]. As mentioned previously, turbulent mixing is an important process in the ocean, which redistributes nutrients, heat, pollutants, momentum, and other ocean properties. Both observations and computational modeling of flow over the Hawaiian Ridge were used as a part of HOME to better understand turbulent mixing over topography. The Hawaiian Ridge is an ideal location because of its steep slopes and regular energy input from tides flowing perpendicular to the ridge. Also, there had previously been observational equipment moored near the Hawaiian Ridge collecting data which could be analyzed and used to support the present HOME data.

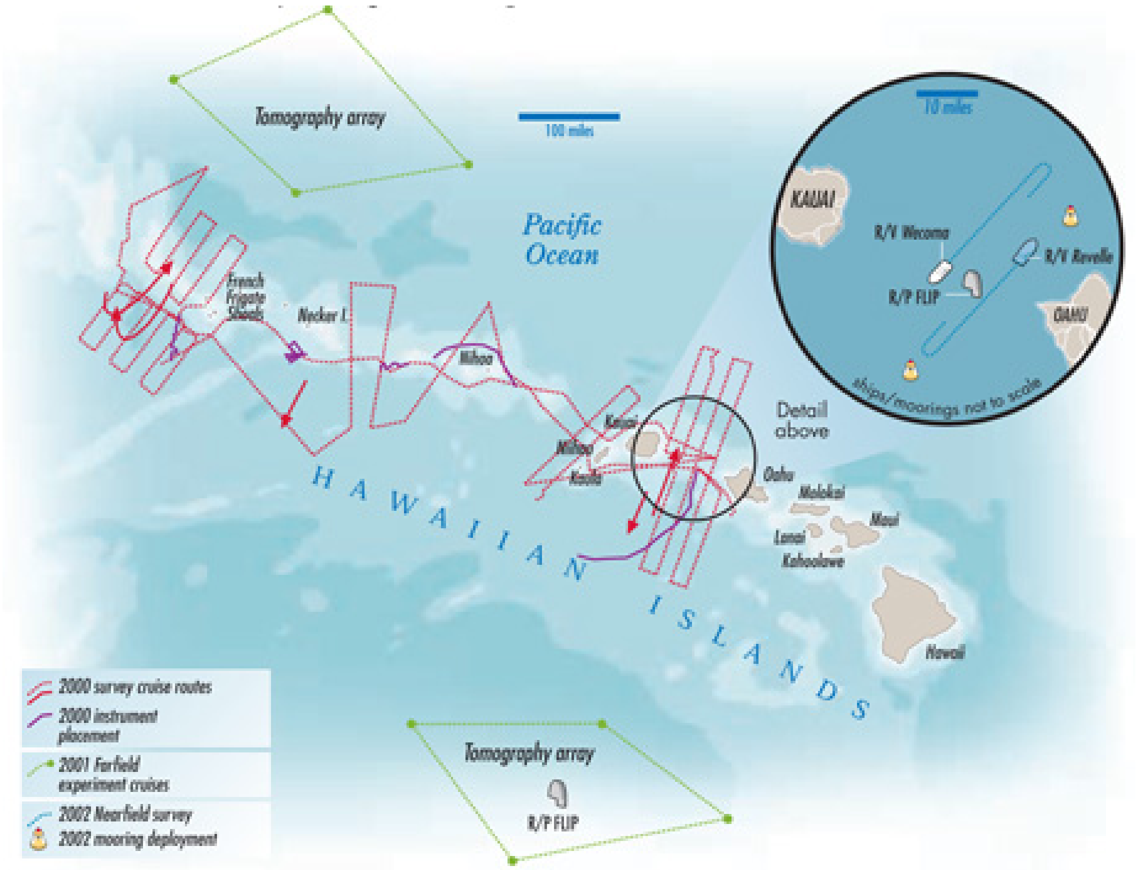

Figure IV.1: Observational cruise paths from 2000 to 2002 along and around the Hawaiian Ridge. Figure provided by HOME researchers on chowder.ucsd.edu/home/index.html

The modelling aspect of HOME consisted of model-based data assimilations, based on historical data, satellite altimetry data, plus data collected during HOME, which resulted in general ideas for enhanced tidal mixing over topography which could be applied globally.

The observational aspect of HOME included a number of ocean cruises to collect data all along the ridge, in a specific location above Kaena Ridge, and far from the ridge. First a survey of the Hawaiian Ridge was done in order to quantify geographic variability of turbulent mixing around the Hawaiian Ridge, as well as to find an ideal location for the more specific Nearfield region, which would be further studied as a part of HOME. This was accomplished over five cruises. These are drawn in red in Fig. IV.1. After this survey the Eastern Kauai Channel, between

Oahu and Kauai, was chosen to be further studied, which includes Kaena Ridge.

Then observations were taken in the Farfield region, where models had approximated the propagation of energy away from the Eastern Kauai Channel out into the open ocean. The cruise path was then chosen and is drawn in green in Fig. IV.1. There was also one stationary location where data was collected on the FLoating Instrument Platform, whose location is also shown in Fig. IV.1. The data collected here was necessary to show how much energy escaped the Hawaiian Ridge and made it into the open ocean without breaking and causing turbulent dissipation. In general the energy lost from the barotropic tide is equal to the baroclinic tide radiative energy plus the local dissipation. The first two pieces of this equation are quantified by the farfield observations.

The last piece of this equation, local dissipation, is found by the final observational component in the Nearfield, which consisted of cruises shown by blue lines in Fig. IV.1. Again these cruises included both moving ships collecting data and a stationary setup just above Kaena Ridge. This stationary location will be described in more detail in the next section, as it is the location at which the data being analyzed here was taken. The purpose of the Nearfield is to observe the mixing processes above the ridge in enough detail to understand the dynamics behind the mixing.

Through satellite altimetry, HOME researchers Zaron and Egbert [68] found that 26 gigawatts of tidal energy is dissipated in the region of the Hawaiian Ridge. This shows a definite increase in tidal mixing at this location near topography. Using two vertical profilers and a towed body over six cruises along Kauai Channel, it was shown that there is strong internal wave generation and energy there, with high turbulence near the bottom and over the ridge crest. This turbulence decayed further from the topography, and by 60 km away the mixing values had fallen to the open-ocean values. These general results support the theory that mixing is enhanced over topography in the ocean.

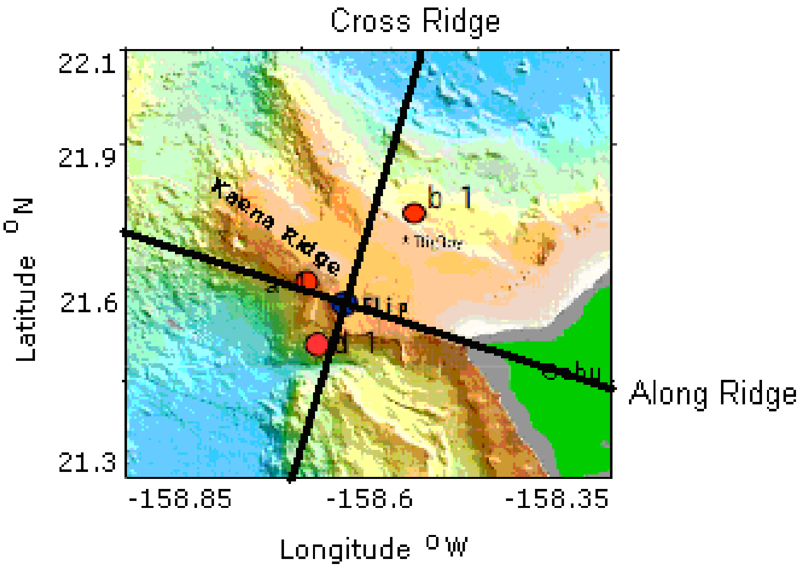

Figure IV.2: Location of FLIP during August 2002 HOME Nearfield data collection. The blue circle represents the location of FLIP, the red circles are the locations of the moorings. The solid lines denote cross-ridge and along-ridge directions.

IV.A Observational Setup

During the Nearfield study in August, 2002, the FLoating Instrument Platform, FLIP, was moored as shown in Fig. IV.2, just east of the crest of Kaena Ridge, Hawaii, a submerged western extension of the Hawaiian island of Oahu. It extends west-north-west from Oahu for about 60 km, half of the distance to Kauaii. At the location of FLIP the ridge is approximately in a North-South orientation. The crest depth is about 1100 meters deep, with surrounding areas at 5 km depth, and located at 21.7° North, 158.6° West. Instruments deployed on FLIP, including an eight-beam, coded-pulse Doppler sonar measuring velocity and two current-temperature-density profilers, CTD's, collected data in a range from 80 meters to 820 meters depth. The two CTD's are a Seabird SBE 9 CTD's, which measure current, temperature, and pressure, from which salinity, depth, and density can be calculated. There is also a micro-conductivity cell mounted on the instrument which can resolve temperature-salinity fluctuations down to 10 cm scales. The instruments

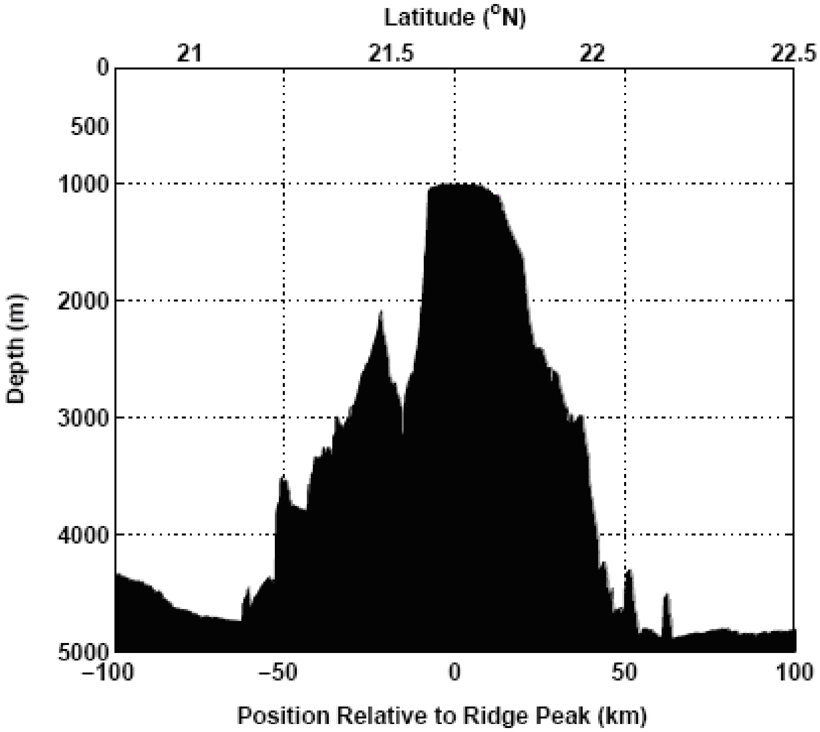

Figure IV.3: View of Kaena Ridge from the east looking west.

are pulled up and down every four minutes using two computer controlled winches which run at 3.5 m/s, resulting in 1.1 meter vertical resolution. The sonar can profile a 600 – 800 meter vertical range, with 3 meter vertical resolution, one minute temporal resolution and 1 cm/s precision. A current meter was also deployed at 800 m, from which we could read the velocity of the current from a rotor, and the direction of the current from the tail of the instrument, which acts to align the instrument such that the body will face into the oncoming current.

Slopes as steep as 1:4 define the north-north-east and south-south-west sides of the ridge. Fig. IV.3 is a view from the south of the ridge, looking north toward the ridge. Fig. IV.4 is a view of the ridge from east-south-east looking west-north-west, or along the ridge (along-ridge). Fig. IV.5 is a view of the ridge from south-south-west looking north-north-east, or across the ridge (cross-ridge).

The ridge is oriented roughly normal to local semi-diurnal barotropic tidal flow. The S_2 (12 hour semidiurnal solar) tidal current has amplitude 2.8 cm/s East

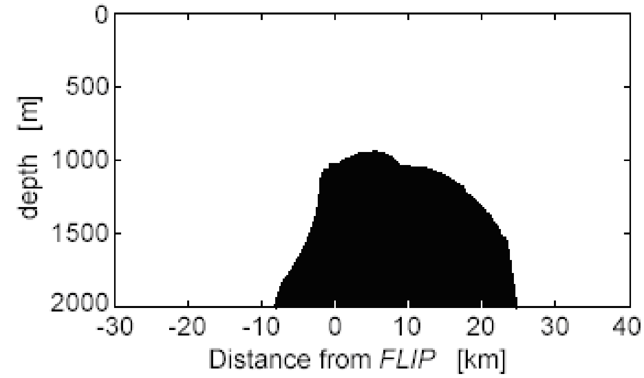

Figure IV.4: View of Kaena Ridge from east-south-east looking west-north-west.

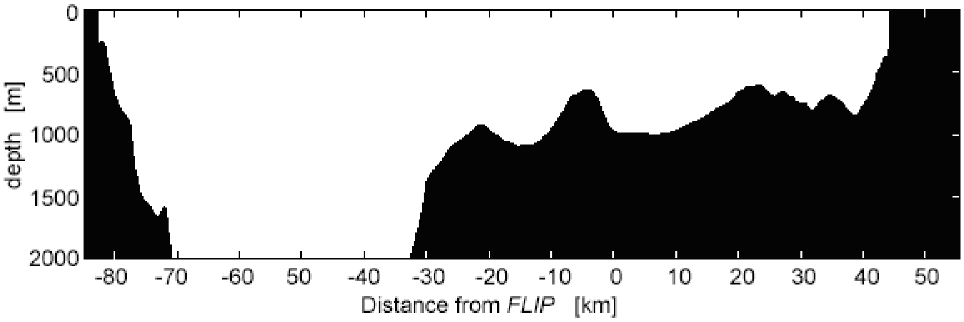

Figure IV.5: View of Kaena Ridge from south-south-west looking north-north-east.

and 5.2 cm/s North. The K_1 (24 hour diurnal solar) tidal current has amplitude 3.2 cm/s East and 4.6 cm/s North. The M_2 (semidiurnal lunar - 12 hour 25 minute) tidal current has amplitude 6.4 cm/s East and 11.7 cm/s North, and is the dominant tide. It has a pronounced fortnightly cycle. The currents do not reach the deep sensors on the moorings, and are apparently generated above the ridge crest.

Above 500 meters depth energy and momentum fluxes are upward and southward (1dyne/cm^2 during spring tide). Below 500 meters depth the fluxes are upward and northward. Above the ridge crest, power spectra of horizontal velocity and vertical displacement have pronounced D2 (diurnal - 12 hour) peak, but there is little evidence of it in the shear field, as we will see later. The cruise covered two neap and two spring tides. The first neap tide was covered from year day 257 (September 14, 2002) to year day 261 (September 18, 2002). The first spring tide was from year day 262 to year day 269.

As a preliminary analysis of the dynamics of the flow around Kaena Ridge we have calculated the background mean currents, which are shown in Fig. IV.6. Also shown are the mean currents over the week of most interest to us (which will be explained later). The U velocity is zonal, where positive is eastward current. The V velocity is meridional where positive is northward current.

The buoyancy frequency was calculated using the conductivity and temperature readings of the CTD's, from which a profile of density can be obtained. Using this data the buoyancy frequency along the water column is calculated as $N = \sqrt{g/\rho \Delta\rho/\Delta z}$. These values are averaged over year day 258 to year day 290, and then fit using a cubic spline to smooth the curve. The final result is plotted in Fig. IV.7, which shows the decrease in buoyancy frequency with decreasing ocean depth. We can also see the location of the thermocline at about 100 m, where the buoyancy frequency increases rapidly to about 10 cycles per hour.

Cross-ridge velocity and shear calculated over one week, from year day 260 to year day 267 are shown in Fig. IV.8. Peaks can be seen in the observations in both the velocity and shear spectra at the inertial, diurnal, and semidiurnal frequencies.

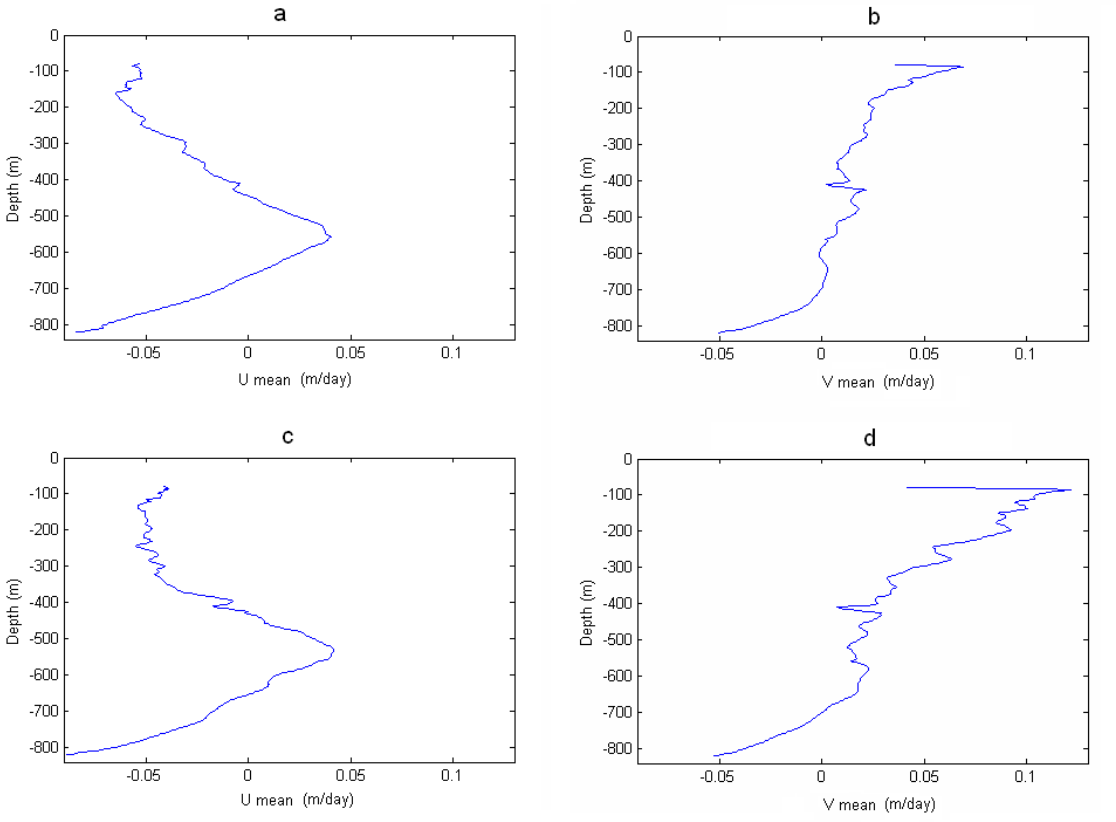

Figure IV.6: Average current over time. (a) Average zonal velocity (where positive is eastward) over depth for year days 258 to 291. (b) Average meridional velocity (where positive is northward) over depth for year days 258 to 291. (c) Average zonal velocity over depth for year days 260 to 267. (d) Average meridional velocity over depth for year days 260 to 267.

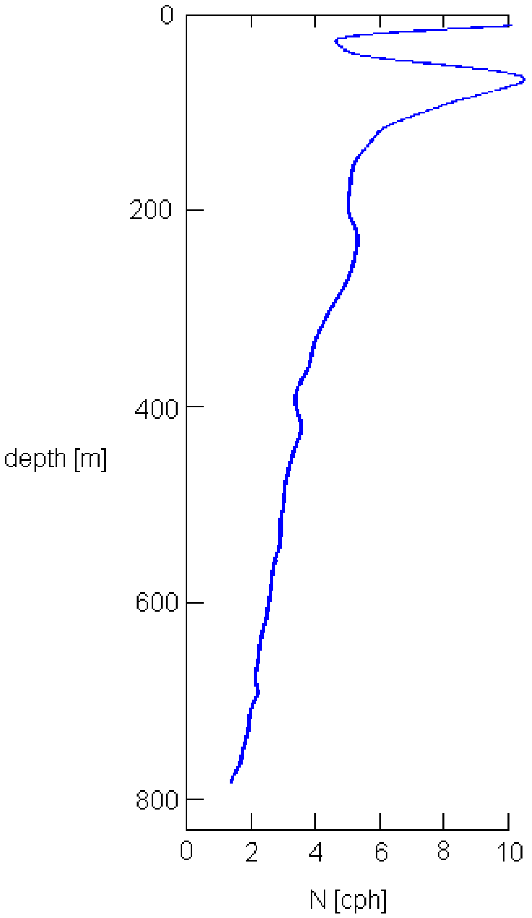

Figure IV.7: Average buoyancy frequency over 32 days, fit with a cubic spline.

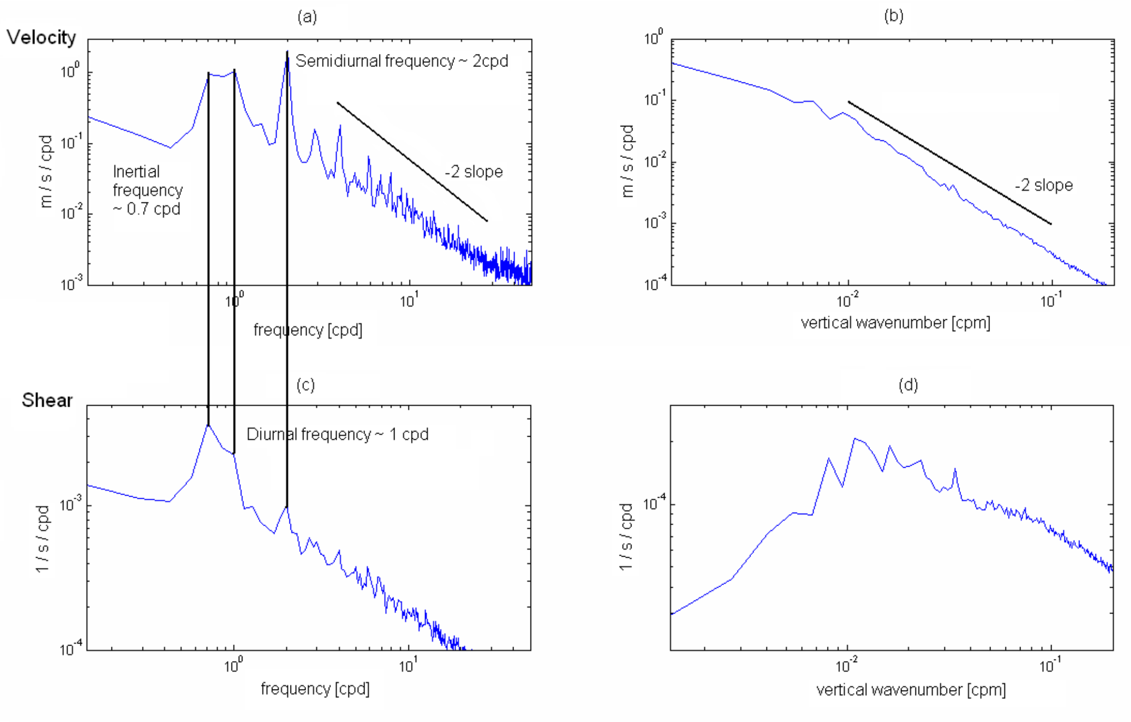

Figure IV.8: Observations from sonar data over Kaena Ridge for one week (year day 260 to year day 267) over all depths (100 meters to 800 meters). Inertial, diurnal, and semidiurnal frequencies are labelled. A line with slope of -2 is superimposed on both the frequency and vertical wavenumber graphs for the velocity. (a) Frequency spectrum for cross-ridge velocity averaged over all depths (371 data points). (b) Vertical wavenumber spectrum for cross-ridge velocity averaged over one week (2520 data points). (c) Frequency spectrum for cross-ridge shear, U_z, averaged over all depths (371 data points). (d) Vertical wavenumber spectrum for cross-ridge shear averaged over one week (2520 data points).

Notice that in the shear spectrum the inertial and diurnal frequencies have the highest peaks, yet in the velocity spectrum it is the semidiurnal frequency which has the highest peak. From this we see the near-inertial shears we are assuming in previous calculations are being seen in the ocean. The large signature of the semidiurnal frequency in the velocity spectrum occurs because of the tidal flow over the ridge. There is energy in the velocity at the semidiurnal frequency, but the strongest shears are at the inertial and diurnal frequencies. Also, an approximately -2 high vertical wavenumber slope and high frequency slope can be seen in Fig. IV.8a and b.

IV.B Mathematics and Analysis

The observations are made up of a time series of current, temperature and pressure data points from approximately 100 meters deep to 800 meters in the ocean, taken over a few weeks. The calculations necessary to do a preliminary analysis of the observational data include calcualting power spectral density, cross spectra, cospectra, coherences, and phases. The following is an overview of how this is accomplished.

The eight-beam, coded-pulse Doppler sonar system measures velocity. Horizontal velocity is calculated by taking into account the slanted orientation of the beams. The shear is then obtained by differencing this horizontal velocity in depth. The CTD's measure conductivity, temperature, and pressure at each meter depth every 4 minutes, from about 50 meters to 950 meters depth. From the conductivity and temperature readings, profiles of density and velocity can be obtained.

The vertical velocity can be defined as the change in isopycnal displacement over time, as follows:

$$\hat{w} = \frac{\partial \zeta}{\partial t} \ . \tag{IV.1}$$

The rate of strain is defined as the change in the vertical velocity over depth, as follows:

$$\text{strainrate} = \frac{\partial \mathrm{w}}{\partial \mathrm{z}} = \frac{\partial^2 \zeta}{\partial \mathrm{z} \partial \mathrm{t}} \ . \tag{IV.2}$$

For calculating spectral estimates, we define the number of data points as n, and the record length in time as $2T$. Frequency steps are defined as $\sigma_n = 2\pi n/2T$, where the lowest resolvable Fourier frequency is π/T. Then the separation in frequency between Fourier estimates is: $\Delta\sigma = 2\pi/2T$ in radians / record length in time.

We can plot the energy spectral density in two dimensions, which gives us an idea of how the energy in the ocean is distributed among short and long scale waves (in terms of vertical wavenumbers) and fast and slow waves (in terms of frequencies). Consider data $B(x,t)$ where $-X < x < X$ defines the spatial bounds and $-T < t < T$ defines the time bounds on the data. Then B is given uniquely by

$$B(x,t) = \sum_{n=-\infty}^{\infty} \sum_{m=-\infty}^{\infty} = B_{nm} e^{i(\alpha_m x + \sigma_n t)} \tag{IV.3}$$

where $\alpha_m = 2\pi m/2X$ and $\sigma_n = 2\pi n/2T$. The associated spectral estimate is

$$\hat{E}(\alpha_m, \sigma_n) = \frac{|B_{nm}|^2}{\Delta\alpha\Delta\sigma} \ . \tag{IV.4}$$

To compare data, we define a pair of time series data as $A(t, \overline{x}_1) \equiv A_1(t)$ and $A(t, \overline{x}_2) \equiv A_2(t)$, where the energy spectrum of the two time series are $\hat{E}_1(\sigma) \equiv 2\left|A_1(\sigma)\right|^2/\Delta\sigma$ and $\hat{E}_2(\sigma) \equiv 2\left|A_2(\sigma)\right|^2/\Delta\sigma$, when $\sigma > 0$. Where $\overline{x}_1$ and $\overline{x}_2$ are two different properties defined at specific spatial locations over time. For example property 1 may be the horizontal velocity of the high frequency waves, and property 2 may be the low frequency shear, both of which are calculated from the same time series, but represent different data. To find relationships between the two we start by selecting a trial value of the number of degrees of freedom, N. Then we break the records up into $N/2$ segments. Fourier transform each individual segment and create the products, $A_1^*(\sigma)A_2(\sigma)$, where the * represents a complex conjugate. Then we average these together to get an N degree of freedom estimate of the cross spectrum,

$$\hat{C}_{12}(\sigma) = \frac{\frac{2}{N}\sum_{n=1}^{N/2} A_1^{n*}(\sigma)A_2^{n}(\sigma)}{\Delta\sigma} \tag{IV.5}$$

(we divide by $\Delta\sigma$ to get the cross spectral density).

The real part of the cross spectrum is the Co-spectrum ($\widehat{Co}_{12}(\sigma)$), and the imaginary part is the Quadrature spectrum ($\hat{Q}_{12}(\sigma)$). Now we can define the phase of the cross spectrum as the angle of the cross spectrum:

$$\hat{\Phi}_{12}(\sigma) = tan^{-1}\frac{\hat{Q}_{12}(\sigma)}{\widehat{Co}_{12}(\sigma)} \ . \tag{IV.6}$$

This is a measure of whether or not the two data series are in phase or out of phase.

The coherence of the cross spectrum is defined as:

$$\widehat{Coh}_{12}(\sigma) = \frac{\left|\hat{C}_{12}(\sigma)\right|}{\left[\hat{E}_1(\sigma)\hat{E}_2(\sigma)\right]^{1/2}} \ . \tag{IV.7}$$

This is the normalized absolute value of the cross spectrum. The maximum value of the coherence is 1, which corresponds to two completely coherent data series. This would occur if the two series were exactly the same, or if one of the data series was completely dependent on the other. A coherence of 0 means the two data series have nothing to do with each other, and are not even randomly coherent. A greater coherence shows a stronger relationship exists between the two data series.

The observational data collected on FLIP over the Kaena Ridge supports the idea of strong refraction by time-dependent shears as a mechanism for transferring internal gravity waves to smaller, breaking scales. Correlations between the near-inertial shear and high-frequency (1 to 5 hour period) wave strain rate have been detected. This can be seen in Fig. IV.9 which is an image of the shear normalized by the buoyancy frequency over one week down to approximately 800 meters depth and the strain rate squared, which represents high frequency wave activity. The sideways ”v” shapes in the shear are characteristic of upward and downward propagating near-inertial waves, as can be seen by their period of approximately 24 to 30 hours, relating to a frequency of about 1 to 1.3f. The dominant vertical vertical

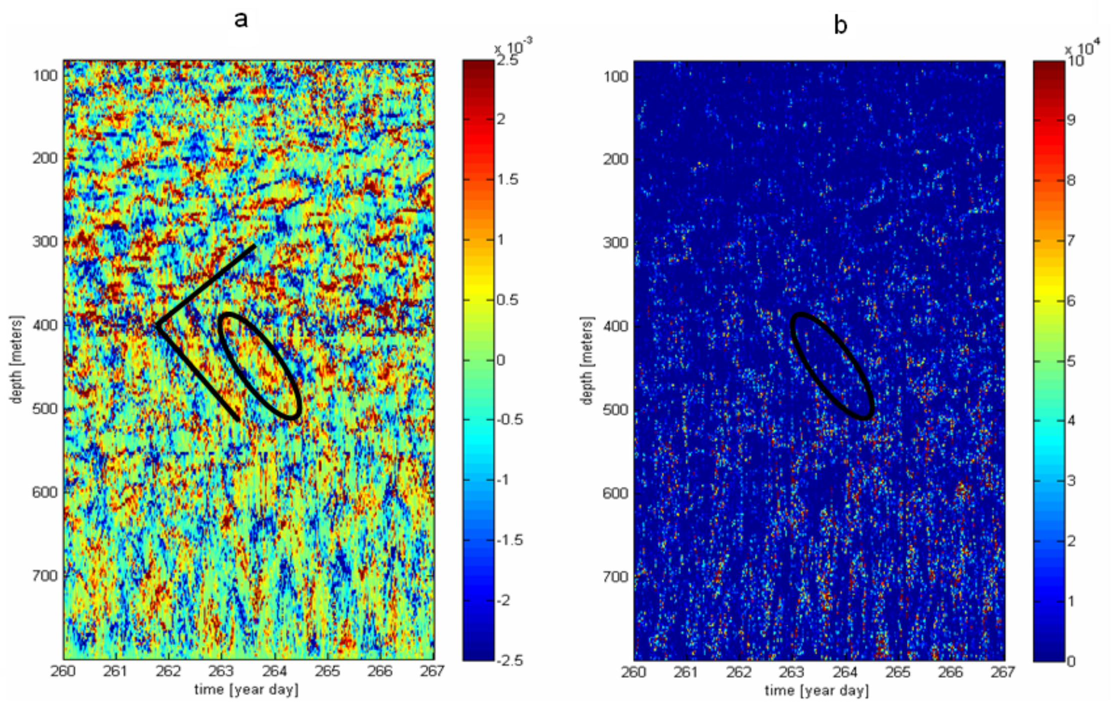

Figure IV.9: (a) Cross-ridge shear normalized by buoyancy frequency (dimensionless) calculated from the sonar data. (b) Strain rate squared [1/days^2] calculated from the sonar data.

wavelength is 75 meters. For the upward propagating near-inertial wave locations, between about 400 meters and 500 meters depth, have positive shear regions which correspond directly to a modulation in the squared strain rate field, which is a measure of the high frequency wave activity. In the presence of large positive shear due to near-inertial waves, high frequency waves are suppressed, which may be explained by a strong interaction occurring between the two waves, such as refraction.

To confirm this we test the frequency spectrum for each field, the shear and the strain rate squared, to see if there is any indication of this interesting behavior. Fig. IV.10 shows the 52-degree of freedom estimate, used for averaging, of the frequency spectra for these two fields over the week of interest, year day 260 to 267, and the specific depths of interest, 425 to 475 meters. We can see a peak in both the shear and strain rate squared spectra around a near-inertial frequency of 0.9 cycles per day.

The trend is even easier to see when we use a basic band pass filter to see only low frequencies in the shear field, between 0.6 cpd to 1.4 cpd, and smooth the squared strain rate field with a 30 meter, 6 hour finite impulse response filter. The results of this smoothing are shown in Fig. IV.11, where the locations of increased shear corresponding to locations of decreased squared strain rate are again circled. The strong squared strain rate at lower depths corresponds to increased short wave activity due to nearby bathymetry exciting short waves and affecting the flow parameters at depths below about 500 meters. Above this these features do not exist or affect the flow.

A numerical simulation, done as described in Chapter II, of a situation similar to that observed is shown in Fig. IV.12. Here two short waves, one of which interacts as an encounter of the second kind and the other as a third kind, are input and followed as they interact with a wave of frequency 1 cpd. Fig. IV.12a shows the shear, which is directed at an opposite angle to the observations because in the observations the inertial waves have an upward group speed and downward phase speed, but the net propagation of the crests is upward because the group speed

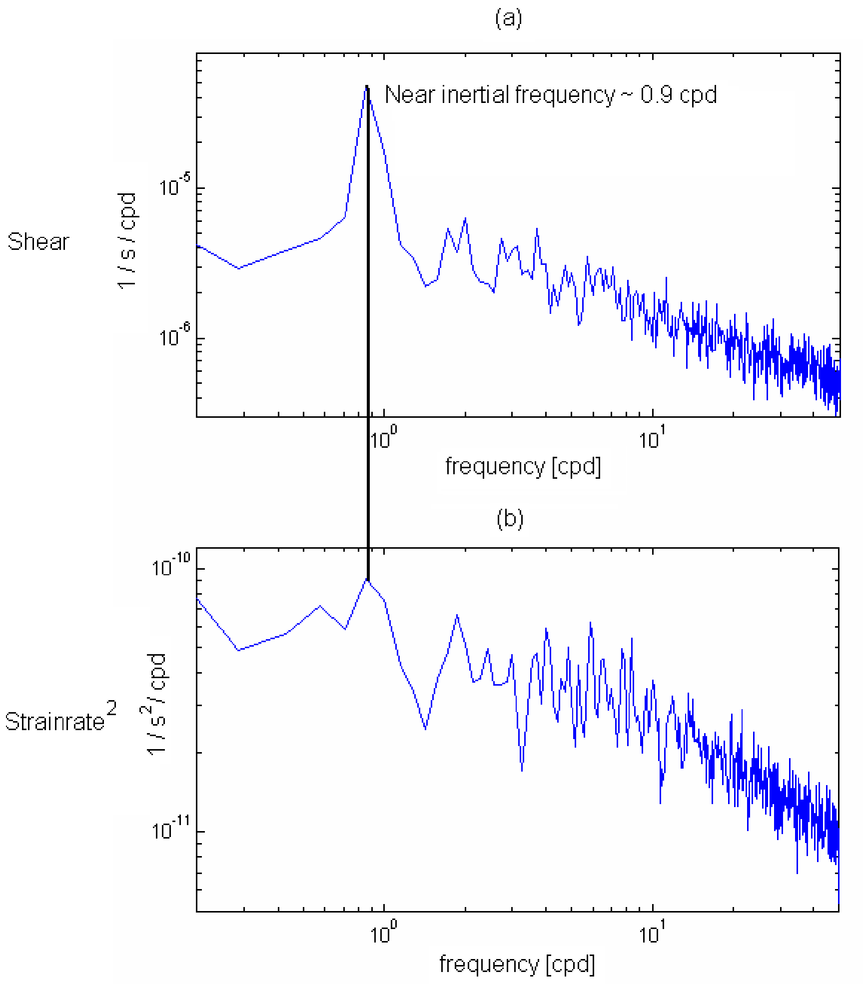

Figure IV.10: Observations over Kaena Ridge. Line at location of near-inertial frequency of 0.9 cycles per day. Data over the one week of interest, year day 260 to 267, and the depths of interest, 425 to 475 meters. This is a 52 degree of freedom estimate. (a) Cross-ridge shear frequency spectra normalized by the buoyancy frequency calculated from the CTD profiles. (b) Strain rate squared frequency spectra calculated from the CTD profiles.

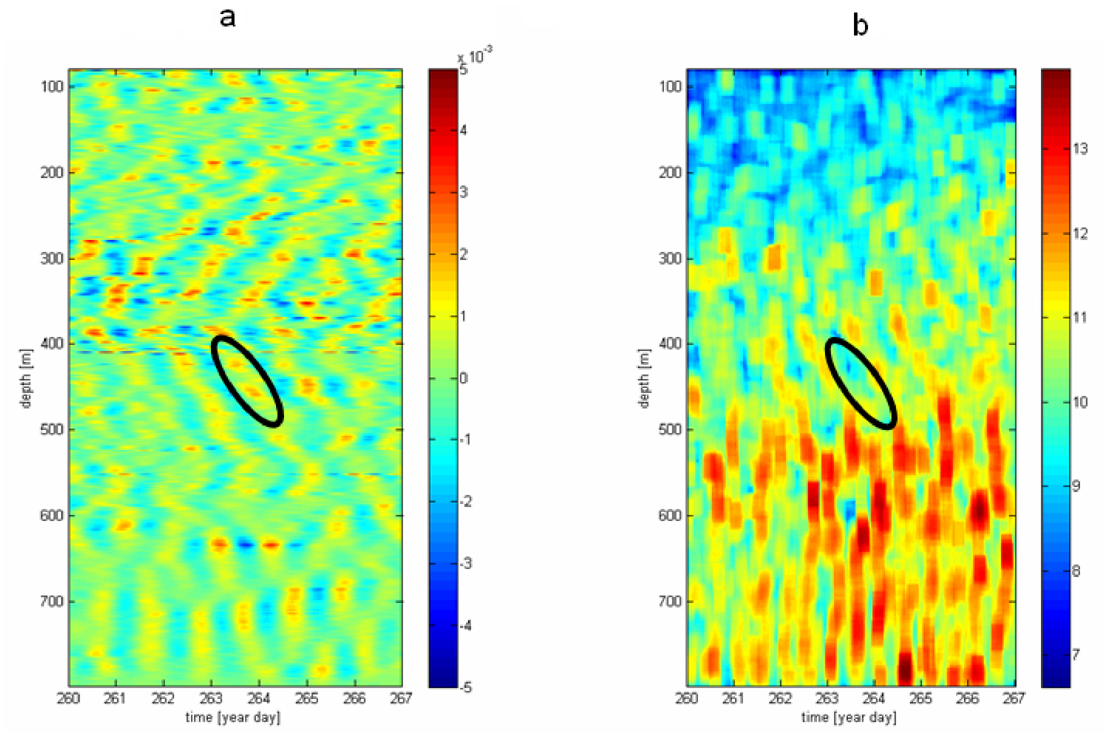

Figure IV.11: (a) Cross-ridge shear normalized by buoyancy frequency [dimensionless] calculated from the CTD profiles, filtered to only include low frequencies. (b) Strain rate squared [1/days^2] calculated from the CTD profiles, smoothed with a 30 meter, 6 hour smoothing function.

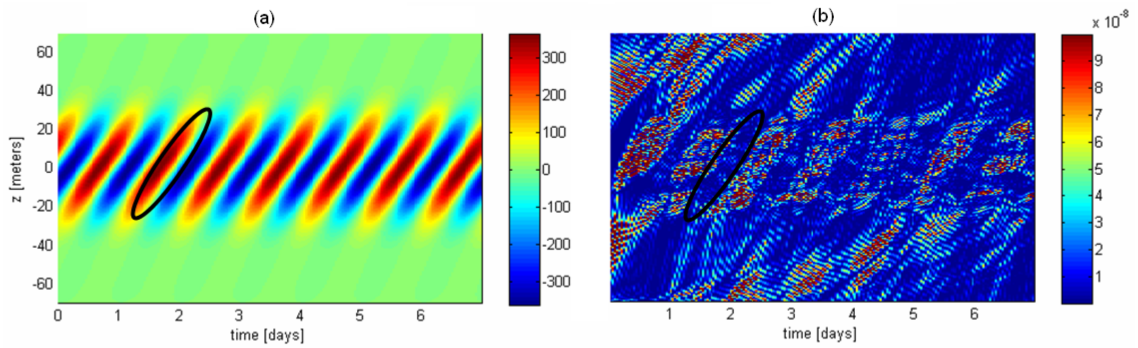

Figure IV.12: Numerical simulation results. (a) The shear from the near-inertial wave, the colorbar units are [1/days]. (b) The squared strain rate of the short wave as defined in the text, colorbar units are [1/days^2], and include only high frequency waves.

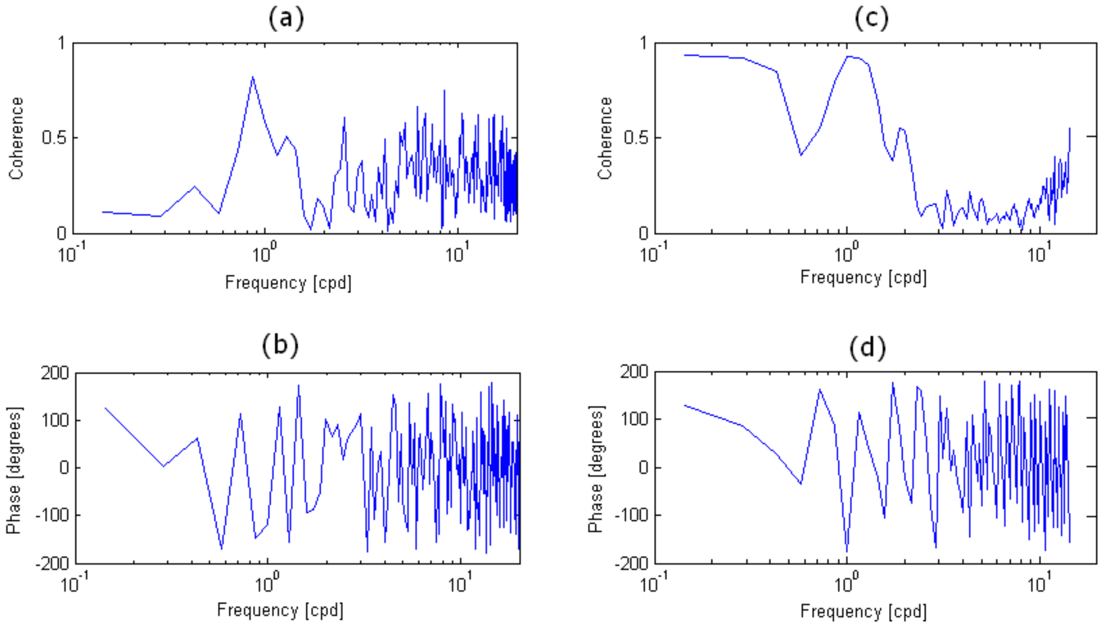

Figure IV.13: Coherence and phases between the near-inertial cross-ridge shear and the high frequency squared strain rate in the area of modulation. This is a 52 degree of freedom estimate. (a) Coherence in observations, (where the squared strain rate is smoothed using a 30 m 6 hr smoothing) over one week at depths 424 m to 476 m. (b) Phase corresponding to (a). (c) Coherence in numerical simulation over one week and 50 m depth. (d) Phase corresponding to (c).

is greater than the phase speed. Again a strong relationship between shear and squared strain rate is seen. These short waves are not propagating very far into the location of positive shear. In the observations this is the case as well.

A calculation of the coherence between these two fields, in the observations between 424 meters depth and 476 meters, and in the numerical simulations between −25 meters depth and 25 meters, is shown in Fig. IV.13, along with the phase of the relationship. This is a 52-degree of freedom estimate. There is a spike near the diurnal frequency in the coherence in both the observations and numerical simulations. The phase shows the two quantities at this frequency are about −150° out of phase from one another in the observations and close to −180° out of phase from one another in the numerical simulations. There is a strong relationship between the two fields in both the ovservations and numerical simulations which suggests the same type of interactions may be occuring in both.

This preliminary analysis leads us to believe that short internal wave parameters and possibly breaking are dependent on their propagation through time-dependent shears in the ocean, specifically inertial waves. These results present a strong argument for a need to understand how the squared strain rate field is affected by the near-inertial waves, whether it is by unsteady shear interactions or not, and that single wave-wave interactions may be able to provide a good basis for understanding the basics of this phenomenon.

IV.C Triple Product

A study of the triple product will help us better understand where, during the interaction between the short wave packet and long wave packet, turbulence is being produced. This particular quantity which we call the triple product has not been used for analysis in previous observations because the necessary data has not been available. Now, with all the data collected on FLIP during HOME we have the ability to calculate this parameter and can compare it to other methods of calculating internal wave propagation. The triple product is defined as:

$$TP = \overline{uw}\frac{\partial U}{\partial z} \tag{IV.8}$$

where lowercase letters are for the small-scale, high-frequency waves and the capital letters denote background inertial wave parameters. Note that here, $\overline{uw}$ is the Reynolds stress divided by the density.

The significance of the triple product is its relationship to the turbulent energy production,

$$-\rho\overline{u_i u_j}S_{ij} \tag{IV.9}$$

where S_{ij} is the mean rate of strain defined as:

$$S_{ij} = \frac{1}{2}\left(\frac{\partial U_i}{\partial x_j} + \frac{\partial U_j}{\partial x_i}\right) \tag{IV.10}$$

which for our idealized case, where $V \approx 0$, relates directly to the triple product,

$$TP = -\rho\overline{u_i u_j} S_{i,j}(-2/\rho) \ . \tag{IV.11}$$

For this system we assume the background is a quasi-steady mean flow and the short waves are small fluctuations to that flow. Then the total velocity of the flow is the sum of the background and short wave ($u_{\text{total}} = \mathrm{U} + \mathrm{u}$). We assume $\partial U/\partial t = 0$ (this is true for the average velocity) in order to use the equations of motion for turbulent flow.

The equations of motion for the steady mean flow in an incompressible fluid are

$$U_j \frac{\partial U_i}{\partial x_j} = \frac{\partial}{\partial x_j}\left(\frac{T_{ij}}{\rho}\right) \tag{IV.12}$$

and

$$\frac{\partial U_i}{\partial x_i} = 0 \ . \tag{IV.13}$$

The equation for mean flow energy, $\frac{1}{2}U_i U_i$, is then obtained by multiplying IV.12 by U_i. The stress tensor is $T_{ij} = -P\delta_{ij} + 2\mu S_{ij} - \rho\overline{u_i u_j}$ (Tennekes and Lumley [58]). P is a mean value, ν is the kinematic viscosity, and the resulting equation is:

$$U_j \frac{\partial}{\partial x_j}\left(\frac{1}{2}U_i U_i\right) = \frac{\partial}{\partial x_j}\left(-\frac{P}{\rho}U_j + 2\nu U_i S_{ij} - \overline{u_i u_j} U_i\right) - 2\nu S_{ij} S_{ij} + \overline{u_i u_j} S_{ij} \ . \tag{IV.14}$$

The first term on the right hand side of the equation is a measure of the pressure work, the second term is the transfer of mean flow energy by viscous stresses, and the third term is the transfer of mean flow energy by Reynold's stresses. Since turbulent stresses perform the deformation work, the kinetic energy of the turbulence benefits from this work. Thus $-\rho\overline{u_i u_j} S_{ij}$ is called the turbulent energy production. So when the triple product as defined here is positive the there is a transfer of energy to the background, longer waves. When the triple product is negative then there is turbulent energy production, and energy is being transferred to smaller scales.

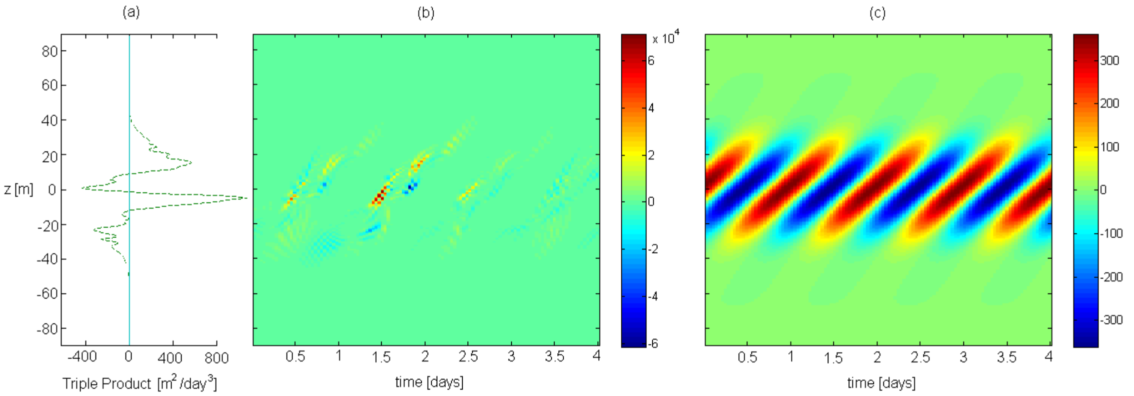

Figure IV.14: Numerical simulations of a third-kind encounter, $m/k = -35$ initially. (a) Triple product averaged over time [m^2/day^3], $\overline{uwU_z}$. (b) Triple product [m^2/day^3]. (c) Background shear [1/day].

IV.C.1 Triple Product in Numerical Simulations

We now compute these same diagnostics for the numerical simulations in order to make a comparison with observational data.

The triple product in the numerical simulations for a third-kind encounter, as well as the background shear, is shown in Fig. IV.14. The initial setup for this simulation is the same as previously, where the short waves are approaching from below the inertial wave with an initial vertical wavenumber of $m = -35k$. Fig. IV.14a is the triple product averaged over time, defined as $\overline{uwU_z}$. Fig. IV.14b is the triple product at each location in the flow. Fig. IV.14c is the background shear in the simulations. This data shows the triple product is greatest where the shear is strong, but generally has a different sign than the shear.

Fig. IV.15 shows the triple product and Reynolds stress averages over five inertial periods. We can see that for this single interaction the Reynolds stress is negative where the shear is largest and the short wave is refracting strongly as it goes through the inertial wave. Elsewhere the Reynolds stress is positive. The triple product also changes over the interaction, becoming both positive and negative, but at both the entrance and exit it is positive. The triple product is negative at locations of strong refraction where the short wave is extracting energy from the long wave. Since the average of the shear over time in this ideal setup is zero, it is ben-

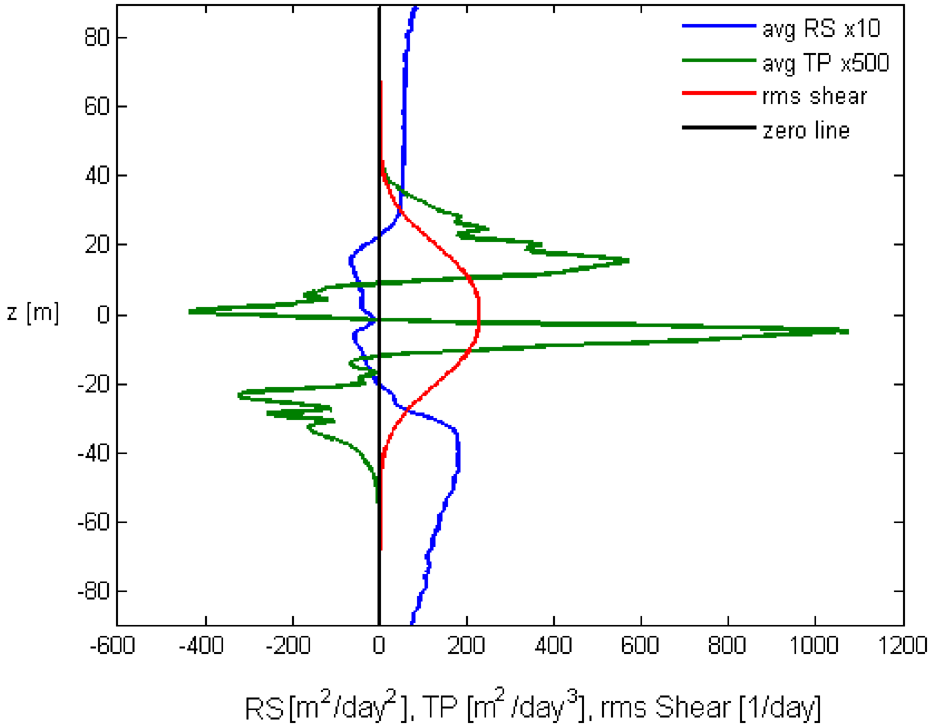

Figure IV.15: Numerical simulations of a third-kind encounter. Average Reynolds stress (×10) [$\mathrm{m}^2/\mathrm{day}^2$], $\overline{uw}$, (blue), average triple product (×500)[$\mathrm{m}^2/\mathrm{day}^3$], $\overline{uwU_z}$, (green), and rms shear [1/day], $\sqrt{\overline{U_z^2}}$, (red).

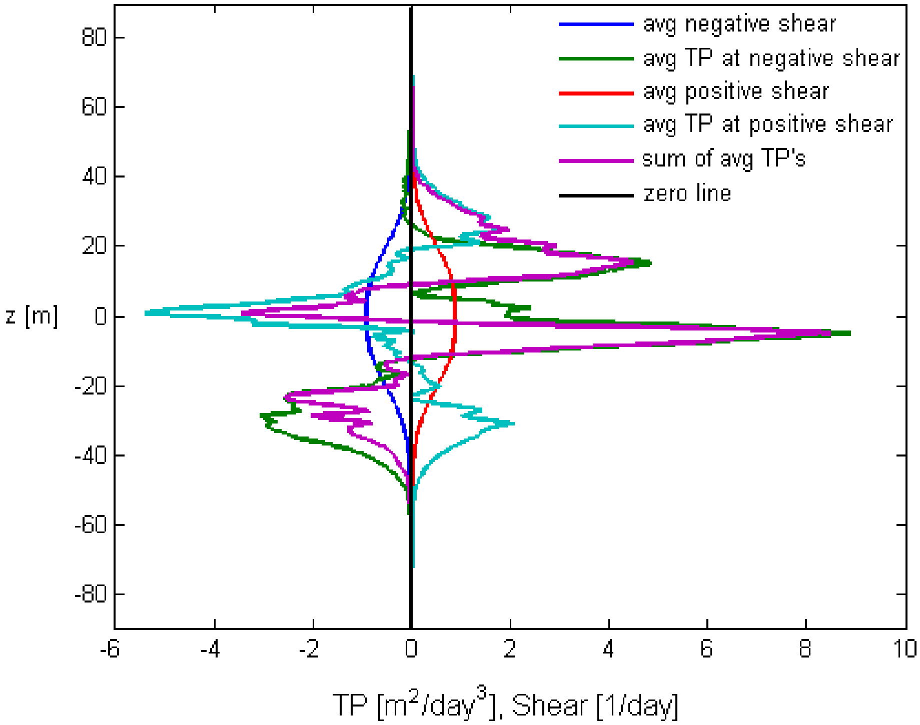

Figure IV.16: Numerical simulations of a third-kind encounter. Average positive shear over time and average negative shear over time [1/day] (red positive, blue negative), average triple product at positive shear locations [m^2/day^3] (light blue), average triple product at negative shear locations [m^2/day^3] (green), and sum of the average triple products [m^2/day^3] (purple).

eficial to look at the average triple product since it relates to positive or negative shear. Fig. IV.16 shows the triple product averages split between locations when the shear is positive and when the shear is negative. In this case we see the triple product averages are approximately opposite, with the average triple product generally corresponding to negative shear areas dominates the total average triple product. This would suggest strong interactions mainly occuring in regions of negative shear.

The setup here is an interesting one though, as there is a single short wave interacting with a single long wave. There are no short waves which are not strongly refracted averaging into the equations for the triple product. With just this single interaction we see a general trend of short waves taking energy from the inertial wave initially, but giving back more before the short wave exits, resulting in a net transfer of energy to the inertial wave. This matches the results in the previous chapters showing the amplitude of the short waves in the third-kind encounter decreasing as they exit the inertial wave. This drop in amplitude is not as drastic for a first-kind encounter, where the first refraction is to higher vertical wavenumber and smaller group speed, and the final refraction is generally back to its initial vertical wavenumber and group speed, resulting in almost no loss in the final amplitude of the short wave.

IV.C.2 Triple Product in Ray Tracing

Although the results of the previous section are interesting and give us a feel for how a single interaction will affect the different properties of interest, because there are many more waves in the ocean it seems a good idea to create a statistical set of data from ray tracing simulations. In this sense we can cover all types of encounters at once and average over them all. We input 1500 rays total, with 500 different equally spaced frequencies between $2f$ to $0.99N$, 3 rays at each frequency have different initial positions, within 3 meters of one another.

In Fig. IV.17a all of the 1500 short waves are travelling upward through the inertial wave and they strongly refract as they propagate through the inertial

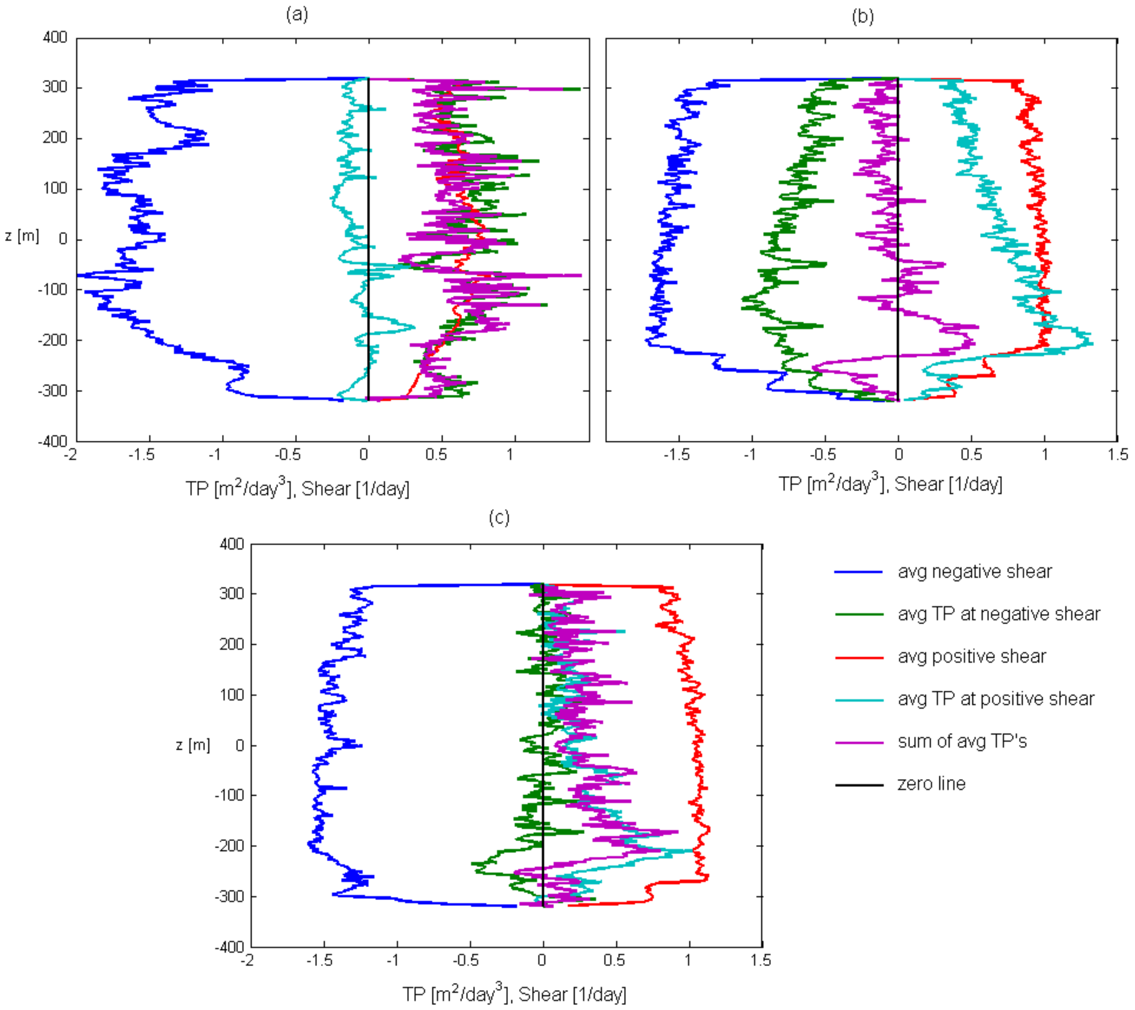

Figure IV.17: Ray tracing calculations of a set of 1500 waves with different initial depths and frequencies ranging from $2f$ to $0.99N$. Average shear ($\times 10^5$) over time [1/day] (red positive, blue negative), average triple product ($\times 10^7$) at positive shear locations [m^2/day^3] (light blue), average triple product ($\times 10^7$) at negative shear locations [m^2/day^3] (green), and sum of the average triple products ($\times 10^7$) [m^2/day^3] (purple). (a) Upward travelling waves. (b) Downward travelling waves. (c) Equal number of upward and downward travelling waves.

wave. We can see there seems to be a greater average negative shear for the ray tracing. This is because the shear is being calculated only along the ray, so a greater average negative shear means the short waves are spending more time in locations of stronger negative shear. Although there are many different locations of strong refraction there is a more regular trend of a positive triple product at locations of negative shear. This dominates the triple product calculation, and the average triple product at locations of positive shear, which is generally negative, has a small effect on the total average triple product. So again we see the negative shear locations dominating the triple product calculations. Also, because the overall triple product is positive the short waves are transferring energy to the inertial wave as they strongly refract.

In Fig. IV.17b all of the 1500 short waves are downward travelling waves which refract as in the critical layer case, but because of the propagating phases of the background the critical layer soon vanishes and the wave propagates unchanged again. There is a strong signal of a negative triple product when the shear is negative, and a positive triple product when the shear is positive. These combine to give a near-zero triple product throughout the simulation. Little energy is being transferred between the short and long wave during this interaction. In this scenario the short waves may begin to approach a critical level and refract, but then as the phases of the long wave propagate through the critical level also propagates through and the short wave refracts back to its original properties with no net exchange of energy between the long and short wave.

When we have an equal number of upward and downward travelling waves, as in Fig. IV.17c, where 750 short waves are initiated below and 750 above the inertial wave, we see a smaller triple product, although overall it is still positive. Here the downward travelling waves, which have a positive triple product during positive shear locations, seem to dominate. This makes sense as the short waves transfer energy as they strongly refract, but generally exit with a smaller amplitude, therefore having lost energy to the inertial wave, whereas those short waves which do

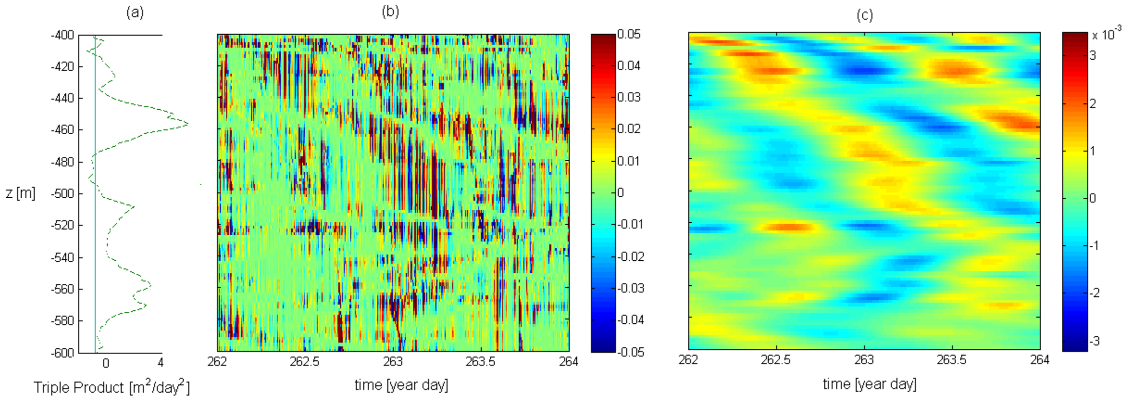

Figure IV.18: Observational analysis of flow over Kaena Ridge for two days over 200 meters. (a) Triple product averaged over time [m^2/day^2], $\overline{uwU_z}/N(z)$. (b) Triple product [m^2/day^2]. (c) Background shear [1/day].

not strongly refract will keep their energy throughout the interaction. (Although in these cases we do not actually see changes in the inertial wave because it is set as a constant, and although it may be increasing in energy the change is small compared with its original energy.) The result is that overall, short waves which interact with the inertial wave are transferring energy to it and leaving the interaction less likely to break, unless they break during the interaction, which will be investigated later.

IV.C.3 Triple Product in Observations

For the observational calculations we divide the shear by the buoyancy frequency because it changes over the depth of the ocean. Fig. IV.18a shows the triple product averaged over time, defined as $\overline{uwU_z}/N(z)$. Fig. IV.18b is the triple product at each data point collected. Fig. IV.18c is the background shear calculated by filtering the data to see only the near-inertial shear. Here we can see the triple product is greatest, positive or negative, in locations of strong positive or negative shear. Fig. IV.18a shows the average triple product is generally positive, as we have seen in previous cases.

Fig. IV.19 is the result of calculating the Reynolds stress and triple product from observational calculations and averaging over two days. The two days were chosen to be those where the inertial waves propagating upward through the ocean

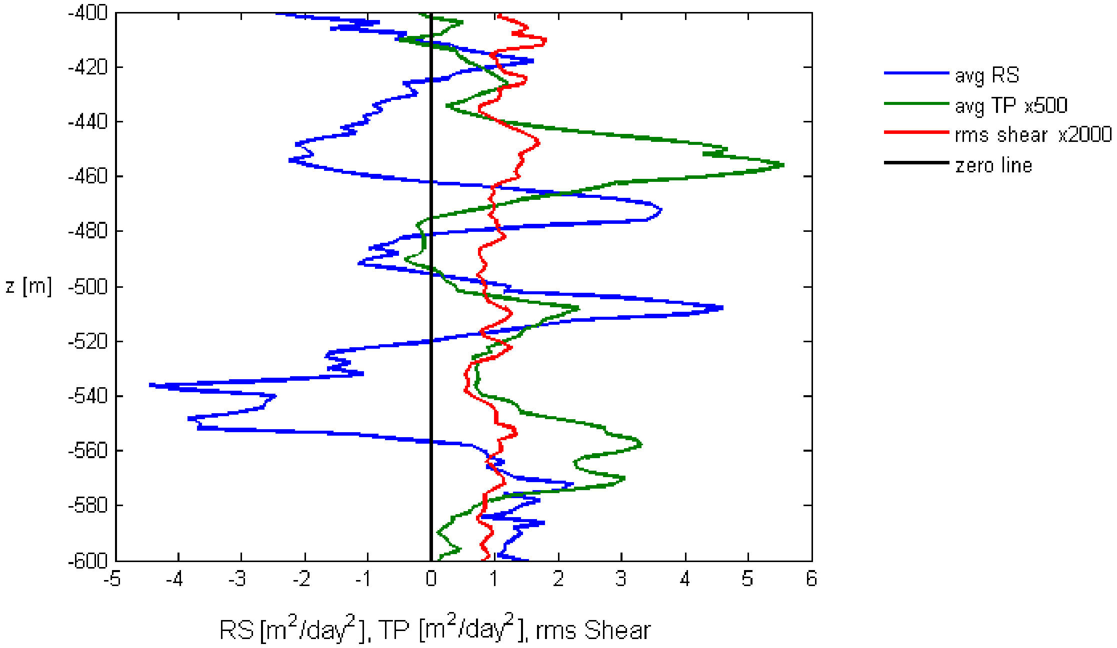

Figure IV.19: Observational analysis over Kaena Ridge, averaged from year day 262 to 264. Shear is divided by the buoyancy frequency as it is variable over the ocean depth. Average Reynolds stress [$\mathrm{m}^2/\mathrm{day}^2$], $\overline{uw}$, (blue), average triple product ($\times 500$)[$\mathrm{m}^2/\mathrm{day}^2$], $\overline{uwU_z}/N(z)$, (green), and rms shear ($\times 2000$) [dimensionless], $\sqrt{U_z^2}/N(z)$, (red).

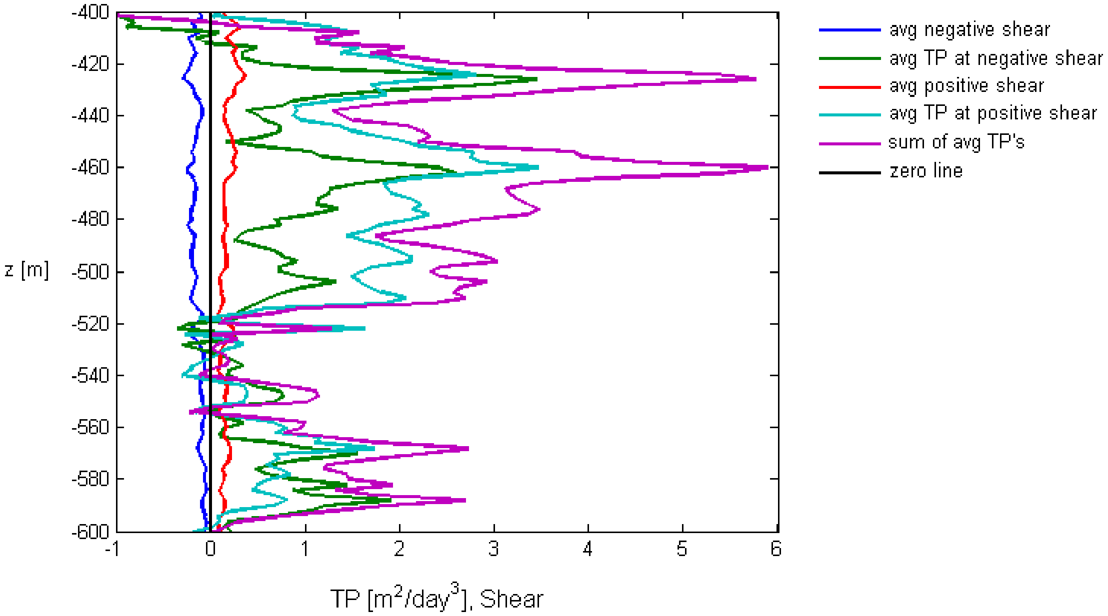

Figure IV.20: Observational analysis over Kaena Ridge, averaged from year day 262 to 264. Shear is divided by the buoyancy frequency as it is variable over the ocean depth. Average shear (×10^5) over time [1/day] (red positive, blue negative), average triple product (×10^5) at positive shear locations [m^2/day^2] (light blue), average triple product (×10^5) at negative shear locations [m^2/day^2] (green), and sum of the average triple products (×10^5) [m^2/day^2] (purple).

were dominant. We see the Reynolds stress is both positive and negative, but the average triple product is positive almost everywhere. Fig. IV.20 is averaged for the same two days and shows that during positive shear regions the triple product is positive, as it is in the negative shear regions as well. This looks somewhat like Fig. IV.17c, which is the ray tracing of short waves propagating both with and against the inertial wave. The balance between upward and downward propagating waves would be important in defining the value of the triple product, as well as the location of short waves. Since they are spread out initially, the short waves have the negative triple product regions seen in Fig. IV.16 but they will not show up with the greater positive triple product from other averaged areas. Also, the positive shear locations have a positive triple product as the waves propagating downward are not strongly refracting, but keeping most of their energy.

When the triple product is positive the short waves are transferring energy to the long waves. This is occurring in numerical simulations, ray tracing, and observations. This corresponds to short waves strongly refracting through longer waves, exiting with a smaller vertical wavenumber and decreased amplitude. In the next section we will see why it is the negative shear areas that dominate when the short waves may be strongly refracted and possibly break.

IV.D Wave Breaking

We calculate wave-breaking by calculating when isopycnal displacements are such that $\zeta_z > 1$, where ζ_z is a measure of the wave steepness as discussed previously. This leads to overturning within the fluid and resulting turbulence. This can be calculated in the numerical simulations and observations by finding $\Delta\zeta/\Delta z$.

IV.D.1 Wave Breaking in Numerical Simulations

A wave breaking map for the numerical simulation is shown in Fig. IV.21b. Next to it, Fig. IV.21a, is the corresponding background wave shear field. Notice the

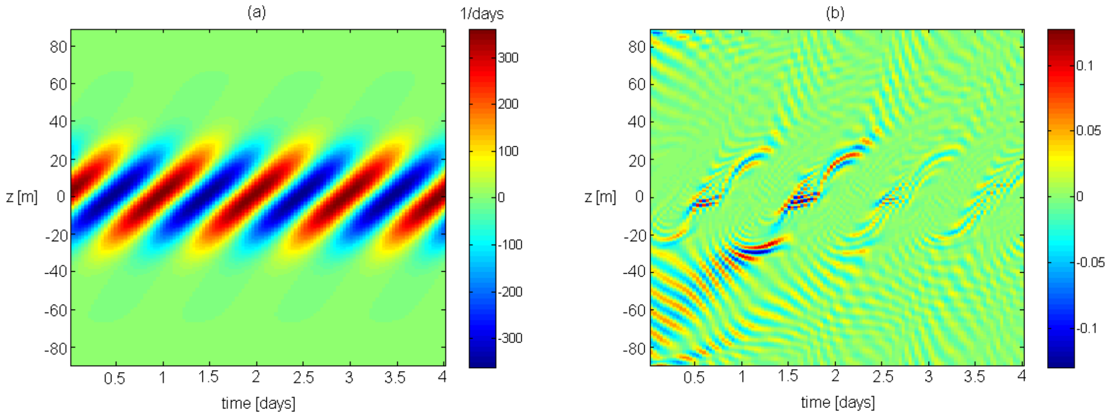

Figure IV.21: Numerical simulation of a third-kind encounter, where initially $m/k = -35$, and $\zeta_z = 0.1$. (a) Background shear [1/days]. (b) Possible breaking map for numerical simulation of a third kind encounter. The colorbar represents ζ_z

colormap in Fig. IV.21b represents the wave-breaking parameter ζ_z, and does not ever go to 1. So breaking is not occurring in these simulations, as we already knew, but we can see where the wave steepness is greatest and therefore if the amplitude of the original short wave were increased these would be the locations of probable breaking. In the numerical simulations the short wave travels in between locations of high and low shear, through locations of zero shear, going from negative to positive shear. We can see the wave steepness begins to increase as soon as the short wave is first strongly refracted, which is at a location where the background shear is negative for first kind encounters, and positive for third kind encounters (this will be described further in the next section addressing ray tracing). Where negative shear corresponds to the velocity of the inertial wave, in the direction of short-wave propagation, decreasing with depth. The increase in short-wave steepness at the location of strong refraction makes sense as we have seen the amplitude of the short-wave increases at locations of strong refraction. If the background velocity were large enough the strong refraction locations would be in areas of relatively large positive and negative shear because they would be relatively far from the maximum and minimum velocity locations.

In the first-kind encounter we expect to see breaking in regions of negative

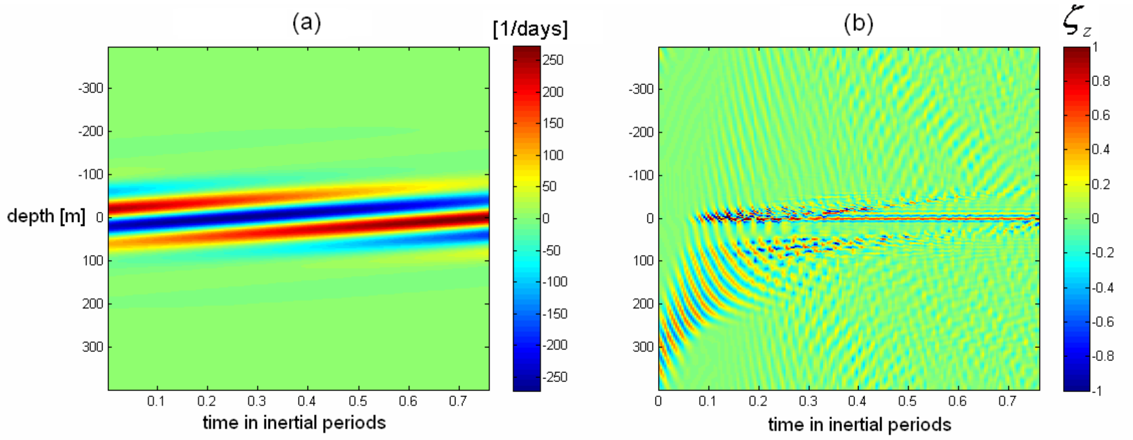

Figure IV.22: Numerical simulation of a first-kind encounter, where initially $m/k = -3$, and $\zeta_z = 0.6$. (a) Background shear [1/days]. (b) Possible breaking map for numerical simulation of a first-kind encounter. The colorbar represents ζ_z

shear, which can be seen in Fig. IV.22. This displays breaking of short waves which propagate into a region where the background wave velocity is increasing in the direction of vertical short wave propagation. Also the short waves are propagating in the positive horizontal direction.

If we increase the initial wave steepness of the short wave to $\zeta_z = 0.9$ than we are almost positive breaking should occur. Fig. IV.23 shows this situation for the third kind encounter. Since the numerical simulations are only two-dimensional and breaking is three-dimensional the breaking will not be resolved. In these simulations what we see is instability within the short wave packet. There is no longer a clean packet with nice phases, but the crests are altered and look wavy. This is showing locations of breaking within the short wave. These begin at the first location of refraction corresponding to each area of the short wave packet, which was at a location of negative shear as can be seen in Fig. IV.21. The short wave seems to curve around the negative shear area as it is refracted. This is what we would expect from the previous results of where the wave steepness parameter, ζ_z is greatest.

If we increase the initial wave steepness even further, for the wave to be unstable initially, $\zeta_z = 1.5$, the results can be seen in Fig. IV.24. At the initial time we see the same type of unstable behavior as seen in Fig. IV.23 at the locations

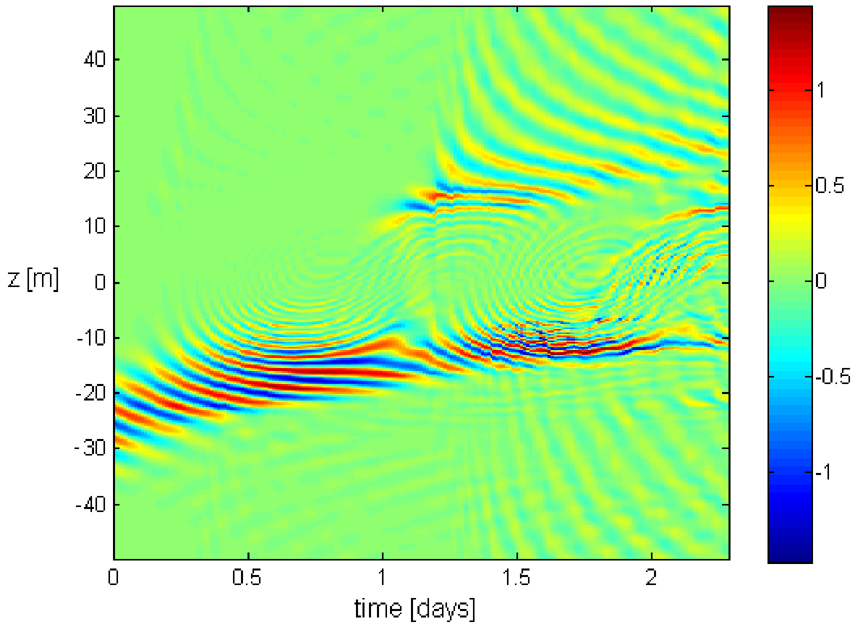

Figure IV.23: Breaking map for numerical simulation of a third kind encounter with an initial wave steepness of $\zeta_z = 0.9$ and $m/k = -35$. The colorbar represents ζ_z

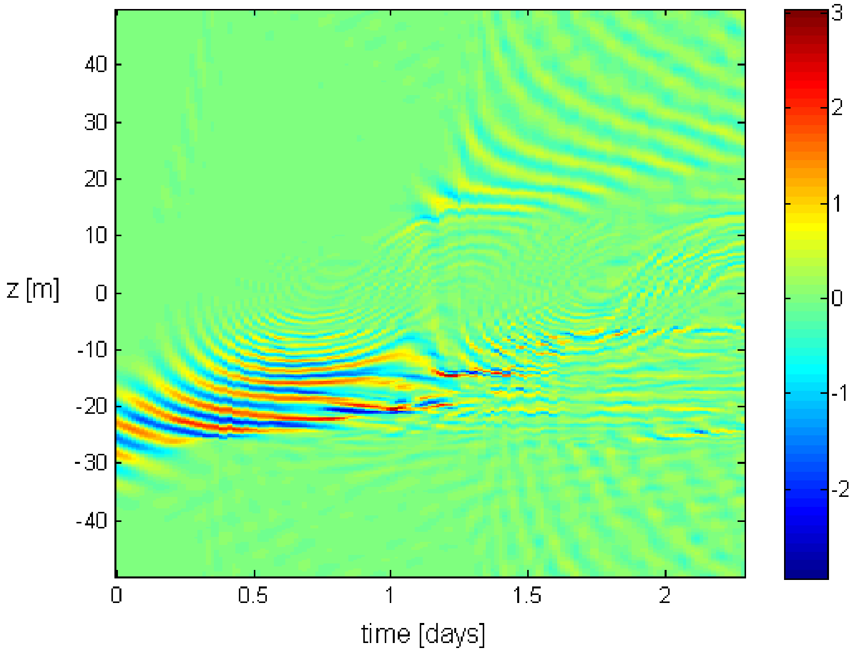

Figure IV.24: Breaking map for numerical simulation of a third kind encounter with an initial wave steepness of $\zeta_z = 1.5$ and $m/k = -35$. The colorbar represents ζ_z

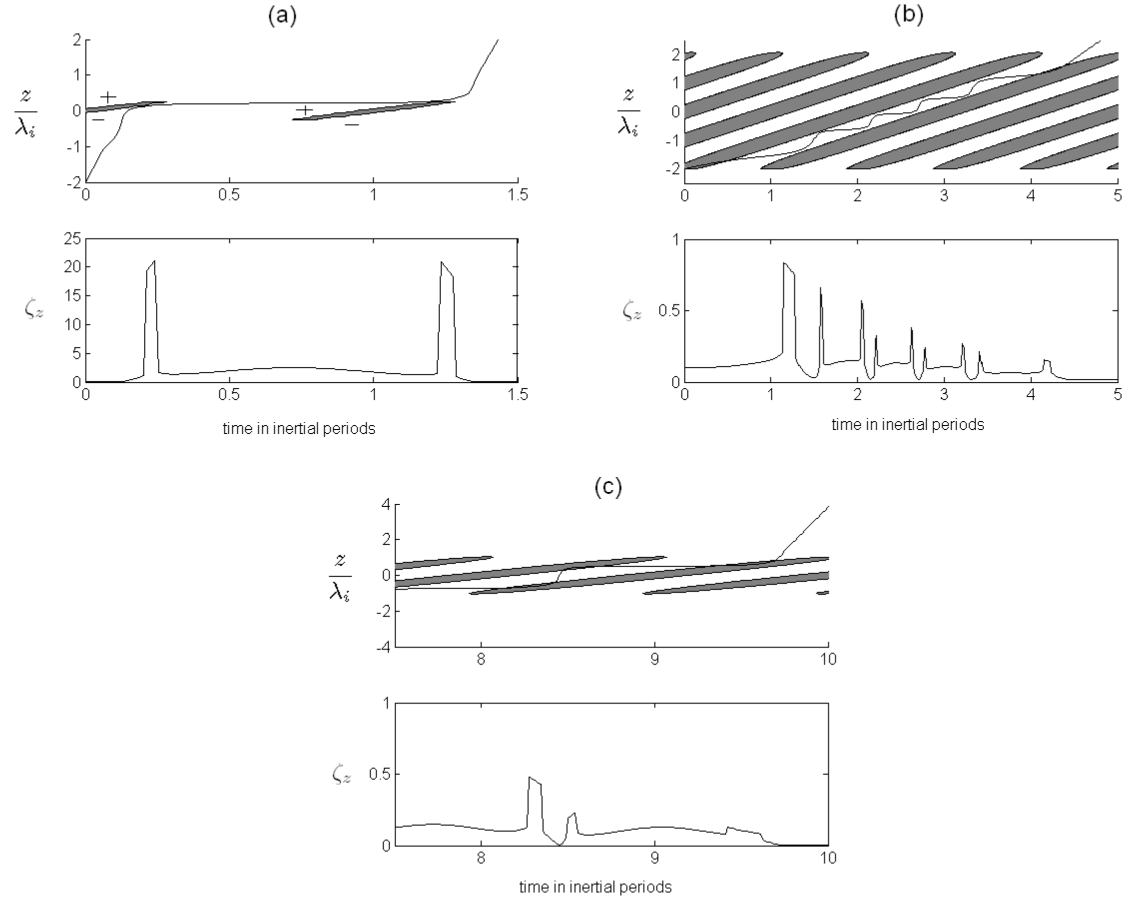

Figure IV.25: Ray paths for different rays within the ray tracing simulation where the filled in ellipses are outlined by locations of strong refraction and corresponding ζ_z values along the ray. (a) First-kind encounter, $m/k = -3$. Notice the locations of positive and negative shear which outline the ellipses. (b) Second-kind encounter, $m/k = -12.25$. (c) Third-kind encounter, $m/k = -35$.

of strong refraction. But in Fig. IV.24 at the locations of strong refraction the numerical simulations are not only somewhat unstable, but seem to be turbulent, which is not at all resolved by these numerical simulations. Again, we see the strongest instability occurring at the first location of strong refraction corresponding to negative background shear. We also notice the curviture of the short wave as it is refracted and breaks, as later this will match the observations.

IV.D.2 Wave Breaking in Ray Tracing

The calculations for finding breaking in the ray tracing are harder and we only see the wave-breaking parameter along the paths of the short waves. A different approach as there is not information over the entire spatial domain, but only along each short wave ray path. For this we use the dispersion relation and (II.3) to derive:

$$\zeta_z = -m \left| \left(\frac{2A\hat{\omega}}{\rho_0} \right)^{1/2} N^{-1} \right| \ . \tag{IV.15}$$

Fig. IV.25 shows the ray lines, locations of strong refraction outlined by filled in ellipses, and the corresponding ζ_z values. These values are estimated at the caustics with the corrected amplitude calculated previously. We see that in each of the three encounters the largest steepness is at locations of strong refraction. In the second and third kind encounters these locations correspond to refraction at positive shear. The locations of positive and negative shear within the ellipses is shown in Fig. IV.25a, which shows the upper left portion of the ellipse corresponds to positive background shear and the lower right portions correspond to negative background shear. These plots look much like those shown previously for the amplitude of the short wave. In the ray tracing calculations the amplitude of the short wave approaches infinity as the caustic is approached. We see the first-kind encounter has the largest increase in wave-steepness at the caustic, and would be most likely to break if each of these short waves had the same initial wave steepness.

If we look back to Figs. II.3, II.5, and II.6 we can see that there is a drop in the vertical wavenumber at locations of strong refraction. This drop is very small in the first kind encounter, and an order of magnitude in the third kind encounter. This may have an effect on the steepness, $\zeta_z = m\zeta_0$, at the location of strong refraction. For constant initial wave steepness, ζ_0 will be smaller for the third-kind encounter because its vertical wavenumber is larger. But at the location of strong refraction the vertical wavenumber drops an order of magnitude, and the amplitude is corrected as discussed previously. Whereas in the first-kind encounter the vertical wavenumber has only a slight decrease in value at the location of strong refraction,

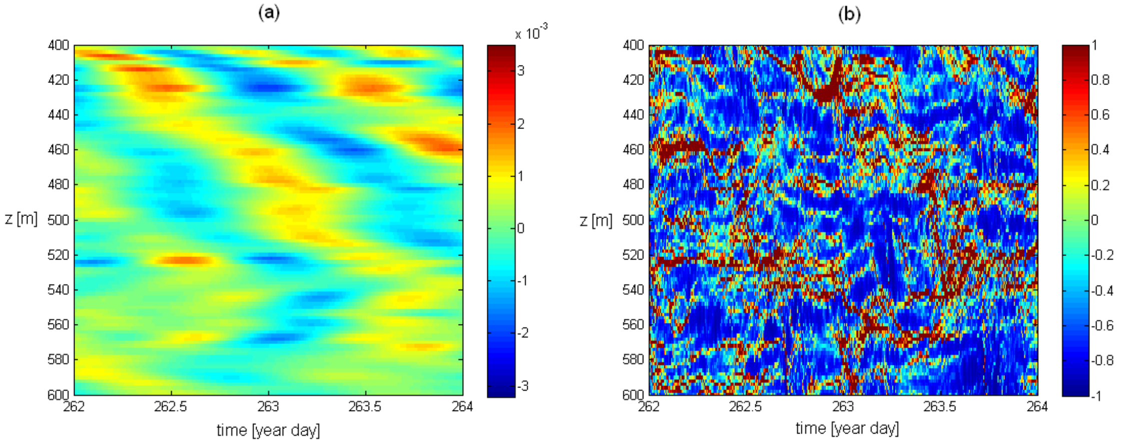

Figure IV.26: Observational analysis over Kaena Ridge for two days over 200 meters depth. (a) Inertial shear divided by buoyancy frequency. (b) Wave breaking map calculated from CTD data. The colorbar represents ζ_z.

and the amplitude is again corrected.

Also relating this back to the statistical analysis, breaking of the short waves of the first kind would result in taking energy from the highest frequencies, but then the third-kind encounters interact and transfer their energy, although less than their original energy, back to the higher frequencies. This shift may keep the balance, resulting in a realistic ocean spectrum that may have shifted to less energy because of the loss of energy to mixing and to third kind encounters upgrading to first kind encounters. As we saw in Chapter II, the final energy spectrum for a single third kind encounter interacting with an intertial wave has a realistic ocean slope. If the first-kind encounters are breaking and the third kind encounters are redistributing their energy, the realistic energy spectrum may be kept intact while we see breaking in the negative shear regions of the ocean where the encounters of the first kind are breaking.

IV.D.3 Wave Breaking in Observations

The observational results of calculating the breaking parameter, ζ_z, from the CTD data over two days and 200 meters depth are shown in Fig. IV.26b. The corresponding filtered inertial shear is shown in Fig. IV.26a. These results show a strong relationship between breaking and negative shear, as we did in the ray tracing and numerical simulations. Wave breaking coincides with negative shear.

If the waves are of large enough initial amplitude to break, they will break just after the first strong refraction location. Therefore, whether or not the shear is positive or negative when the short waves break, they may be able to have a relative effect on the background shear in the form of acting to push the wave upwards as the short waves propagate upwards and proceed to distribute their energy near the base of the inertial wave, acting with a net positive effect on the background.

In the simulations, ray tracing, and observations, it seems that breaking is occuring at locations of negative shear. In the numerical simulations and ray tracing the short waves most likely to break are first strongly refracted in a location of negative shear. The corresponding observational plots then have locations of breaking mainly where the background shear is negative as well.

Why do the short waves first refract when the shear is negative? As the inertial wave phases propagate downwards, the first possible location of strong refraction within the shaded locations of strong refraction as shown in Fig. II.3a corresponds to high negative shear. The short waves that refract strongly at these locations are first-kind encounters, and they are also the most likely to break because of their large increase in wave steepness at the location of strong refraction. It is also interesting again to notice the curvature of some of the breaking regions in Fig. IV.26b, which match the curvature seen in the numerical simulations when the single short wave packet first interacts with the inertial wave in Fig. IV.21b.

If some short waves of the spectrum are able to be refracted, they will create internal wave activity at locations between negative and positive shear locations. Those short waves that cannot be strongly refracted will have wave activity at all locations and not depend on the sign of the background shear. We have seen that short waves which can be strongly refracted and have the highest probability of breaking will generally break in a region of negative shear. Waves which enter the inertial wave with a slow vertical group speed, which may break in regions of positive shear, also have a smaller wave steepness at locations of strong refraction and thus are less likely to break. So they may not be as important to the breaking dynamics. Then the net total of a number of waves travelling through an inertial wave will be an increase in short wave breaking mainly at negative shear locations. But if these waves were to travel in the opposite direction, such as westward travelling waves instead of eastward, they would be breaking in locations of positive shear instead of negative. So these results of breaking during negative shear locations show a possibility of short waves propagating in one direction for a period of time.

IV.E Discussion

The results shown in this chapter have given us insight into one of the mechanisms of short wave breaking in the ocean. This is when short waves created by flow over topography, small mixing patches, etc., propagate upward through the ocean and propagate into long inertial waves. Observations have shown these phenomenon occurring, and this analysis shows the same results when looking at the phenomenon in the ocean, numerical simulations, and ray tracing. We see breaking occurring at locations where the background shear is decreasing with increasing depth and the short waves have a group speed in the positive horizontal direction. The importance of these methods matching is that they can be used simultaneously, in sequence, or individually and the results should be comparable. This means that in the future we can more confidently use ray tracing, which is very fast, and numerical simulations, which are still faster than collecting observational data, to understand short-wave propagation throughout the ocean.

We also found that when the short waves do not break they have a net transfer of energy to the inertial wave. This is because the short waves generally exit with a faster group speed and smaller vertical wavenumber. These short waves are then less likely to break when the next inertial wave propagates downward through the ocean.

Combining information from all three methods, we have found short-wave breaking in regions of negative shear in the ocean, corresponding to high-frequency waves travelling in the same direction breaking and dissipating their energy within the inertial wave interaction. Then the lower frequency waves which interact with the background wave redistribute their energy to those high frequencies, resulting in a realistic ocean spectrum both before and after the short waves propagate through the inertial wave.

V

Conclusions

For the thermohaline circulation to continue working as it does today there are certain energy constraints that must be met. As mentioned previously, approximately 1 TW of energy is input into the deep ocean from the tides, in addition to the approximately 1 TW already input by wind-driven waves. Recent data has shown a strong case for some of the tidal energy being dissipated by flow over topography creating internal gravity waves. These waves break, some immediately, and some after propagating further into the ocean and interacting with other waves, and mixing results. It is important to study each of these parts of this energy cascade from tidal energy, to internal gravity waves, to smaller breaking scale waves, to turbulence and mixing, to understand how the process fits into the overall ocean circulation model.

The process of internal waves' propagating to waves of short enough scales where breaking may occur is one of these important pieces. Henyey and Pomphrey made some assumptions about the dissipation of short internal waves as they reached smaller scales which are still being used in some models today. These dissipation estimates do not take into account the time-dependence of the shear in the ocean and assume a cutoff for wave-breaking based on a steady background shear profile. Field data has shown that inertial waves propagate downward through the ocean, providing a time-dependent shear for the broad spectrum of wavenumbers present in the upper-ocean to propagate through. This work has addressed these interactions through a detailed study of the dynamics of an interaction between a short wave and an inertial wave, a statistical study of a number of short waves propagating through a number of inertial waves, and an observational study of this phenomenon. Results have shown good agreement between the three methods, which supports further use of ray tracing and numerical simulations as a means to study a broader range of situations within the ocean. We have also found a strong signal of short wave breaking within inertial waves, specifically the negative shear regions which shows a directional dependence on the waves in the region studied. This corresponds to short-waves of high frequencies propagating upward through the downward propagating inertial waves and breaking at their first strong refraction by the inertial wave. This breaking may be seen in other oceanographic data, and may be attributed to this type of interaction.

V.A Summary

The overall goal of this work has been to investigate short-wave dynamics as they propagate through a realistic ocean background in an effort to understand how and where short waves may break and dissipate their energy. It has been found, through a series of numerical and observational techniques, that short waves which fit the criteria to strongly refract will do so and will break at the first location of strong refraction. If this were not the case we would see a flat frequency spectrum within the ocean, as we saw in the statistical analysis. These short waves are breaking at their first location of strong refraction because of the increase in amplitude there. This creates a large wave steepness, resulting in breaking. We also saw that the short-waves with the highest probability of breaking – first-kind encounters with initially high frequencies – will strongly refract first at a location of negative shear. Those which do not are lower frequency short-waves and are propagating to higher frequencies, but smaller amplitudes while transferring energy to the background long wave. Thus we see a trend of upward propagating short waves breaking at locations of negative shear created by long inertial waves travelling downward through the ocean.

Because of the strong correlation between fully nonlinear numerical simulations, ray tracing, and the observations, we are confident in our modeling capability. This is important as we can trace many short waves through many long waves in a number of minutes using ray tracing, where numerical simulations would take a few hours, and the observations would take however long you wanted to track the short waves, as well as the time to analyze the data.

V.A.1 Single Short and Long Wave Interaction

In investigating the effect of time-dependent long-wave shear on short internal waves using ray theory and fully nonlinear numerical simulations, we have found that critical layers are rare if the model is a realistic oceanic flow. When the interactions occur, $c_g = c$, short-wave focusing results and after being refracted, the vertical wavelength of the short wave may be affected. As m is increased, there is a decrease in wave-energy, which will be transferred to the mean flow. The dissipation will depend on both the initial vertical wavelength and the initial amplitude of the short-wave. Previous assumptions about critical levels in steady shear must be carefully considered in time-dependent shear because they may not be true.

Although these results are for mid-latitude deep oceanic flows, many of the conclusions may be extended to the middle atmosphere as well.

There are a number of other neglected processes that various studies suggest are significant for short-wave dynamics, and they include some processes that have never been analyzed in the context of the model of a short and long wave interaction and that could be critical for understanding the model predictions. Interactions among short waves and short-wave induced mean flows have not yet been analyzed using this model. Other important processes with limited analysis using this model include refraction by steady shear, phase-group interactions, and ray convergence/divergence. The relative importance of steady shear versus near-inertial shear for short-wave propagation was first examined by Buckley, Broutman, Rottman, and Eckermann [8], but with a quasi-2D model and for a very limited range of conditions. Sun and Kunze [54, 55] included vertical divergence of the background and found that it sped up the refraction of the short waves toward small dissipating scales and hence increased the predicted dissipation rate of the HWF model to a value closer to reality. One problem with the Sun-Kunze study, as they say, is that the background W_z tends to be associated with internal waves whose intrinsic frequency is higher than the short waves being refracted. This calls into question – but does not necessarily violate – the validity of the slowly varying approximation of ray theory.

V.A.2 Statistical Analysis

An analysis of the wave-set phenomenon first seen by Bruhwiler and Kaper [7] led to a better understanding of the propagation of a spectrum of short waves. These short-wave results may show a propensity to exit a long-wave interaction with a particular final vertical wavenumber. Although short waves have a preferred entrance and exit location within the inertial wave, because of the relationship between the slope of the incoming ray and the slope of the locations of strong refraction, the general outcome seen in the analysis of individual waves is still valid. The propagation of a short wave through an inertial wave will lead to a decrease in the short wave vertical wavenumber, if initially $m_i^* > 1$, which corresponds to a third-kind encounter where $c_g \ll C$ corresponding to a shallower slope of short-wave propagation in $z - t$ space than for the long-wave phase propagation.

After extending the work of Bruhwiler and Kaper we see that their results seem valid over the suggested range of k values for which strong refraction may occur. Statistically the general trend in frequency space is for the short waves to propagate to higher frequencies. The results also seem to hold as the short waves propagate through a set of inertial waves, as they would in the ocean. The practically flat spectrum propagating again through an inertial wave stays approximately flat. This is interesting, as no such flat spectra have been measured in the ocean (not including locations near strong sources of internal waves). Observations have stayed close to the analytic form approximating this spectrum, by Garrett and Munk [19], which has a -2 slope. There is a possibility that short waves with larger amplitudes will break at locations of strong refraction, and therefore no flat spectrum will result. As we saw in the ray tracing analysis the highest frequency waves (first-kind encounters) may break, resulting in a decrease in the number of waves left at the high frequencies, altering the spectrum to have a negative slope again. Also, three-dimensional effects may be important here since changes in horizontal wavenumber result in changes in the group speed of the short-wave, which would alter the locations of strong refraction. It would be interesting to find the types of interactions which, with an initially realistic spectrum, after propagating through a time-dependent background shear would result in a finally realistic spectrum as well. It may also be that the number of short waves within this range of strong refraction are minimal. Although there are short waves which satisfy the limits necessary for strong refraction, how abundant are there and where are they? They may be generated by flow over topograpy, mixed regions, or flow behind an object.

We conclude that within the region of strong refraction the short wave frequency spectrum flattens, and waves are spread between the maximum and minimum possible frequencies of strong refraction. Outside of this region, as expected through theory, the short waves do not change and their final frequency and vertical wavenumber spectrum do not change from the initial. The interest then is in whether or not real spectra fall within this range or not. As further work one could test actual short wave spectra created in the ocean or atmosphere, to see whether or not the short wave parameters fall within the locations of strong refraction by an inertial wave. Also, because of these results, which show a flat frequency spectrum which is not measured in the ocean, we believe breaking of some of those waves which can refract will occur.

V.A.3 Observational Analysis

In the observations we mainly see breaking occuring within the inertial wave. This breaking occurs in locations of negative background shear for positive x-propagation of the short-wave, even though the parameter deciding whether or not the short waves can strongly refract has to do with the velocity of the background, not the shear, and thus the shear will be positive or negative at locations of strong refraction. But this phenomenon is seen in both representative ray tracing calculations and numerical simulations. It is found that generally short waves of the first kind will strongly refract first at a location of negative shear because of the dynamics of the interaction: the slope of the short wave group speed in $z-t$ space is greater than the slope of the phase speed of the inertial wave, $c_g >> C$. The short waves will reach their greatest amplitude within the first strong refraction. If the short wave has a large enough initial amplitude to break, it will at this first strong refraction location. We found first-kind encounters have the largest increase in wave steepness at locations of strong refractions, and would therefore be most likely to break. These factors result in short waves breaking in locations of negative shear.

The observations showed a net transfer of short wave energy to the background inertial wave. This corresponds to third-kind encounters which have a net transfer of energy to the background long-wave. Although we did not analyze it more fully, this may result in a net upward push of the inertial wave by the short waves. It does result in short waves with less propensity to break, though, because of their diminished amplitude.

The results of the observational analysis match fairly well with results of the ray tracing and fully nonlinear numerical simulations. This gives us faith in the methods which we have used to calculate short wave behavior, and since thousands of short waves can be traced through a number of inertial waves in a matter of hours, confidence in these methods means a decrease in computational time and power and an increase in knowledge.

V.B Future Work

There is still work to be done within this specific field. Ideally a parameterization of short wave activity and breaking would be created. Then one could represent the short-wave evolution to breaking in terms of large-scale features that are dealt with explicitly in the models. Just as an extension of the work presented here, one could further analyze the observational data and do more comparisons to verify the ray tracing and numerical simulations and their ability to recreate critical data from the observations. Also it would be of interest to terminate the short waves in the ray tracing if they were to reach a breaking point and then calculate the triple product, as it would be closer to reality. This would entail calculating each specific amplitude correction to find whether the steepness of the wave is greater than unity.

To coincide with a specific location, ideally one could create the range of short waves created by flow over topography (even the Hawaiian Ridge specifically) numerically and test these coherent short waves as they travel through the inertial wave environments tested in this work. This would give further insight on what outcome to expect when following short waves purely created by flow over topography, and not the Garrett-Munk spectrum of short waves. These short-waves would correspond to certain types of encounters which have been studied here or would not be interacting with the inertial wave. Then using the methods of ray tracing and numericals simulations we could calculate a good estimate of what should happen after the short waves were created by over particular topography.

It would be of interest to do a statistical study, somewhat like that already completed, yet keep the amplitudes of each of the rays, and have a final and initial frequency spectrum not based solely on the number of waves at each frequency, but their energy. Then conclusions could be drawn about the energy in each frequency after interacting with an inertial wave. This may match observations slightly better. The analysis would not be difficult, but would be interesting and take some time.

It would also be interesting to do a statistical study within the numerical simulations. This would provide more information on the total wavefield as an array of waves propagate through an inertial wave.

The work done here can also be easily applied to the atmosphere. The ray tracing and numerical techniques may be used to test locations of breaking in the atmosphere, for example as wind blows over topography resulting in gravity-wave breaking and turbulence production. A three dimensional study has been done by Fritts and Garten [16], but the evolution of short waves to breaking has not yet been fully parameterized. These results would aid in the understanding of phenomenon such as clear air turbulence and how pollutants propagate up through the atmosphere.

V.B.1 Three-dimensional Ray Tracing

Experiments exist of a three-dimensional ray tracing of short waves propagating through a pancake dipole. Thus it would be of interest to use three-dimensional ray theory to compare with these results. Three-dimensional effects may alter the locations of strong refraction as refraction in the horizontal dimension will affect the frequency of the short-wave and therefore the group speed.

We would extend the ray tracing we have been doing to three dimensions. This means the velocity of the long wave will no longer be purely horizontal, and the short wave may refract in the horizontal direction, resulting in changes in the horizontal wavenumber. Godoy-Diana, Chomaz, and Donnadieu [20] have done experiments which test the interaction between downward propagating internal waves created by an oscillating cylinder and a pancake dipole created by closing two flaps and letting a piece of the vortex through a hole into the tank. In the vertical plane along the centerline the horizontal velocity profile of the pancake dipole can be described by a gaussian. Along this line they found that internal waves propagating in the same direction as the dipole (co-propagating) reached a critical layer and were absorbed by the dipole. Internal waves propagating opposite of the dipole (counter-propagating), though, reached turning points along the centerline and were refracted back upward through the tank. The horizontal structure of the dipole causes the co-propagating internal wave field to diverge, resulting in defocusing of the wave field. The opposite occurs when the internal waves are counter-propagating, the internal wave field converges, resulting in focusing of the wave field. Their experimental results support this. In the co-propagating case no waves are in the vertical centerline plane after the dipole passes, even when no critical layer is reached. The wave field has diverged. In the counter-propagating case they see waves, with amplified wave amplitude, below the dipole on the centerline where the wave should have been refracted upward. The wave field has converged. These three-dimensional effects result in a limiting of the horizontal extent of the critical layer in the co-propagating case, negatively effecting the momentum transfer, and an increase in wave activity along the centerline of the dipole in the counter-propagating case.

Godoy-Diana, Chomaz, and Donnadieu [20] were able to use two-dimensional ray tracing calculations to compare with the plane of vertical symmetry in the experiments. They found critical layers and turning points occuring at the same locations as seen in the experiments. These simulations did not account for the three-dimensional refraction and focusing of the waves and so these phenomenon were not tested. We can extend the ray tracing calculations to include these three-dimensional effects and find if ray theory can predict the results seen in the experiments. Then we will better understand the propagation of short waves through three-dimensional shears and the whether there will be an increase or decrease in probability of short wave breaking leading to mixing as a result.

This work could also be accomplished in a three-dimensional numerical simulation of the problem. This would further complement the experiments and ray theory.

Bibliography

[1] M. H. Alford and R. Pinkel. Observations of overturning in the thermocline: The context of ocean mixing. *J. Phys. Oceanogr.*, 30:805–832, 2000.

[2] J. R. Booker and F. P. Bretherton. The critical layer for internal gravity waves in a shear flow. *J. Fluid Mech.*, 27:513–539, 1967.

[3] D. Broutman. On internal wave caustics. *J. Phys. Oceanogr.*, 16:1625–1635, 1986.

[4] D. Broutman and R. Grimshaw. The energetics of the interaction between short small-amplitude internal waves and inertial waves. *J. Fluid Mech.*, 196:93–106, 1988.

[5] D. Broutman, C. Macaskill, M. E. McIntyre, and J. W. Rottman. On doppler-spreading models of internal waves. *Geophys. Res. Lett.*, 24:2813–2816, 1997.

[6] D. Broutman and W. R. Young. On the interaction of small-scale oceanic internal waves with near-inertial waves. *J. Fluid Mech.*, 166:341–358, 1986.

[7] D. L. Bruhwiler and T. J. Kaper. Wavenumber transport: scattering of small scale internal waves by large-scale wavepackets. *J. Fluid Mech.*, 289:379–405, 1995.

[8] G. Buckley, D. Broutman, J. W. Rottman, and S. Eckermann. On the importance of weak steady shear in the refraction of short internal waves. *Geophys. Res. Lett.*, 26:2877–2880, 1999.

[9] C. Canuto, M. Y. Hussaini, A. Quarteroni, and T. A. Zang. *Spectral Methods in Fluid Dynamics*. Springer-Verlag, 1988.

[10] J. R. Cary, D. F. Escande, and J. L. Tennyson. Adiabatic invariant change due to separatrix crossing. *Phys. Rev. A*, 34:4256–4275, 1986.

[11] T. J. Dunkerton. Wave transience in a compressible atmosphere. Part i: Transient internal wave, mean-flow interaction. *J. Atmos. Sci.*, 38:281–297, 1981.

[12] S. D. Eckermann. Influence of wave propagation on the doppler spreading of atmospheric gravity waves. *J. Atmos. Sci.*, 54:2554–2573, 1997.

[13] G. D. Egbert and R. D. Ray. Significant dissipation of tidal energy in the deep ocean inferred from satellite altimeter data. *Nature*, 405:775–778, 2000.

[14] S. M. Flatté, F.S. Henyey, and J. A. Wright. Eikonal calculations of short-wavelength internal-wave spectra. *J. Geophs. Res.*, 90:7265–7272, 1985.

[15] D. C. Fritts. The transient critical-level interaction in a boussinesq fluid. *J. Geophys. Res*, 87:7997–8016, 1982.

[16] D. C. Fritts and J. F. Garten. Wave breaking and transition to turbulence in stratified shear flows. *J. Atmos. Sci.*, 53:1057–1085, 1996.

[17] N. Furuichi, T. Hibiya, and Y. Niwa. Bispectral analysis of energy transfer within the two-dimensional oceanic internal wave field. *J. Phys. Oceanogr.*, 35:2104–2109, 2005.

[18] C. Garrett. Mixing with latitude. *Nature*, 422:477–478, 2003.

[19] C. Garrett and W. H. Munk. Space-time scales of internal waves: A progress report. *J. Geophys. Res.*, 80:281–297, 1975.

[20] R. Godoy-Diana, J. Chomaz, and C. Donnadieu. Internal gravity waves in a dipolar wind: a wave-vortex interaction experiment in a stratified fluid. *J. Fluid Mech.*, 548:281–308, 2006.

[21] M. C. Gregg. Scaling turbulent dissipation in the thermocline. *J. Geophys. Res.*, 94:9686–9698, 1989.

[22] M. C. Gregg, T. B. Sanford, and D. P. Winkel. Reduced mixing from the breaking of internal waves in equatorial waters. *Nature*, 422:513–515, 2003.

[23] M. C. Gregg, D. P. Winkel, and T. B. Sanford. Varieties of fully resolved spectra of vertical shear. *J. Phys. Oceanogr.*, 23:124–141, 1993.

[24] R. Grimshaw. Nonlinear internal gravity waves and their interaction with the mean wind. *J. Atmos. Sci.*, 32:1779–1793, 1975.

[25] W. D. Hayes. Kinematic wave theory. *Proc. Roy. Soc. Lond.*, A320:209–226, 1970.

[26] P. Hazel. The effect of viscosity and heat conduction on internal gravity waves at a critical level. *J. Fluid Mech.*, 30:775–783, 1967.

[27] F. S. Henyey and N. Pomphrey. Eikonal description of internal wave interactions: a non-diffusive picture of "induced diffusion". *Dyn. Atmos. Oceans*, 7:189–219, 1983.

[28] F. S. Henyey, J. Wright, and S. M. Flatté. Energy and action flow through the internal wave field: an eikonal approach. *J. Geophys. Res*, 91:8487–8495, 1986.

[29] A. Hertzog, C. Souprayen, and A. Hauchecorne. Eikonal simulations for the formation and the maintenance of atmospheric gravity wave spectra. *J. Geophys. Res.*, 107:4145–4165??, 2002.

[30] T. Hibiya, M. Nagasawa, and Y. Niwa. Nonlinear energy transfer within the oceanic internal wave spectrum at mid and high latitudes. *J. Geophys. Res.*, 107:3207–3214, 2002.

[31] C. O. Hines. The saturation of gravity waves in the middle atmosphere. Part II: Development of doppler-spread theory. *J. Atmos. Sci.*, 48:1360–1379, 1991.

[32] C. O. Hines. Doppler-spread parameterization of gravity wave momentum deposition in the middle atmosphere. Part I: Basic formulation. *J. Atmos. Solar Terr. Phys.*, 59:371–386, 1997.

[33] M. Kruskal. Asymptotic theory of hamiltonian and other systems with all solutions nearly periodic. *J. Math. Phys.*, 3:806–828, 1962.

[34] E. Kunze, A. J. Williams III, and M. G. Briscoe. Observations of shear and vertical stability from a neutrally buoyant float. *J. Geophys. Res*, 95:18,127–18,142, 1990.

[35] S. G. Llewellyn Smith and W. R. Young. Conversion of the barotropic tide. *J. Phys. Oceanogr.*, 32:1554–1566, 2002.

[36] J. A. MacKinnon and K. B. Winters. Subtropical catastrophe: Significant loss of low-mode tidal energy at 28.9 degrees. *Geophys. Res. Lett.*, 32:15605–15610, 2005.

[37] J. A. MacKinnon and K. B. Winters. Spectral evolution of bottom-forced internal waves. *J. Phys. Oceanogr.*, 2006. submitted.

[38] J. A. MacKinnon and K. B. Winters. Tidal mixing hotspots governed by rapic parametric subharmonic instability. *J. Phys. Oceanogr.*, 2006. submitted.

[39] P. Müller and X. Liu. Scattering of internal waves at finite topography in two dimensions. Part ii: Spectral calculations and boundary mixing. *J. Phys. Oceanogr.*, 30:550–563, 2000.

[40] W. Munk and C. Wunsch. Abyssal recipes ii: energetics of tidal and wind mixing. *Deep-Sea Res. Part 1*, 45:1977–2010, 1998.

[41] W. H. Munk. Internal waves and small-scale processes. In B. A. Warren and C. H. Wunsch, editors, *Evolution of Physical Oceanography: Scientific Surveys in Honor of Henry Stommel*, pages 264–291. MIT Press, Cambridge, MA, 1981.

[42] M. Nagasawa, T. Hibiya, Y. Niwa, M. Watanabe, Y. Isoda, S. Takagi, and Y. Kamei. Distribution of fine-scale shear in the deep waters of the north pacific obtained using expendable current profilers. *J. Geophys. Res.*, 107:3221–3228, 2002.

[43] D. J. Olbers and N. Pomphrey. Disqualifying two candidates for the energy balance of oceanic internal waves. *J. Phys. Oceanogr.*, 11:1423–1425, 1981.

[44] T. R. Osborn. Estimates of the local rate of vertical diffusion from dissipation measurements. *J. Phys. Oceanogr.*, 10:83–89, 1980.

[45] O. M. Phillips. *Dynamics of the Upper Ocean, 1st ed.* Cambridge University Press, 1966.

[46] K. L. Polzin, J. M. Toole, J. R. Ledwell, and R. W. Schmitt. Spatial variability of turbulent mixing in the abyssal ocean. *Science*, 276:93–96, 1997.

[47] L. Rainville. *Propagation of the Internal Tide from the Hawaiian Ridge.* PhD thesis, Scripps Institution of Oceanography, University of California, San Diego, 2004.

[48] D. L. Rudnick, T. J. Boyd, R. E. Brainard, G. S. Carter, G. D. Egert, M. C. Gregg, P. E. Holloway, J. M. Klymak, E. Kunze, C. M. Lee, M. D. Levine, D. S. Luther, J. P. Martin, M. A. Merrifield, J. N. Moum, J. D. Nash, R. Pinkel, L. Rainville, and T. B. Sanford. From tides to mixing along the Hawaiian ridge. *Science*, 301:355–357, 2003.

[49] K. N. Sartelet. Wave propagation inside an inertia wave. Part I: Role of time dependence and scale separation. *J. Atmos. Sci.*, 60:1433–1447, 2003.

[50] K. N. Sartelet. Wave propagation inside an inertia wave. Part II: Wave breaking. *J. Atmos. Sci.*, 60:1448–1455, 2003.

[51] L. St. Laurent and C. Garrett. The role of internal tides in mixing the deep ocean. *J. Phys. Oceanogr.*, 32:2882–2899, 2002.

[52] L. St. Laurent and J. Nash. An examination of the radiative and dissipative properties of the internal tides. *Deep Sea Res.*, 51:3029–3042, 2004.

[53] C. Staquet and J. Sommeria. Internal gravity waves: From instabilities to turbulence. *Ann. Rev. Fluid Mech.*, 34:559–593, 2002.

[54] H. Sun and E. Kunze. Internal wave-wave interactions. Part I: The role of internal wave vertical divergence. *J. Phys. Oceanogr.*, 29:2886–2904, 1999.

[55] H. Sun and E. Kunze. Internal wave-wave interactions. Part II: Spectral energy transfer and turbulence production. *J. Phys. Oceanogr.*, 29:2905–2919, 1999.

[56] B. R. Sutherland. Finite-amplitude internal wavepacket dispersion and breaking. *J. Fluid Mech.*, 429:343–380, 2001.

[57] B. R. Sutherland. Internal wave instability: Wave-wave vs wave-induced mean flow interactions. *J. Phys. Oceanogr.*, 2006. under review.

[58] H. Tennekes and J. L. Lumley. *A First Course in Turbulence.* The MIT Press, 1972.

[59] W. Thomson. Stability of fluid motion – rectilineal motion of viscous fluid between two parallel planes. *Phil. Mag.*, 24:188–196, 1887.

[60] S. A. Thorpe. An experimental study of critical layers. *J. Fluid Mech.*, 103:321–344, 1994.

[61] J. C. Vanderhoff, K. K. Nomura, J. W. Rottman, and C. Macaskill. Doppler spreading of internal gravity waves by an inertia-wave packet. *J. Geophys. Res.*, 2007. accepted.

[62] M. Watanabe and T. Hibiya. Estimates of energy dissipation rates in the three-dimensional deep ocean internal wave field. *J. Oceanog.*, 61:123–127, 2005.

[63] J. H. Williamson. Low-storage runge-kutta schemes. *J. Comp. Phys.*, 35:48–56, 1980.

[64] K. B. Winters and E. A. D'Asaro. Two-dimensional instability of finite amplitude internal gravity waves packets near a critical layer. *J. Geophys. Res.*, 94:12,709–12,719, 1989.

[65] K. B. Winters and E. A. D'Asaro. Three-dimensional wave instability near a critical level. *J. Fluid Mech.*, 272:255–284, 1994.

[66] K. B. Winters and J. J. Riley. Instability of internal waves near a critical level. *Dyn. Atmos. Oceans*, 16:249–278, 1992.

[67] C. Wunsch. The work done by the wind on the ocean circulation. *J. Phys. Oceanogr.*, 28:2331–2339, 1998.

[68] E. D. Zaron and G. D. Egbert. Estimating open-ocean barotropic tidal dissipation: The hawaiian ridge. *J. Phys. Oceanogr.*, 36:1019–1035, 2006.